Title: Multiple resolution seismic attenuation imaging at Mt. Vesuvius

Corresponding Author: Edoardo Del Pezzo, Dr.

Corresponding Author's Institution: INGV - Osservatorio Vesuviano

First Author: Luca De Siena

Order of Authors: Luca De Siena; Edoardo Del Pezzo; Francesca Bianco; Anna Tramelli

Abstract: A three-dimensional S wave attenuation tomography of Mt. Vesuvius has been obtained with multiple measurements of coda-normalized S-wave spectra of local small magnitude earthquakes. We used 6609 waveforms, relative to 826 volcano-tectonic earthquakes, located close to the crater axis in a depth range between 1 and 4 km (below the sea level), recorded at seven 3-component digital seismic stations. We adopted a two-point ray-tracing; rays were traced in an high resolution 3-D velocity model. The spatial resolution achieved in the attenuation tomography is comparable with
that of the velocity tomography (we resolve 300 m side cubic cells). We statistically tested that the results are almost independent from the radiation pattern. We also applied an improvement of the ordinary spectral-slope method to both P- and S-waves, assuming that the differences between the theoretical and the experimental high frequency
spectral-slope are only due to the attenuation effects. We could check the coda-normalization method comparing the S attenuation image obtained with the two methods. The images were obtained with a multiple
resolution approach. Results show the general coincidence of low attenuation with high velocity zones. The joint interpretation of velocity and attenuation images allows us to interpret the low
attenuation zone intruding toward the surface until a depth of 500 meters
below the sea level as related to the residual part of solidified magma from the last eruption. In the depth range between -700 and -2300 meters above sea level, the images are consistent with the presence of multiple acquifer layers. No evidence of magma patches greater than the minimum cell dimension (300m) has been found. A shallow P wave attenuation
anomaly (beneath the southern flank of the volcano) is consitent with the presence of gas saturated rocks.
The zone characterized by the maximum seismic energy release cohincides with a high attenuation and low velocity volume, interpreted as a cracked medium.

Abstract

A three-dimensional S wave attenuation tomography of Mt. Vesuvius has been obtained with multiple measurements
of coda-normalized S-wave spectra of local small magnitude earthquakes. We used 6609 waveforms, relative to 826
volcano-tectonic earthquakes, located close to the crater axis in a depth range between 1 and 4 km (below the sea
level), recorded at seven 3-component digital seismic stations. We adopted a two-point ray-tracing; rays were traced
in an high resolution 3-D velocity model. The spatial resolution achieved in the attenuation tomography is comparable with
that of the velocity tomography (we resolve 300 m side cubic cells). We statistically tested that the results are almost
independent from the radiation pattern. We also applied an improvement of the ordinary spectral-slope method to
both P- and S-waves, assuming that the differences between the theoretical and the experimental high frequency
spectral-slope are only due to the attenuation effects. We could check the coda-normalization method
comparing the S attenuation image obtained with the two methods. The images were obtained with a multiple
resolution approach. Results show the general coincidence of low attenuation
with high velocity zones. The joint interpretation of velocity and attenuation images allows us to interpret the low
attenuation zone intruding toward the surface until a depth of 500 meters
below the sea level as related to the residual part of solidified magma from the last eruption. In the depth range
between -700 and -2300 meters above sea level, the images are consistent with the presence of multiple acquifer layers. No evidence of
magma patches greater than the minimum cell dimension (300m) has been found. A shallow P wave attenuation
anomaly (beneath the southern flank of the volcano) is consitent with the presence of gas saturated rocks.
The zone characterized by the maximum seismic energy release cohincides with a high attenuation and low velocity
volume, interpreted as a cracked medium.

MS. REF. NO.: PEPI-D-07-00301
 TITLE: MULTIPLE RESOLUTION SEISMIC ATTENUATION IMAGING AT MT. VESUVIUS
 PHYSICS OF THE EARTH AND PLANETARY INTERIORS

Dear Editor,
First of all we want to thank both reviewers for the suggestions, which were
really useful to improve the paper quality, and in particular the graphical
representation of the results obtained.
We took into account all the suggestions made by both reviewers. We also answer
to the questions raised, to better clarify how we corrected the paper. We
specify all the points, starting from those raised by Referee 2.
One of the main point to be addressed is the improving of all the synthetic
tests. We hence decided to a) include in the article a synthetic anomaly test;
b) to explicitly show the checkerboard test; c) to mark the high resolution
volume enlightening the test results inside this zone.
Another important point was the discussion of the results, too short and concise
in the first version. We re-wrote completely all this stuff, trying to
explicitly illustrate in detail our interpretation.
The other major comment regards the effective resolution of our method (300 m).
We follow an empirical rule, that the wavelength must be lower than a half of
the minimum cell size. Moreover, we consider for the interpretation only those
cell crossed by a number of rays defined by the empirical equation (14). The
question arisen by rev. 3 about the formal correctness of formula (14) is right.
With the decreasing of the cell size, the minimum number of rays passing through
the cell also decreases. Anyway, this number is never lower than 4. We have
empirically observed that this number ensures stable results. So, we are
confident that, even with a decreasing resolution, the results do not represent
ghost images.

All the other minor points have been fully addressed, as reported in the
following list, in which in capital letters there is copied the reviewer
comment, and in lower case our reply.

Multiple resolution seismic attenuation imaging at Mt. Vesuvius

Luca De Siena[1] *Edoardo Del Pezzo[1] Francesca Bianco[1]
Anna Tramelli[1]

[1]*Istituto Nazionale di Geofisica e Vulcanologia , sezione di Napoli Osservatorio Vesuviano, Via Diocleziano, 328 - 80124 Napoli, Italia.*

∗ fax: +39 081 6108323 ; email: delpezzo@ov.ingv.it

Abstract

A three-dimensional S wave attenuation tomography of Mt. Vesuvius has been obtained with multiple measurements of coda-normalized S-wave spectra of local small magnitude earthquakes. We used 6609 waveforms, relative to 826 volcano-tectonic earthquakes, located close to the crater axis in a depth range between 1 and 4 km (below the sea level), recorded at seven 3-component digital seismic stations. We adopted a two-point ray-tracing; rays were traced in an high resolution 3-D velocity model. The spatial resolution achieved in the attenuation tomography is comparable with that of the velocity tomography (we resolve 300 m side cubic cells). We statistically tested that the results are almost independent from the radiation pattern. We also applied an improvement of the ordinary spectral-slope method to both P- and S-waves, assuming that the differences between the theoretical and the experimental high frequency spectral-slope are only due to the attenuation effects. We could check the coda-normalization method comparing the S attenuation image obtained with the two methods. The images were obtained with a multiple resolution approach. Results show the general coincidence of low attenuation with high velocity zones. The joint interpretation of velocity and attenuation images allows us to interpret the low attenuation zone intruding toward the surface until a depth of 500 meters below the sea level as related to the residual part of solidified magma from the last eruption. In the depth range between -700 and -2300 meters above sea level, the images are consistent with the presence of multiple acquifer layers. No evidence of magma patches greater than the minimum cell dimension (300m) has been found. A shallow P wave attenuation anomaly (beneath the southern flank of the volcano) is consitent with the presence of gas saturated rocks. The zone characterized by the maximum seismic energy release cohincides with a high attenuation and low velocity volume, interpreted as a cracked medium.

Key words: Attenuation tomography, Mt. Vesuvius, Coda normalization method, Spectral slope, Multi resolution inversion

1 Introduction.

The knowledge of the internal structure of the volcanoes represents a crucial task to properly constrain the physical models of eruption. Passive tomography is one of the easiest and cheapest way to achieve this goal and is consequently widely applied for the study of volcano structures at several depths (Chouet et al., 1996).

There are two main factors limiting the maximum resolution that can be obtained in passive methods: the ray coverage and the wavelength of the waveforms from which the observables are retrieved. The first factor is linked to the station density and the source space distribution. The second is directly associated with the kind of events that are used as input. For a local tomography on a volcano with a volume of the order of 10 km of linear dimensions, local VT earthquakes, with their associate wavelengths that ordinary span from some kilometers to hundreds of meters (Chouet, 2003) are a suitable input. Generally the smallest wavelength characterizes the minimum cell size, and this can be considered as the thumb rule for this constraint. Moreover, to reach this minimum cell size, one needs a suitable source space distribution (sources as much as possible uniformly distributed in the volume, and an as dense as possible network of receivers). In a configuration typical of an up-to-date seismic network, an order of resolution of 300 meters can be reached only in the volume cells with a sufficient ray coverage (Chouet et al., 1996). This leads to the solution of a mixed-determined problem, with an highly overdetermined system of equations correspondent to the cells with a redundant number of rays crossing through, and an equal- or lower-determined system for the other cells. A way to optimize the problem is to use an approach with a non uniform cell size, that maintains a sufficient over-determination in any cell, but reaches a good resolution only in the parts of the investigated volume characterized by the maximum ray coverage. This kind of approach is typically named as multi-step or multiple-resolution method [see Bai and Greenhalgh (2005), for an example of travel time multi-step tomography on a volcano].

The attenuation of elastic waves depends strongly on a number of factors affecting the lithology, the most important of which are probably the temperature and the presence of fractures and hydrothermal or magmatic fluids. Attenuation is quantified by the quality factor, Q, defined as the ratio between the energy lost by a wave cycle and the energy of the cycle itself; equivalently, attenuation can be defined through the attenuation coefficient $\alpha = \pi f r / v Q$ that accounts for the damping of the wave amplitude, A, as a function of distance, r and frequency, f. This factor may greatly vary for rocks with the same composition but different degree of fracturing and/or temperature. The response of the rocks to the propagation of longitudinal and shear waves is different; the independent determination of the quality factors for longitudinal

2

(Qp) and shear (Qs) waves, critical parameters for the characterization of the physical state of the rocks within a volcano, aims at discriminating between melt fluids and gases residing at shallow depths in the earth's crust. For this purpose, a comparative study of velocity and attenuation tomography can be critical (Hansen et al., 2004).

A phenomenon that intensely affects the wave propagation in volcanic areas is the scattering process, which tends to transfer the high-frequency energy of direct P and S waves into the coda of the seismograms (Sato and Fehler, 1998). Scattering is produced by the interaction of the wavefield with the small scale heterogeneities in the elastic parameters, as, for example, those associated with intense rock fracturing. The average attenuation caused by scattering, can be studied independently from the one caused by intrinsic attenuation, separating the two different types of losses (Bianco et al., 1999). Results on volcanoes show that, for frequencies higher than 10 Hz, scattering attenuation is more important than intrinsic attenuation (Del Pezzo et al., 2006 a). For a comprehensive summary of results from attenuation measurements by a range of methods, at varying frequency, on different scales and in different geological settings the reader is referred to Sato and Fehler (1998).

Unfortunately, for the single path estimates (necessary for tomography) of the attenuation coefficient, the separation between the two kinds of contribution (scattering and intrinsic) is practically impossible. Consequently, in the attenuation tomography, the parameter obtained by the inversion is the total-Q or the correspondent attenuation coefficient.

This paper is aimed at giving an image of the shallow crust materials at Mt. Vesuvius volcanic area using shear wave attenuation tomography at high frequency (in the range between 10 and 20 Hz), solved with a multi-resolution method with a minimum cell (the greatest available resolution) of 300 meters. Observables (total-Q inverse for each single path) are obtained using the coda-normalization method (Aki, 1980), and checked with the ordinary spectral-slope method. Spectral slope is used also to estimate P-wave total Q-inverse. Attenuation images are eventually compared with high resolution passive velocity tomography [the same minimum cell size, Scarpa et al. (2002)]. The images obtained with this method are also compared with those obtained at a resolution of 900 meters in a previous study of the same area, carried out using a subset of the present data set (Del Pezzo et al., 2006 b).We will show that the low attenuation zone located under the crater is coincident with a high velocity volume, possibly associated with residual frozen magma from the last eruptions; and that a high attenuation volume at 1-2 km of depth is coincident with a low velocity zone. This is interpreted as the aquifer permeating the shallow structure of Mt. Vesuvius.

2 Geological and seismological settings.

Mt. Vesuvius is a stratovolcano formed by an ancient caldera (Mt. Somma) and by a younger volcanic cone (Mt. Vesuvius). The volcanic activity is dated back to 300–500 ky (Santacroce, 1987) and characterized by both effusive and explosive regimes (Andronico et al., 1995). The volcanic complex is located in the Campania plain (southern Italy) at the intersection of two main fault systems oriented NNW–SSE and NE–SW (Bianco et al., 1997). The last eruption, in March 1944, was effusive (Berrino et al., 1993). It may have started a new obstructed conduct phase and hence a quiescent stage.

The seismic activity is actually the unique indicator of the internal dynamics [see e.g. De Natale et al. (1998)]. Seismicity studies are of extreme importance for the high risk volcanic area of Mt. Vesuvius. As an overall, the seismicity of Mt. Vesuvius is characterized by a mean rate of approximately 300 events per year. The largest earthquake in the area [reasonably since the last eruption -1944- see Del Pezzo et al. (2004)] occurred in 1999, and has been associated with regional and local stress fields (Bianco et al., 1997). The main features of the earthquake space and time distribution are described in the papers by Scarpa et al. (2002), hereafter cited as SCA02, and Del Pezzo et al. (2004). In the study of SCA02 the relocated seismicity appears to extend down to 5 km below the central crater, with most of the energy (up to local magnitude 3.6) clustered in a volume spanning 2 km in depth, positioned at the border between the limestone basement and the volcanic edifice. The hypocentral locations for the data used in the present article show the same pattern of the overall seismicity (Figure 1).

The earthquakes recorded at Mt. Vesuvius are mostly of volcano-tectonic type (VT), with fault-plane orientations, showing an highly non-regular spatial pattern. The spectral content of the P- and S-wave trains of the VT events is compatible with stress drops spanning a range between 1 and 100 bars (100 bars for the largest magnitude) and focal dimensions of the order of 100 m (Del Pezzo et al., 2004).

The velocity structure beneath Mt. Vesuvius, in the depth range from the Earth surface to 10 km, has been deduced by seismic tomography. Auger et al. (2001) suggest the presence of a melting zone at a depth of about 8 km, on the base of the TOMOVES experiment results (see the book by Capuano et al. (2003) and the numerous references therein). At smaller scale, between the topographical surface and 5 km of depth, SCA02 evidence a low velocity contrast between 1 and 2 km, possibly associated with the presence of aquifers. No shallow and small magma chambers are visible at the resolution scale reached by SCA02.

3 Data selection.

In the present work we utilized a total number of 6609 waveforms, obtained from a selection of 826 earthquakes recorded from January 1996 to June 2000 at seven 3-component stations that are the analogical station OVO (66 dB dynamic range, three component) sampled at 100 s.p.s. and 6 digital, high dynamic (120 dB, gain ranging), 1 Hz , seismic stations sampled at 125 s.p.s. (Table I). Analog anti-aliasing filter with 25 Hz cut-off frequency operated on all the data logger prior to sampling. Data selection has been made on the base of the following pre-requisites: the best signal to noise ratio, the absence of spikes and other disturbances in the waveforms, a minimum coda duration (from origin time) of 15 s and the absence of secondary events in the early coda. In doing this selection we implicitly restricted the earthquake magnitude in the range from 1.6 to 3.0, because small aftershocks are often present in the coda of larger events. Location of the 826 earthquakes (Figure 1) was obtained using P-picking of all the available seismic stations constituting the monitoring network (www.ov.ingv.it) with a non linear procedure based on a grid-search algorithm (Lomax et al., 2001); ray-tracing was calculated using the $3D$ velocity model obtained by SCA02.

4 Methods.

4.1 Ray tracing.

We used a Thurber-modified approach (Block, 1991) to trace the path of each ray in the 3-D velocity structure of Mt. Vesuvius obtained by SCA02. This is an extension of the approximate ray-bending method (Um and Thurber, 1987) that works well in velocity structures characterized by fairly sharp velocity variations, like that of Mt. Vesuvius. The only limitation is that the method does not compute reflected ray paths, that anyway are not taken into account in the present work. After dividing the whole structure to be investigated in three different grids (respectively with 1800, 900 and 300 m cubic cell size) we stored in a database the length of each ray, connecting each source to each receiver, and the length of the ray-segments crossing each cell. This database is necessary for the multiple-resolution inversion approach, as discussed later.

4.2 Single-path attenuation with the coda-normalization (CN) method.

The CN method is widely used to retrieve attenuation parameters independently of the site and instrumental transfer function [Aki (1980); Sato and Fehler (1998)]. Del Pezzo et al. (2006 b) used this approach for the estimation of single path total Q-inverse to map the S-wave attenuation structure in Mt. Vesuvius area, using a subdivision of the investigation volume in cubic cell of 900 meters in a single-scale approach. Even though the method used to estimate the single path inverse total-Q has been already described and discussed in Del Pezzo et al. (2006 b), we report in Appendix 1 a synthesis for sake of completeness.

Our reference equation (see Appendix 1 and 2 for any detail) is:

$$\frac{E_{ij}(f,r)}{E^C(f,t)}r_{ij}^2 = \frac{1}{P(f,t_c)}\exp\left[-2\pi f\int_{r_{ij}}\frac{dl}{v(l)Q_T^{ij}(l)}\right] \qquad (1)$$

Taking logs of both sides of eq. (1) and approximating the line integral with a sum, we can write

$$d_k^C = \frac{1}{2\pi f}\ln(\frac{1}{P(f,t_c)}) - \sum_{b=1}^{N\_cells} l_{kb}s_b Q_b^{-1} \qquad (2)$$

where d_k^C represents the log of energy spectral ratio between S and coda premultiplied for the squared ray-length and divided for $2\pi f$. N_cells is the total number of blocks crossed by the ray , l_{kb} is the length of the k-th ray-segment intersecting the b-th block characterized by slowness s_b and inverse quality factor Q_b^{-1}. In this formulation we use the suffix k to indicate the k-th ray of the suite of rays connecting stations to sources. Eq. (2) can be rewritten separating Q_b^{-1} into an average Q_b^{-1}, $<Q_b^{-1}>$, that we assume to be equal to the average quality factor for the whole area (Q_T^{-1}), and an incremental δQ_b^{-1}.It results:

$$\widetilde{d}_k^C = \sum_{b=1}^{N\_cells} l_{kb}s_b\delta Q_b^{-1} \qquad (3)$$

where:

$$\widetilde{d}_k^C = \frac{1}{2\pi f}\ln(\frac{1}{P(f,t_c)}) - d_k^C - Q_T^{-1}\sum_{b=1}^{N\_cells} l_{kb}s_b \qquad (4)$$

Eq. (3) represents a linear system of N_k equations in N_cells unknowns that can be inverted, as discussed in the next chapters.

4.3   The estimate of the observables with the CN method.

Prior to the application of the CN method we checked the temporal stability of the S-wave time window for the radiation pattern effect, as widely described in Appendix 2. Accordingly, we set the duration of the S-wave time window at 2.5 s starting from the S-wave arrival time. Coda signal time window starts at 8 s lapse time and ends at 12 s, since most of our data show a favorable signal-to-noise ratio ($>$3) for lapse time smaller than 12 s. A Discrete Fourier Transform (DFT) is applied to the signals after windowing (we used a cosine taper window with tapering at 10% both for S and coda) for both the horizontal components of the ground motion. We calculate the S spectral amplitude averaged in the frequency bands centered at the values of frequency, f_c,with bandwidths ($\pm\Delta f$) reported in Tab II, and finally log-averaged over the components; we thus obtain the ratio between the S-wave spectrum and the coda spectrum. The natural logarithm of this ratio estimates d_k^C of formula (4). The constant in eq. (2) has been already estimated by Del Pezzo et al. (2006 b) for the area under study.

4.4   The slope-decay (SD) method .

As a complementary approach, we adopted the so called slope decay method, which has been widely used to estimate the attenuation coefficient in many regions of the world [Nava et al. (1999), Giampiccolo et al. (2003), Gudmundsson et al. (2004)].

As well known, the amplitude spectral density for S and P waves for frequencies higher than the corner frequency can be expressed as the product of source, path and site effects as:

$$A_{ij}^{HF}(f,r) = S_i^A(f)I_j(f)T_j(f)G_{ij}(r)\exp(-\pi f\frac{t_{ij}(r)}{Q_T^{ij}(r)}) \qquad (5)$$

where $A^{HF}(f,r)$ is the high-frequency spectral amplitude of the P- or S-wave radiation emitted by the source i at total distance r measured along the source(i)-station (j) ray-path; f is the frequency; $S_i^A(f)$ is the amplitude spectrum at source; I_j is the instrument transfer function; T_j is the site transfer function and G is the geometrical spreading term; t_{ij} is the travel time along the ray of length r and Q_T^{ij} is the total quality factor measured along the ray-path. In the present formulation we assume that the high frequency amplitude spectrum at the source can be described by a function $S_i^A = const_i \cdot f^{-\gamma}$, γ being a constant for the whole set of data utilized. Taking the natural logarithm and making the derivative of the eq. (5) respect to frequency, f, it can be written for each ray-path:

$$D_f(\ln A_{ij}^{HF}) = D_f(\ln S_i^A) - \pi \frac{t_{ij}(r)}{Q_T^{ij}(r)} \tag{6}$$

where D_f is the symbol of derivative. In obtaining formula (6) we assumed the independence of frequency for the site and instrument transfer function. The independence of frequency for the site term has been confirmed by Galluzzo et al. (2005) who studied the site transfer function at Mt. Vesuvius. The transfer function of the instruments is flat with frequency in the whole frequency range investigated. Transforming the couple of indexes ij in a single integer k associated with the single ray, as in the previous section, we can write:

$$D_f(\ln A_k^{HF}) = D_f(\ln S_i^A) - \pi \frac{t_k(r)}{Q_T^k(r)} \tag{7}$$

Averaging the left hand quantity of the above equation over the rays considered (k index) we obtain:

$$< D_f(\ln A_k^{HF}) >_k = D_f^0(\ln A^{HF}) =$$
$$< D_f(\ln S_i^A) - \pi \frac{t_k(r)}{Q_T^k(r)} >_k \quad = D_f^0(\ln S^A) - \pi < \frac{t(r)}{Q_T(r)} >_k \tag{8}$$

$D_f^0(\ln S^A)$ results to be the same of $D_f(\ln S_i^A)$ (the average of the source spectral derivative equals the spectral derivative for the single event), so that we can write:

$$D_f(\ln A_k^{HF}) - D_f^0(\ln A^{HF}) \tilde{=} \pi (< \frac{t(r)}{Q_T(r)} >_k - \frac{t_k(r)}{Q_T^k(r)}) \tag{9}$$

Indicating with d^D the quantity:

$$d_k^D = \frac{1}{\pi} \left[D_f(\ln A_k^{HF}) - D_f^0(\ln A^{HF}) \right] \tag{10}$$

and expressing the right hand side of eq. (9) as already done in eq. (1) we obtain:

$$d_k^D = < \frac{t(r)}{Q_T(r)} >_k - \sum_{b=1}^{N\_cells} l_{kb} s_b Q_b^{-1} \tag{11}$$

where the index k is referred to the k-th ray.

Making the same assumption that leads to formula (3), we can finally write:

$$\widetilde{d}_k^D = \sum_{b=1}^{N\_cells} l_{kb}s_b\delta Q_b^{-1} \tag{12}$$

where:

$$\widetilde{d}_k^D = < \frac{t_k}{Q_k} > -d_k^D - Q_T^{-1}\sum_{b=1}^{N\_cells} l_{kb}s_b \tag{13}$$

The inversion schemes (3) and (12) are formally identical, apart the constant values.

4.5   The estimate of the observables with the SD method.

Direct S spectral amplitudes were obtained in the frequency band centered at $f_c = 18\ Hz$, with the same bandwidth used for the CN method (Table II). The use of only this central frequency value is justified by the spectral features of the seismicity at Vesuvius like broadly discussed in Del Pezzo et al. (2006 b). We applied a DFT to windowed signals of length 2.5 seconds starting from the direct S travel time for both W-E and S-N components of the ground motion; then we log-averaged the spectra over the components.

We applied the SD method both to direct S waves and to direct P waves. Spectral amplitude for P waves was calculated in a time window starting from the P-wave onset and ending at 0.1 s before the S-wave picking, tapering each spectrum with a 10% cosine taper function.

The derivative was carried out for both S and P log-spectra in the frequency band starting from corner frequency (around 10 Hz for the whole set of data) and ending at 23 Hz (before the cut-off frequency of the anti-alias filter that was set up at 25 Hz). The derivative was computed using MATLAB "diffnew" routine.

5   Multi-resolution inversion.

The resolution of the methods depends both on the wavelength (which has to be smaller than the cell size) and on the number of rays crossing the single cell. A frequency $fc = 12$ Hz corresponds to a wavelength of about $200\ m$ for S waves. For P waves (examined at 18 Hz only) the corresponding wavelength is of the order of 150 m. Taking a cell size of 300 m we observe that the blocks bordering the volume of investigation are crossed by a number of rays

insufficient to ensure stability in the final solution, due to the distribution of the sources, concentrated along the crater axis and not uniformly distributed in space and depth inside the volume under investigation. This is the reason why we cannot invert the whole data set using a uniform resolution of 300 m. Consequently, we seek for solutions that can represent images in cells with a non-uniform size, as other researchers do in velocity tomography[Thurber (1987), Sambridge et al. (1998)]. In this approach, a relatively high-resolution can be obtained in a target area with a good ray coverage (this avoids linear dependence among the system equations). To perform this task we use an iterative inversion scheme [Thurber (1987), Eberhart-Phillips (1990)], in which we employ the results obtained in a lower resolution (LRR) as input for highest resolution (HRR). Bai and Greenhalgh (2005) describe an inversion scheme of this kind, applied to velocity tomography. Our inversion scheme is different from those above cited and will be described in the following points.

(1) The observables are calculated (both for the CN method and the SD method we apply the same inversion procedure) as above described.
(2) The attenuation factor averaged over the whole volume under study, Q_T^{-1}, is estimated with the CN method. It results in a really good agreement with that estimated by the previous works in the same area [Bianco et al. (1999), Del Pezzo et al. (2006 a)].
(3) The problem of eq. (3) and (12) is solved for a volume divided in cubic blocks of 1800 m side, using a positivity constraint. Then, each 1800 m side block is divided in 8 blocks of 900 m side, and the inverse quality factors thus calculated, $(Q_b^{-1})^{1800}$, are assigned to each of this cubes.
(4) The problem is solved for the 900 m cell size resolution, taking into consideration that each ray is characterized by the attenuation factor, which has been obtained by the solution of the previous step. In this way we obtain the new quantity $(\delta Q_b^{-1})^{900}$, which represents the variation from the inverse quality factor $(Q^{-1})^{1800}$ assigned to the 900 meters block in the previous step. We divide as before each 900 meters block in 27 blocks of 300 m side, assigning to each of them the inverse quality factor $(Q_b^{-1})^{900}$. Also for this step we use a positivity constraint on the $(Q_b^{-1})^{900}$.
(5) Finally we solve the problem for a 300 m side cell resolution, obtaining $(\delta Q_b^{-1})^{300}$.

It is noteworthy that, whereas the data vectors and the coefficient matrices need to be recalculated at each scale, the inversion problem is always formally the same and is given by equations (3) and (12). The details regarding how the data vectors and coefficient matrices are upgraded at each scale are reported in Appendix 3. It is also important to note that, at each step, we accept the solutions for the blocks in which the number of ray-segments , n_R, is given by:

$$n_R \geq \frac{2 Block\_side}{\lambda} \qquad (14)$$

10

This empirically determined threshold would ensure, in the assumption that the directions of ray-segments are randomly distributed in each block, that each block is homogeneously sampled.

6   Robustness, stability, checkerboard and synthetic anomaly tests.

6.1   a) Robustness

The robustness of the method is tested using a bootstrap approach, reducing randomly the number of available equations (rays). We applied this test to all the blocks at each cell size. The solutions for blocks of 1800 meters side were obtained for progressive reductions of the equations used to solve the inverse problem (see Appendix 3 , formula (21)); at each step we measured the quantity:

$$P = \frac{Q_b(0) - Q_b(\%)}{Q_b(0)} \times 100 \tag{15}$$

where $Q_b(\%)$ is the quality factor of the block b obtained for the reduced data set, whereas $Q_b(0)$ is the solution obtained using the whole database. We repeated the inversion 100 times for each data reduction, measuring then the average percentage . We observed in most of the cases a significant increase of the percentage for a reduction of more then 40% of the data-set . The results for all the blocks of 1800 meters side solved are reported in Table III.

We repeated the same procedure for each scale, i.e. we measured the quantity P of formula (15) for all the 900 meters side blocks. We obtain a significant change in the value of P and a significant reduction of the average blocks resolved, for a random extraction of more than 40% of data. For sake of synthesis we report in Table IV the results obtained for 8 blocks contained in a single 1800-side block which resulted to be characterized by $(Q_b^{1800})^{-1} = 0.0128$; its position is shown in the upper panels of Figure 1 using the light grey square evidenced by number **1**. The results for the other 900 m side blocks solved by the inversion are similar.

Finally, we compared the variations of P calculated with eq. (15) for all the 300 meters side blocks, observing both a significant change in the value of the parameter models and a significant reduction in the average number of blocks resolved, for the random extraction of more than 20% of data. We report in Table V a selection of 8 blocks of 300 meters contained in the singular block of 900 meters side having $(Q_b^{900})^{-1} = 0.011$ (the position of the 900 meters block is shown in the upper panels of Figure 1 using the dark grey square evidenced

11

by number **2**).

6.2   b) Stability.

The stability of the method is checked by changing the value of the constants in formulas (4) and (13). In formula (4) we let g_0 to vary between the values of $g_{\min} = 1$ and $g_{\max} = 2.5$ that represent the error limits of the average g as reported in Del Pezzo et al. (2006 a). In formula (13) we let $< \frac{t_k}{Q_k} >$ to vary in the interval $[-3\sigma + < \frac{t_k}{Q_k} > , +3\sigma + < \frac{t_k}{Q_k} >]$. The results do not change significantly. In both (4) and (13) we let Q_T^{-1} to vary in the interval $[-3\sigma + Q_T^{-1} , +3\sigma + Q_T^{-1}]$

For the resolution of $1800m$ the variations of each parameter model obtained for the extreme values are reported in Table VI.

For the intermediate resolution (900 meters) we repeat the same procedure setting maximum and minimum values of $(Q^{1800})^{-1}$ and $Q_T{}^{-1}$ sampled in their confidence interval (3σ). The 8 blocks considered in Table VII are the same of Table IV.

For the maximum available resolution (300 meters), using the results obtained changing the values of Q_T^{-1}, $(Q_b^{1800})^{-1}$ and $(Q_b^{900})^{-1}$ in their confidence interval, we obtain the results shown in Table VIII for the 8 blocks considered in Table V.

6.3   c) Checkerboard inside the HRR.

Our results have been tested imposing an a priori attenuation structure to the area: we assumed an homogeneous medium in the LRR and a checkerboard distribution of the quality factors in the volume where the HRR is located, resolving only the blocks crossed by at least 5 rays per block, following eq. (14). Using the CN method we calculated the true spectral ratios and added to these values a Gaussian random error calculated with a random number generator with zero mean and standard deviation equal to 10% of the spectral ratio.

The synthetic structure results to be extremely well resolved in the central part, whereas the quality of the reproduction of the input values decreases toward the borders of the volume under investigation. The checkerboard test results (Figures 2 and 3) are shown both for the W-E and S-N sections already shown in Figure 1, and for five horizontal slices in the depth range between -500 to $-3500m$.

Both in Figure 2 and Figure 3 we marked with a white broken line the zone where the checkerboard structure is effectively reproduced, as described in the following. In Figure 2 it can be noticed that the input checkerboard structure (W-E and S-N sections in panel a) is well reproduced everywhere except in a small area toward North and toward East, corresponding to the geological structure of Mt. Somma (the same sections in panel b); this is due to the lack of seismic sensors in this area. The negative variations in the inverse quality factors under -3000 meters always well reconstruct the zones with low Q_S^{-1}. In Figure 3 the five panels on the left present five horizontal sections of the volume containing the input checkerboard structure, imaging the HRR (see also Figure 1, downward left panel); the good resolution achievable by the method used is evident in the volume constrained between 0 and -2700 m (right panels of the same figure). At $Z = -3500$ m, the method resolves at the maximum resolution only a subset of the input volume.

6.4   d) Synthetic anomaly

We performed a second test adopting the procedure described in Schurr et al. (2003), using synthetic data by tracing rays through the real 3-D V_S model, in order to check the effective availability of the results which will be discussed in the following chapter. This test uses as input a Q_S^{-1} model created using anomalies comparable in size to those observed using the real data-set (W-E and S-N sections in Figure 4, panel a) but with slightly different geometries. A 10% normally distributed error was applied to the spectral ratios. The test shows that at maximum resolution the anomalies are generally well recovered between the surface and -3000 m (W-E and S-N sections in Figure 4, panel b). In the depth range between -3000 m and -4500 m the test shows that the resolution decreases. The test is consistent with the checkerboard test (Figure 3, $Z = -3500$ m) and shows that the maximum resolution achievable in this depth range is 900 m.

7   Results.

Using the present multi-resolution method, we obtained the attenuation structure under Mt. Vesuvius in two frequency bands (Table II), centered at 12 and 18 Hz. The images have a resolution of 300 meters in the sub-volumes with high ray coverage marked in Figures 2 and 3 with a white broken line. All the results obtained are shown in Figures 5, 6 and 7, where the depths (negative downward), are calculated respect to the sea level. In Figures 6 and 7 the images relative to the velocity tomography (SCA02) are also shown. The present database is a subset of the database used in the velocity tomography.

13

In Figure 5 the results of S-wave attenuation imaging obtained with both CN and SD are reported for sake of comparison.

Using CN technique, an estimate of the variation of Q_S^{-1} respect to the mean was obtained for the two frequency bands (12 and 18 Hz), where the signal to noise ratio value resulted sufficiently high for this analysis [see Del Pezzo et al. (2006 b)]. These images are reproduced in panels a and b of Figure 5. Using SD technique a unique image at 18 Hz was obtained (panel c).

Images shown in panel a and b of Figure 5 are very similar except for an higher attenuation zone (turquoise) located in a depth range between -2500 and -3500 m centered at 452000 onto the W-E section, visible in panel b.

Comparing panel b and panel c of Figure 5, we notice that in the HRR the images are similar. Outside the HRR slight differences between the two images appear in the W-E section, at a depth of approximately -1000 m, between coordinates 453000 and 454000. In this region CN method (panel b) gives a high attenuation contrast zone whereas the contrary occurs for SD method (panel c). We observed that the SD method produces in general images that are less variable in space respect to those from the CN method.

Figure 6, panel a, reports the W-E and S-N sections of the S- wave attenuation images at 18 Hz; in the same figure the S-wave velocity (panel b), P-wave attenuation (panel c) and P-wave velocity (panel d) for the W-E and S-N sections are also represented. V_P/V_S ratio as a function of depth (calculated as an average over the slices at different depth) is superimposed to all the figures. The color scale in panels a and c represents the variation of the inverse quality factor respect to the mean S- or P-wave attenuation; the color scales of panels b and d represent the absolute S- and P-wave velocity.

Figure 7 represents twenty horizontal slices at the depths $-500, -1000, -2000,$ -2700 and -3500 meters. Color scales represent the differences respect to the average S-wave velocity (first column), S-wave attenuation (second column), P-wave velocity (third column) and P-wave attenuation (fourth column) calculated for each slice. The differences respect to the average show the same pattern of the absolute P- and S- waves velocities and attenuation (in the discussion we will not make any difference between the absolute quantity and the variation respect to the mean), and better enlighten the lateral variations.

8   Discussion

The HRR is localized essentially under the central part of the cone spanning a depth range between +250 and -3500 m (see Figures 2 and 3). In this zone

14

we have thus an S-wave attenuation image with a resolution improved respect to that obtained by Del Pezzo et al. (2006 b) using a single scale approach. Laterally, the resolution becomes lower due to the station density, which is not comparable with the cell dimension [for a wider discussion on station density and resolution see Bai and Greenhalgh (2005)]. In general, the 3-D attenuation pattern shows a Q^{-1} which clearly decreases with depth in the 12 and 18 Hz frequency bands (Figure 5, panels a and b) , showing clearly visible attenuation contrasts localized along the borders of the already known structures (see e.g. SCA02), like the carbonate basement, well visible at the maximum resolution in the Q_S^{-1}, Q_P^{-1}, V_S and V_p images at -1500 meters (see Figures 6, all panels).

8.1 Frequency dependence of the S-wave attenuation

In the HRR the independence of attenuation from frequency is confirmed in the frequency range between 12 and 18 Hz. The panel b of Figure 5 shows an attenuation contrast localized between 452000 and 453000, in the depth range between -2500 and -3500 meters, with a size larger than the minimum resolution. This contrast is not evident in panel a of the same Figure, for the image obtained at 12 Hz, possibly due to the different linear dimensions of the anomalous region sampled by the different wavelength.

8.2 Comparison between CN and SD images

The S-wave images obtained under the cone at 18 Hz with CN and SD methods are quite enough similar, showing on average the same dependency of Q_S^{-1} with depth (Figure 5, panel b and c). In general the images obtained with CN appear much more smoothed than those obtained with SD. In the HRR most of the attenuation contrasts follow the same pattern, being sometimes different in value.

The sole significant differences between CN and SD images can be observed between -1000 m and -2000 m toward North and toward East (corresponding at surface with the geological structure of Mt. Somma). In this volume (Figure 5 panels b and c) the interface between carbonate basement and the overlying volcano materials, is not clearly defined in the SD image. On the other hand, this interface is clearly evidenced by SD method applied to P-waves, and very well defined by the velocity tomography (see also SCA02 and Zollo et al. (2002)).

The discrepancy above discussed may be due to the assumptions that are at the base of CN. In this method S-spectra are normalized by coda spectra, in order

to cancel out the site term. This procedure is based on the experimental result that the coda radiation is uniform for all the source station pairs after a lapse time greater than twice the S-wave travel time. This experimental property of coda waves may be not strictly verified in presence of a non-uniform scattering wave field (Wegler, 2003) that may produce for few waveforms a bias in the normalization of S-spectrum with coda spectrum. Despite this problem, the independence of CN of site transfer function makes CN approach particularly suitable for the application to volcanic areas, where site effects may severely affect the spectrum of S-radiation emitted by the VT earthquakes.

8.3 Joint interpretation of velocity and attenuation images

8.3.1 General pattern

We first analysed the velocity images, isolating the volumes characterized by strong laterally and/or in depth contrasts, velocity inversions, variations from the average V_P/V_S. Then, we associated them with the corresponding volumes in all the other available images. Comparing V_P with Q_P^{-1} and V_S with Q_S^{-1} images (Figures 6, all panels) we observe that high V_P zones correspond roughly to low Q_P^{-1} volumes and that high V_S zones correspond to low Q_S^{-1} volumes; the unique evident exception is the volume located under the central cone, confined in the depth range between -1000 m and -2000 m, where the pattern is characterized by a low V_S and V_P corresponding to high variations in attenuation (Q_S^{-1} and Q_P^{-1} strongly increase with depth).

8.3.2 The shallower structures

In average, the attenuation of the S- and P-waves increases toward North and East in all the images for the volumes above the sea level (Figure 6, panels a and c); interestingly, the S-N section of the Q_S^{-1} image (panel a) shows a low attenuation inclusion (green surrounded by orange, not included in the HRR) with dimension of the order of a 900 meters , corresponding to the structure of Mt. Somma, the ancient caldera border. This structure surrounds the central cone in the North and East quadrants (Figure 1, down left) and is characterized by higher rigidity older age lavas.

 In the HRR (marked with a broken white line in Figure 2, panel b), velocity and attenuation images clearly evidence the presence of a contrast between the structure above and the volume underneath the depth of 0 meters; this contrast marks the first interaction between the recent products of the volcano activity and the older higher rigidity materials.

A low attenuation zone [roughly surrounded by the rectangle **1**] is strongly

correlated with an high V_S and V_p zone in the same position, as shown in Figure 7 ($Z = -500$ meters). This zone is located inside the HRR (see Figure 3, panel a) and may represent the residual lava emitted during the last eruptions, completely solidified in the present time.

In the same slice (Figure 7 , $Z = -500$) we observe that the western part is characterized by low Q_S^{-1}, high Q_P^{-1} and low V_P/V_S . This features, in particular the opposite pattern of Q_S^{-1} and Q_P^{-1} , may be compatible with the presence of a CO_2 reservoir (Hansen et al., 2004). This interpretation is corroborated by the presence of the above discussed low attenuating body in the central part of the Figure. As reported by Hansen et al. (2004), when the magma rises, the decrease in confining pressure causes the magma to decompress and the biggest part of CO_2 exsolves; however, when the magma cools, a modest amount of CO_2 can be definitely trapped in the rock matrix, and could explain the observed low V_P and low V_P/V_S anomalies (Gerlach and Taylor, 1990). This interpretation is confirmed by the laboratory experiments of (Ito et al. (1979), Spencer (1979), Sengupta and Rendleman (1989)). Summarizing the results from these papers, at pressure below the saturation pressure (as should be at a depth of -500 meters), the presence of gas can lead to a decrease in V_S and V_P, an increase of Q_S^{-1}, and an anomalous decrease of Q_P^{-1}, that is the same pattern observed for Mt. Vesuvius.

The presence of melt or partially melt rocks would lead to a low V_P, a low V_S, high V_P/V_S ratio, high Q_P^{-1} and high Q_S^{-1}. In the depth range around -500 m there is consequently no evidence supporting the presence of patches of magma with dimensions larger than cell size.

8.3.3 The intermediate structure

A zone of strong lateral contrast is evident in both the V_P and V_S images [the zone surrounded by the rectangle marked by number **2** in the slices of Figure 7 ($Z = -1000$)] . In this zone there is no correspondence of the increasing velocity with decreasing attenuation, as already discussed in the "General pattern" section. The low attenuation area marked by the white rectangle **1** in Figure 7 ($Z = -1000$m) corresponds instead to an high velocity area. This area is a section of the anomalously high-velocity volume (figure 6, panels b and d) which seems to intrude from depth, in agreement with the interpretation reported in several velocity tomography studies [Zollo et al. (2002), Tondi and De Franco (2003), De Natale et al. (2005), SCA02], and interpreted as related to the residual part of solidified lava from the last eruption. This high attenuation and velocity zone is connected with the area marked by line **1** in Figure 7, $Z = -500$ m.

To refine the interpretation in the depth range around -1000 m, especially

17

for the area marked by rectangle **2** in Figure 7, we focus the attention on the W-E and S-N sections in Figures 6 [all panels]. The zone corresponding in depth with the maximum value of the V_P/V_S ratio roughly corresponds to the interface between high attenuation and low attenuation. This interface is also characterized by low V_P and low V_S. All these observations may be interpreted as due to the presence of a fractured medium permeated by fluids, as discussed in Hansen et al. (2004) and Eberhart-Phillips et al. (2004). In this interpretation the presence of a shallow patch of magma in the same depth range should be excluded, in the limit of the spatial resolution: in fact, the attenuation images do not show any particular evidence of melt, that, if present, should have produced both high Q_P^{-1} and high Q_S^{-1}. These results are in agreement with the previous interpretation done by SCA02 on the base of the ole velocity tomography, and are also corroborated by geochemical studies, that locate an hot aquifer under the cone just in the same position (Marianelli et al. (1999), Chiodini et al. (2001)). The properties observed at $Z = -1000$ m can be observed also at $Z = -2000$ m (see Figure 7). In particular a secondary maximum in the V_P/V_S ratio can be observed at -2000 m. The vertical sections of Q_P^{-1} and Q_S^{-1} (Figure 6 panels a and c) indicate the presence of a high attenuation zone, around -2000 m, included in a low attenuation body. This pattern can be interpreted as an highly cracked medium filled by fluids, in agreement with geochemical studies (Chiodini et al., 2001).

8.3.4 The deepest structure

The V_P, V_S and V_P/V_S patterns between -2500 m and -4000 m (Figures 6, panels b and d) are more regular. The $Z = -2700$ and $Z = -3500$ slices of Figure 7 help in better understanding the velocity and attenuation features. The pattern of Q_P^{-1} and Q_S^{-1} are similar at $Z = -2700$ (Figure 7 and Figure 3), both in the HRR and in the LRR. Focusing the attention on the central part of the attenuation images (rectangle **3**), a high contrast in both Q_S^{-1} and Q_P^{-1}, not perfectly matching the contrast in both V_P and V_S can be observed. The imperfet match may be due to a lack of resolution of attenuation imaging in this depth range.

At $Z = -3500$ m, the decreasing attenuation corresponds to the increasing velocity outside rectangle 4, for both P and S waves. A low velocity and attenuation zone corresponding to the South-East sector of Figure 7 at $Z = -3500$ m is clearly visible, and marked with the rectangle **4**. In this region the low V_P/V_S ratio excludes the presence of partially melt rocks or fluid inclusions, suggesting on the contrary the presence of a cracked volume. This zone is spatially coincident with the zone of maximum seismic energy release, as shown in Figure 1 (upper-left and upper-right panels, the grey ellipsoidal line marked by number **3**).

9 Conclusions.

The present paper complements a previous preliminary study of the same area, which was carried out in a smaller volume respect to that used in the present study. The present paper uses a multi-resolution approach, which solves a 300 m cell size in the volume beneath the central crater located in the depth range between approximately 0 (the sea level) and -3500 m. The new study is based a data set improved respect to the first one (the number of waveforms in the present study is more than doubled respect to the previous), improving both stability and robustness. The improved resolution allowed a better definition of the 3-D pattern for both Q_P^{-1} and Q_S^{-1}, thus improving the joint interpretation of previous velocity images with the present attenuation structure. The essential results show that no magma patches with dimensions larger than the cell size are visible in the images and confirm the presence of shallow hydrothermal reservoirs (between -700 and -2300 m) evidenced by geochemical studies. The high resolution achievable between 0 and -1500 m allowed a small scale imaging of the residual solidified lava emitted during the last eruptions, leading to the interpretation in terms of large patches of gas located in the first kilometer below sea level. Interestingly, the zone of maximum seismic energy release, imaged for the first time at a resolution of 900 meters, coincides with a high attenuation and low velocity anomaly, easily interpretable as due to the presence of a cracked zone inside the limestone layer. These results are expected to add important constraints for the numerical models that will be adopted to simulate the next eruption, and consequently to be used for Civil Defense purposes.

10 Appendix 1

10.1 Coda Normalization Method.

As well known, the S-wave seismic energy density spectrum decays as a function of lapse-time as:

$$E_{ij}(f, r) = S_i(f)\theta_{ij}(\vartheta, \phi)I_j(f)T_j(f)\frac{1}{r_{ij}^2}\exp(-2\pi f\frac{t_{ij}(r)}{Q_T^{ij}(r)}) \qquad (16)$$

where $E(f, r)$ is the energy density spectrum of the S-wave radiation emitted by the source i at total distance r measured along the ray-path connecting source(i) and station (j) ; f is the frequency. $S_i(f)$ is the energy spectrum at source, modulated by the radiation pattern function $\theta(\vartheta, \phi)$. I_j is the instrument transfer function and T_j is the site transfer function. t_{ij} is the travel time

along the ray whose length is r_{ij} and Q_T^{ij} is the total quality factor measured along the ray-path.

The coda energy spectrum evaluated around a given lapse time, t_c, can be considered as a function of the "average" medium properties and expressed as in Sato and Fehler (1998):

$$E^C(f,t) = S_i(f)I_j(f)T_j(f)P(f,t_c) \tag{17}$$

where $P(f,t_c)$, is independent on both source-receiver distance and directional azimuth and depends only by the earth medium. The radiation pattern term $\theta_{ij}(\vartheta,\phi)$ disappears due to the well known property of natural space averaging of coda waves (Aki, 1980). For sake of simplicity, we assume the validity of the single scattering model, but in principle equation (17) is independent of any scattering model. Dividing eq. (16) for eq. (17) for each source-station pair, at lapse time t_c, we obtain

$$\frac{E_{ij}(f,r)}{E^C(f,t)}r_{ij}^2 = \frac{\theta_{ij}(\vartheta,\phi)}{P(f,t_c)}\exp\left[-2\pi f\int_{rij}\frac{dl}{v(l)Q_T^{ij}(l)}\right] \tag{18}$$

The spectral ratio at the left side of formula (18) is independent of energy level at source, site and instrument transfer function. In eq. (18) the attenuation operator has been substituted with the path integral along the seismic ray, where $v(l)$ is the velocity along the path l. $\theta_{ij}(\vartheta,\phi)$ in principle depends on source azimuth ϕ and incidence angle ϑ. For a complete review of the method see Del Pezzo et al. (2006 b). In Appendix 2 we test the independence of the spectral ratio of formula (18) of radiation pattern for ratios evaluated on signal time windows longer than 2.5 seconds. In this case $\theta_{ij}(\vartheta,\phi)$ can be set equal to unity.

11   Appendix 2

11.1   Test for the independence of radiation pattern.

Using the properties of the early-coda, Gusev and Abubakirov (1999) developed an empirical method to test the independence of S-wave spectra from radiation-pattern, when the spectrum is estimated in a time window of duration much greater than the source duration. We make a similar test for the spectral ratio between S and coda energy spectra calculated for the earthquakes of Mt. Vesuvius. We consider for each ray connecting the source to the receiver, the quantity:

$$A = \frac{LR}{M} \tag{19}$$

where L is the ray length, R is the spectral ratio between energies of formula (18) and $M = \exp(-\pi f r / V Q_{mean})$, with V indicating the average S-wave velocity, is the average anelastic attenuation in the area. A is implicitly dependent only on the radiation pattern, R being independent of site and instrument effects. The percent standard deviation ($\sigma_A / < A >$) calculated averaging A over the stations for a single earthquake, is plotted for different time window durations in Figure A2.1; this quantity abruptly decreases with increasing duration of the time window, as expected. We applied a statistical test [the "change point" test of Mulargia and Tinti (1985)] to estimate the "change point" of the pattern of A respect to the duration of the time window in which is calculated. The pattern results to be steady after 2.5 seconds at 99% confidence. Consequently, the radiation-pattern effects become negligible for time windows with a duration greater than 2.5 s. We interpret this result as due to the natural processes of averaging the radiation pattern effects that takes place in a ray-tube centered along the ray-path. The forward scattered radiation that arrives at the receiver soon after the ballistic (direct) arrival is contained inside this ray-tube(Gusev and Abubakirov, 1999). For the above reasons we assume that $\theta_{ij}(\vartheta, \phi)$ of eq. 18 is identically equal to unity.

12   Appendix 3

In this Appendix we explain the details relative to the points listed between 2 and 5 in the section 5

Point 2: estimate of the Average inverse Quality Factor (AQF).

S-waves AQF is calculated using the coda normalization method applied to the whole data-set ; the eq. (2) becomes:

$$d_k^C = \frac{1}{2\pi f} \ln(\frac{1}{P(f, t_c)}) - \sum_{b=1}^{N\_cells} l_{kb} s_b \left[Q_T^{-1} \right]^C \tag{20}$$

where $<>$ indicates the average over We obtained the inverse AQF for S waves (Q_T^{-1}):

$$(Q_T^{-1})^{12} = 0.010 \pm 0.003$$
$$(Q_T^{-1})^{18} = 0.019 \pm 0.003$$

where the above index is referred to the center frequency.

Uncertainty is estimated assuming that each spectrum is affected by a 10% of error due to the noise. This result is in good agreement with previous Q-estimate for S waves in the area (Del Pezzo et al., 2006 a).

P-waves AQF has been already calculated by Bianco et al. (1999).

Point 3: cell dimension of 1800 m.

The inversion problem of eq. (3) and (12) is solved for a grid of 1800 meters step. We can rewrite the equation as:

$$\tilde{d}_k^{C,D} = \sum_{b=1}^{N\_cells\_1800} G_{kb}^{1800}[(\delta Q_b^{1800})^{-1}]^{C,D} \tag{21}$$

where the superscript 1800 stands for the step of the grid, while the superscript C, D takes into account the different methods used. The elements of the inversion matrix, G_{kb}^{1800}, are the length of the $k-th$ ray segment in the 1800-meter side $b-th$ block, l_{kb}^{1800} , multiplied for his slowness s_b^{1800}:

$$G_{kb}^{1800} = l_{kb}^{1800} s_b^{1800} \tag{22}$$

Applying eq. (14), we consider only blocks crossed by at least $n_R = 35$ rays. The problem is solved separately for each frequency band. We solve the problem using the least squares algorithm "lsqlin" deployed in MATLAB.

The percentage reduction of the residuals, computed using the formula in Gubbins (2004), results to be 65%. The inverse quality factor of each 1800 meters block b is given by:

$$(Q_b^{1800})^{-1} = Q_T^{-1} + (\delta Q_b^{1800})^{-1} \tag{23}$$

Point 4: cell dimension of 900 meters.

The data vector obtained solving the inversion schemes of eq. (4) and (13) can be updated with the solutions obtained in the previous steps. Each ray crosses a medium whose quality factor is no more Q_T, and is affected by the quality factors of the cube that it effectively crosses. The elements of the data vector must represent the effect of the attenuation structure obtained in the previous steps. They become respectively:

$$(\tilde{d}_k^C)^{1800} = < \frac{1}{2\pi f} \ln(\frac{1}{P(f,t_c)}) > -d_k^C - Q_T^{-1} \sum_{b=1}^{N\_cells\_900} l_{kb}^{900} s_b^{900}$$
$$- \sum_{b=1}^{N\_cells\_900} l_{kb}^{900} s_b^{900} (\delta Q_b^{-1})^{1800,C} \tag{24}$$

and

$$(\tilde{d}_k^D)^{1800} = < \frac{t_k}{Q_k} >^{1800} - d_k^D - Q_T^{-1} \sum_{b=1}^{N\_cells\_900} l_{kb}^{900} s_b^{900} -$$

$$\sum_{b=1}^{N\_cells\_900} l_{kb}^{900} s_b^{900} (\delta Q_b^{-1})^{1800,D} \quad (25)$$

where $(\delta Q_b^{-1})^{1800,C}$ and $(\delta Q_b^{-1})^{1800,D}$ are respectively the solutions obtained with the CN method and the SD method for 1800 meters side blocks and that where assigned to the N_cells_900 blocks of 900 meters side crossed by the $k-th$ ray. In the SD method the constant value $< \frac{t_k}{Q_k} >^{1800}$ has also been updated with the informations obtained in the previous step. The inversion problem becomes, for a resolution of 900 meters:

$$(\tilde{d}_k^{C,D})^{1800} = \sum_{b=1}^{N\_cells\_900} G_{kb}^{900} [(\delta Q_b^{900})^{-1}]^{C,D} \quad (26)$$

where the superscript 900 stands for the step of the grid and the $(\delta Q_b^{900})^{-1}$ are the inverse variations respect the inverse quality factor of the 1800 meters cube in which they are contained. The elements of the inversion matrix, G_{kb}^{900}, are the length of the $k-th$ ray segment in the 900-meters side $b-th$ block l_{kb}^{900} multiplied for his slowness s_b^{900}:

$$G_{kb}^{900} = l_{kb}^{900} s_b^{900} \quad (27)$$

where, we consider only blocks crossed by at least $n_R = 17$ rays see equation (14). The inversion is linear and we can constrain the average of the $(\delta Q_b^{900})^{-1}$ to be zero. The inverse quality factor of each 900 meters block b is given by:

$$(Q_b^{900})^{-1} = Q_T^{-1} + (\delta Q_b^{1800})^{-1} + (\delta Q_b^{900})^{-1} \quad (28)$$

while the percentage reduction is 70% in residual.

Point 5: cell dimension of 300 meters.

The last step is achieved upgrading the data vectors writing the following two formulas:

$$(\tilde{d}_k^C)^{900} = < \frac{1}{2\pi f} \ln(\frac{1}{P(f,t_c)}) > - d_k^C - Q_T^{-1} \sum_{b=1}^{N\_cells\_300} l_{kb} s_b -$$

$$\sum_{b=1}^{N\_cells\_300} l_{kb} s_b (\delta Q_b^{-1})^{1800,C} - \sum_{b=1}^{N\_cells\_300} l_{kb} s_b (\delta Q_b^{-1})^{900,C} \quad (29)$$

and

$$(\tilde{d}_k^D)^{900} = < \frac{t_k}{Q_k} >^{900} - d_k^D - Q_T^{-1} \sum_{b=1}^{N\_cells\_300} l_{kb}s_b -$$
$$\sum_{b=1}^{N\_cells\_300} l_{kb}s_b(\delta Q_b^{-1})^{1800,D} - \sum_{b=1}^{N\_cells\_300} l_{kb}s_b(\delta Q_b^{-1})^{900,D} \quad (30)$$

where $(\delta Q_b^{-1})^{900,C}$ and $(\delta Q_b^{-1})^{900,D}$ are the solutions obtained in the previous steps that were assigned to a number of N_cells_300 blocks of 300 meters side, crossed by the $k - th$ ray. As before, the constant value $< \frac{t_k}{Q_k} >^{900}$ has been updated with the informations obtained in the previous steps. The inversion problem becomes:

$$(\tilde{d}_k^{C,D})^{900} = \sum_{b=1}^{N\_cells\_300} G_{kb}^{300}[(\delta Q_b^{300})^{-1}]^{C,D} \quad (31)$$

where the superscript 300 stands for the grid step, and the elements of the inversion matrix, G_{kb}^{300}, are given by the length of the $k - th$ ray segment in the $b - th$ block, l_{kb}^{300}, multiplied for his slowness s_b^{300}:

$$G_{kb}^{300} = l_{kb}^{300} s_b^{300} \quad (32)$$

applying eq. (14), we consider only blocks crossed by at least $n_R = 5$ rays. The percentage reduction in residual is 94%. The inverse quality factor of each 300 meters block b is given by:

$$(Q_b^{300})^{-1} = Q_T^{-1} + (\delta Q_b^{1800})^{-1} + (\delta Q_b^{900})^{-1} + (\delta Q_b^{300})^{-1} \quad (33)$$

13   Acknowledgements.

References

Andronico, D., Calderoni, G., Cioni, R., Sbrana, A., Suplizio, R., and Santacroce, R., 1995. *Geological map of Somma-Vesuvius Volcano.* Per. Mineral., 64: 77-78.

Aki, K., 1980. *Attenuation of shear-waves in the lithosphere for frequencies from 0.05 to 25 Hz.* Phys. Earth Planet. Inter., 21: 50-60.

Auger, E., Gasparini, P., Virieux, J., and Zollo, A., 2001. *Seismic Evidence of an Extended Magmatic Sill Under Mt. Vesuvius.* Science, 294: 1510-1512.

Bai, C., and Greenhalgh, S., 2005. *3D multi-step travel time tomography: imaging the local, deep velocity structure of Rabaul volcano, Papua New Guinea.* Physics of the Earth and Pl. Int., 151: 259-275.

Berrino, G., Coppa, U., De Natale, G., and Pingue, F., 1993. *Recent geophysical investigation at Somma–Vesuvius volcanic complex.* J. Volcanol. Geotherm. Res., 58: 239-262.

Bianco, F., Castellano, M., Milano, G., Ventura, G., and Vilardo, G., 1997. *The Somma-Vesuvius stress field induced by regional tectonics: evidences from seismological and mesostructural data.* J. Volcanol. Geotherm. Res., 82: 199-218.

Bianco, F., Castellano, M., Del Pezzo, E., and Ibanez, J. M., 1999. *Attenuation of short period seismic waves at Mt. Vesuvius, Italy.* Geophys. J. Int., 138: 67-76.

Block, L.V., 1991. *Joint hypocenter-velocity inversion of local earthquakes arrival time data in two geothermal regions.* Ph.d. dissertation, M.I.T., Cambridge.

Capuano, P., Gasparini, P., Zollo, A., Virieux, J., Casale, R., and Yeroyanni, M., 2003. *The internal structure of Mt. Vesuvius. A seismic tomography investigation.* Liguori Editore, ISBN 88-207-3503-2.

Chiodini, G., Marini, L., and Russo, M., 2001. *Geochemical evidence for the existence of high-temperature hydrothermal brines at Vesuvio volcano, Italy.* Geoch. et Cosmoch. Acta, 65(13), 2129– 2147.

Chouet, B., 1996. *New methods and future trends in seismological volcano monitoring.* In: Scarpa, R., Tilling, R.I. (Eds.), *Monitoring and Mitigation of Volcano Hazards.* Springer, Berlin, pp. 23–97.

Chouet, B., 2003. *Volcano Seismology.* Pageoph, 160: 739-788.

Del Pezzo, E., Bianco, F., and Saccorotti, G., 2004. *Seismic source dynamics at Vesuvius volcano, Italy.* J. Volcanol. Geotherm. Res., 133: 23-39.

Del Pezzo, E., Bianco, F., and Zaccarelli, L., 2006. *Separation of Qi and Qs from passive data at Mt. Vesuvius: a reappraisal of seismic attenuation.* Physics of the Earth and Pl. Int., 159: 202–212.

Del Pezzo, E., Bianco, F., De Siena, L., and Zollo A., 2006. *Small scale shallow attenuation structure at Mt. Vesuvius, Italy.* Physics of the Earth and Pl. Int., 157: 257-268.

De Natale, G., Capuano, P., Troise, C., and Zollo, A., 1998. *Seismicity at Somma-Vesuvius and its implications for the 3D tomography of the volcano.*

J. Volcanol. Geotherm. Res., Special Issue Vesuvius. Spera F. J., De Vivo B., Ayuso R.A., Belkin H.E. (Eds), 82: 175-197.

De Natale, G., Troise, C., Pingue, F., Mastrolorenzo, G., and Pappalardo, L., 2005. *The Somma–Vesuvius volcano (Southern Italy): Structure, dynamics and hazard evaluation.* Earth-Science Rev., 74: 73-111.

Eberhart-Phillips, D., 1990. *Three-dimensional P and S velocity structure in the Coalinga region, California.* J. Geophys. Res. 95: 15343–15363.

Eberhart-Phillips, D., Reyners, M., Chadwick, M., Chiu, J. M., 2005. *Crustal heterogeneity and subduction processes: 3-D V_P, V_P/V_S and Q in the southern North Island, New Zealand.* Geophys. J. Int. 162: 270–288.

Galluzzo, D., Del Pezzo, E., Maresca, R., La Rocca, M., and Castellano, M., 2005. *Site effects estimation and source-scaling dynamics for local earthquakes at Mt. Vesuvius, Italy.* Congress acts, ESG2006, Grenoble. Paper num. 36.

Gerlach, T., and Taylor, B., 1990. *Carbon isotope constraints on degassing of carbon dioxide from Kilauea volcano.* Geochim. Cosmochim. Acta 54, 2051–2058.

Giampiccolo, E., Gresta, S. and Ganci, G., 2003. *Attenuation of body waves in Southeastern Sicily (Italy).* Physics of the Earth and Pl. Int., 135: 267–279.

Gubbins, D., 2004. *Time series analysis & inverse theory for geophysicists.* Cambridge University Press.

Gudmundsson Ó., Finlayson D. M., Itikarai I., Nishimura Y., and Johnson W. R., 2004. *Seismic attenuation at Rabaul volcano, Papua New Guinea.* J. of Volc. and Geoth. Re., 130: 77-92.

Gusev, A. A., and Abubakirov, I. R., 1999. *Vertical profile of effective turbidity reconstructed from broadening of incoherent body-wave pulses.* Geophys. J. Int., 136: 309-323.

Hansen, S., Thurber, C. H., Mandernach, M., Haslinger, F., and Doran, C., 2004. *Seismic Velocity and Attenuation Structure of the East Rift Zone and South Flank of Kilauea Volcano, Hawaii.* Bull. of the Seism. Soc. of Am., 94: 1430-1440.

Ito, H., DeVilbiss, J., and Nur, A., 1979. *Compressional and shear waves in saturated rock during water–steam transition.* J. Geophys. Res. 84, 4731–4735.

Lomax, A., Zollo, A., Capuano, P., and Virieux, J., 2001. *Precise absolute earthquake location under Somma-Vesuvius volcano using a new three-dimensional velocity model.* Geophys. J. Int., 146: 313-331.

Marianelli, P., M´etrich, N., and Sbrana, A., 1999. *Shallow and deep reservoirs involved in magma supply of the 1944 eruption of Vesuvius.* Bull. Volcanol., 61: 48-63.

Mulargìa, F., and Tinti, S., 1985. *Seismic sample areas defined from incomplete catalogues; an application to the Italian territory.* Phis. Earth Plan. Int, 40: 273-300.

Alejandro Nava, F., Garcìa-Arthur, R., Castro, R. R., Suàrez, C., Màrquez, B., Nùñez-Cornù, F., Saavedra, G. and Toscano, R., 1999. *S wave attenuation*

in the coastal region of Jalisco–Colima, México. Phys. Earth Pl. Int., 115: 247–257.

Santacroce, R., 1987. *Somma-Vesuvius.* CNR, Quaderni di Ricerca Scientifica.

Sambridge, M.S., and Gudmundsson, O., 1998. *Tomographic systems of equation with irregular cells.* J. Geophys. Res., 103: 773–781.

Sato, H., and Fehler, M.C.,1998. *Seismic Wave Propagation and Scattering in the Heterogenous Earth.* Springer.

Sengupta, M. K., and Rendleman, C. A., 1989. *Case study: the importance of gas leakage in interpreting amplitude-versus-offset (AVO) analysis.* Soc. Explor. Geophys. Abstracts 59, 848–850.

Scarpa, R., Tronca, F., Bianco, F., and Del Pezzo, E., 2002. *High resolution velocity structure beneath Mount Vesuvius from seismic array.* Geophys. Res. Lett., 29 (21): 2040.

Schurr, B., Asch, G., Rietbrock, A., Trumbull, R., and Haberland, C., 2003. *Complex patterns of fluid and melt transport in the central Andean subduction zone revealed by attenuation tomography.* Earth. Pl. Scien. Lett., 215: 105-119.

Spencer, J., 1979. *Bulk and shear attenuation in Berea sandstone: the effects of pore fluids.* J. Geophys. Res. 84, 7521–7523.

Thurber, C.H., 1987. *Seismic structure and tectonics of Kilauea volcano Hawaii.* In: Decker, R.W., Wright, T.L., Stauffer, P.H. (Eds.), Volcanism in Hawaii. US Geological Survey, pp. 919–934.

Tondi, R., and De Franco, R., 2003. *Three-dimensional modeling of Mount Vesuvius with sequential integrated inversion.* J. Geophys. Res., 108: 2256.

Um, J., and Thurber, C.H., 1987. *A fast algorithm for two-point seismic ray tracing.* Bull. of the Seism. Soc. of Am. 77: 972-986.

Wegler, U., 2003. *Analysis of multiple scattering at Vesuvius volcano, Italy, using data of the Tomoves active seismic experiment.* J. Volcanol. Geotherm. Res., 128: 45–63.

Zollo, A., D'Auria, L., De Matteis, R., Herrero, A., Virieux, J., and Gasparini, P., 2002. *Bayesian Estimation of 2-D P-Velocity Models From Active Seismic Arrival Time Data: Imaging of the Shallow Structure of Mt.Vesuvius (Southern Italy).* Geophys. J. Int., 151: 566-582.

14   Captions.

- Figure 1:Lower-left panel: Map of Mt. Vesuvius with station positions (black squares) and hypocentral locations (white dots) of the seismic events used in the present work. Black broken line depicts the old caldera rim. Upper-left and upper-right panels represent respectively the W-E and S-N sections, also reported as "W-E plane" and "S-N plane" in the lower-right "wide angle" view. The High Resolution Region (HRR) is roughly depicted by the inner polyhedron in the wide angle view. The solid line rectangles in

the upper left, upper right and lower left panels represent the sections of the HRR. The zones marked with 1and 2 represent the zone in which the robusteness test results are reported respectively in Table IV and V. The ellipsoidal zone marked with 3 shows the area with the maximum seismic energy release.

- Figure 2: Checkerboard test in the HRR. a) Input. W-E and S-N sections (also marked in figure 1, lower right panel); the white lines include all the maximum resolution cells defined by formula (14). In this volume we assumed a checkerboard structure, with high Q-contrast among the blocks; a uniform attenuation medium is assumed outside HRR. b) Output. Test results for a 10% error on synthetic data. The zones marked by the white broken lines include the cells where the checkerboard structure is effectively reproduced. ΔQ_S^{-1} grey scales represent the variation from the average quality factor.

- Figure 3: Left hand panels. Five horizontal slices at different depths (Z value respect to the sea level) of the volume containing the HRR. The white lines include all the maximum resolution cells defined by formula (14). The sections represent the input checkerboard structure also described in Figure 3, with the same colorscale. Rigth hand panels. The figures represent the test output; the zones marked by the white broken lines include the cells where the checkerboard structure is effectively reproduced.

- Figure 4: Synthetic anomaly test. The input structures (panel a) are included in a volume characterized by uniform attenuation. The output (panel b) show the reconstruction of the anomalies. Black areas are not resolved in the inversion. Colorscales refer to the variations respect to the mean inverse quality factor. The zones marked by the white broken lines include the cells where the checkerboard structure is effectively reproduced.

- Figure 5: Results of the attenuation tomography inversion, in the frequency band centered at 12 Hz (panel a), and 18 Hz (panel b) for the CN method, compared with the results obtained at 18 Hz for the SD method (panel c). W-E and S-N sections are those marked in Figure 1 (down-rigth panel). Black areas are not resolved in the inversion.Colorscales refer to the variations respect to the mean inverse quality factor. The zones marked by the white broken lines include the cells where the checkerboard structure is effectively reproduced.

- Figure 6: The W-E and S-N sections represent the attenuation structure inferred for S-waves (CN method), in the frequency band centered at 18 Hz (panel a), and the S-velocity structures inferred by Scarpa et al. (2002) (panel b). The dashed line represents the V_P/V_S pattern with depth and is overimposed to all figures. The P-wave attenuation (SD method, 18 Hz) and velocity (inferred by Scarpa et al. (2002)) are also represented in panels c and d. The colorscales in panels a and c refer to the variations respect to the mean inverse quality factor obtained in the inversions for S- and P-waves. The colorscales in panels b and d represent the absolute S- and P-wave velocity. Black areas are not resolved in the inversion. The zones marked by

the white broken lines include the cells where the checkerboard structure is effectively reproduced.

- Figure 7: Five horizontal slices of the the volume containing HRR at different depths (Z). The colorscales for S- (first column) and P-wave (third column) attenuation images represent the variations from the mean inverse quality factor calculated on each horizontal slice at each depth. The colorscales represented in the second and fourth coloumns respectively represent the variations of S- and P-wave velocity from the average velocity calculated at each depth. On each image we marked with numbered black rectangles, the zones characterized by important properties, widely discussed in the text. The zones marked by the white broken lines include the cells where the checkerboard structure is effectively reproduced.

- Figure A2.1: The percent standard deviation, σ/μ, as a function of the window duration for an earthquake recorded at all the stations. σ/μ is obtained calculating the average, μ [over stations] , of the log of spectral ratio between direct S radiation and coda radiation, after correcting the amplitudes for geometrical spreading and for the average Q. Downward arrow indicates the change-point as discussed in the text.

Table I

Station	E-W (UTM)	N-S (UTM)	altitude (a.s.l.) (m)
BAFM	450372	4518076	594
BKEM	452677	4518762	850
BKNM	451875	4520020	865
FTCM	452692	4516337	350
OVO	449190	4519705	600
POLM	447910	4522499	181
SGVM	450568	4518706	734

Table II

$-\Delta f$	$f_c(Hz)$	$+\Delta f$
8.2	12	15.8
12.4	18	23.6

Table III

Robusteness Test - 1800 m

Block#	1	2	3	4	5	6	7	8	9	10	11	12
P^{1800}, 10%	1%	0%	0%	13%	7%	4%	0%	0,1%	0%	0%	0%	3%
P^{1800}, 20%	1%	0%	2%	29%	9%	11%	17%	1%	0%	0%	0%	3%
P^{1800}, 30%	2%	1%	3%	28%	9%	9%	50%	0,3%	0%	0%	0%	2%
P^{1800}, 40%	3%	3%	10%	29%	8%	16%	87%	2%	1%	0%	0%	8%
P^{1800}, 50%	6%	2%	11%	62%	20%	25%	87%	3%	1%	0%	0%	9%

Robustness test at the lowest resolution; the average percentageof eq. (15) is represented for all the blocks resolved. The increasing percentage in the first column is the data reduction.

Table IV

Robusteness Test - 900 m

Block#	1	2	3	4	5	6	7	8
P^{900}, 10%	1%	15%	2%	1%	10%	1%	31%	1%
P^{900}, 20%	1%	13%	15%	1%	12%	8%	$> 100\%$	1%
P^{900}, 30%	1%	21%	15%	1%	16%	9%	$> 100\%$	1%
P^{900}, 40%	2%	53%	29%	2%	30%	7%	$> 100\%$	2%
P^{900}, 50%	2%	58%	72%	2%	40%	11%	$> 100\%$	2%

Robustness test at the intermediate resolution; the average percentage of eq. (15) is represented for the 8 blocks in which the single 1800 meters side block of $(Q_b^{1800})^{-1} = 0.0128$ wich includes the cone was divided. The increasing percentage in the first column is the data reduction.

Table V

Robusteness Test - 300 m

Block#	1	2	3	4	5	6	7	8
P^{300}, 10%	12%	16%	21%	59%	30%	5%	1%	14%
P^{300}, 20%	37%	90%	54%	99%	17%	48%	90%	70%
P^{300}, 30%	$> 100\%$	$> 100\%$	67%	$> 100\%$	69%	$> 100\%$	98%	$> 100\%$

Robustness test at the highest resolution; the average percentage of eq. (15) is represented for 8 blocks contained in a single 900 meters side block of $(Q_b^{900})^{-1} = 0.0110$. The increasing percentage in the first column is the data reduction.

Table VI

Stability Test - 1800 m

Block#	1	2	3	4	5	6	7	8	9	12
$[(Q^{1800})^{-1}] \times 10^{-2}$	1,98	1,79	1,50	2,44	1,28	1,37	0,92	2,86	0,51	3,16
$[(Q^{1800})^{-1}] \times 10^{-2}, (Q_T^{\min})^{-1}$	1,83	1,67	1,72	1,84	1,28	1,43	1,15	2,72	0,49	3,21
$[(Q^{1800})^{-1}] \times 10^{-2}, (Q_T^{\max})^{-1}$	1,88	1.69	1,10	2,88	1,11	1,08	0,54	2,74	0,40	2,81

Stability test at the lowest resolution; the value of the inverse quality factor of each resolved block is dependent on the maximum $((Q_T^{\max})^{-1} = 0.026)$ and minimum $((Q_T^{\min})^{-1} = 0.008)$ average inverse quality factor allowed.

Table VII

Stability Test - 900 m

Block#	1	2	3	4	5	6	7	8
$[(Q^{900})^{-1}] \times 10^{-2}$	1,79	0,52	0,96	1,79	2,75	1,64	0	1,79
$[(Q^{900})^{-1}] \times 10^{-2}, (Q_T^{\min})^{-1}, (Q_{b\min}^{1800})^{-1}$	1,88	0,46	1,12	1,88	2,36	1,77	0	1,88
$[(Q^{900})^{-1}] \times 10^{-2}, (Q_T^{\max})^{-1}, (Q_{b\max}^{1800})^{-1}$	1.67	0,58	0,80	1,67	3,14	1,51	0	1,67

Stability test at the intermediate resolution; the value of each inverse quality factor is both dependent on the maximum $((Q_T^{\max})^{-1} = 0.026)$ and minimum $((Q_T^{\min})^{-1} = 0.008)$ average inverse quality factor and the maximum $((Q_{b\max}^{1800})^{-1} = 0.0188)$ and minimum $((Q_{b\min}^{1800})^{-1} = 0.0167)$ inverse quality factor of the block in which they are contained.

Table VIII

Stability Test - 300 m

Block#	1	2	3	4	5	6	7	8
$[(Q^{300})^{-1}] \times 10^{-2}$	$5,61$	$1,78$	$1,91$	$0,39$	$1,44$	0	$2,26$	0
$[(Q^{300})^{-1}] \times 10^{-2}, (Q_{T\,\min})^{-1}, (Q_{b\,\min}^{1800})^{-1}, (Q_{b\,\min}^{900})^{-1}$	$2,59$	$1,76$	$1,34$	$0,05$	$1,29$	0	$2,60$	0
$[(Q^{300})^{-1}] \times 10^{-2}, (Q_{T\,\max})^{-1}, (Q_{b\,\max}^{1800})^{-1}, (Q_{b\,\min}^{900})^{-1}$	$6,91$	$1,99$	$2,01$	$1,59$	$1,32$	0	$1,34$	0

Stability test at the highest resolution; the value of each inverse quality factor is both dependent on the maximum $((Q_T^{\max})^{-1} = 0.026)$ and minimum $((Q_T^{\min})^{-1} = 0.008)$ average inverse quality factor. It is also dependent on the maximum $((Q_{b\,\max}^{1800})^{-1} = 0.0188, (Q_{b\,\max}^{900})^{-1} = 0.0177)$ and minimum $((Q_{b\,\min}^{1800})^{-1} = 0.0167, (Q_{b\,\min}^{900})^{-1} = 0.0151)$ inverse quality factor of the blocks in which they are contained.

MS. REF. NO.: PEPI-D-07-00301
TITLE: MULTIPLE RESOLUTION SEISMIC ATTENUATION IMAGING AT MT. VESUVIUS
PHYSICS OF THE EARTH AND PLANETARY INTERIORS

Dear Editor,
First of all we want to thank both reviewers for the suggestions, which were
really useful to improve the paper quality, and in particular the graphical
representation of the results obtained.
We took into account all the suggestions made by both reviewers. We also answer
to the questions raised, to better clarify how we corrected the paper. We
specify all the points, starting from those raised by Referee 2.
One of the main point to be addressed is the improving of all the synthetic
tests. We hence decided to a) include in the article a synthetic anomaly test;
b) to explicitly show the checkerboard test; c) to mark the high resolution
volume enlightening the test results inside this zone.
Another important point was the discussion of the results, too short and concise
in the first version. We re-wrote completely all this stuff, trying to
explicitly illustrate in detail our interpretation.
The other major comment regards the effective resolution of our method (300 m).
We follow an empirical rule, that the wavelength must be lower than a half of
the minimum cell size. Moreover, we consider for the interpretation only those
cell crossed by a number of rays defined by the empirical equation (14). The
question arisen by rev. 3 about the formal correctness of formula (14) is right.
With the decreasing of the cell size, the minimum number of rays passing through
the cell also decreases. Anyway, this number is never lower than 4. We have
empirically observed that this number ensures stable results. So, we are
confident that, even with a decreasing resolution, the results do not represent
ghost images.

All the other minor points have been fully addressed, as reported in the
following list, in which in capital letters there is copied the reviewer
comment, and in lower case our reply.

Reviewer 2.
 1) THIS PAPER PRESENTS ATTENUATION TOMOGRAPHY RESULTS BASED ON A
 MODIFIED CODA NORMALISATION APPROACH. THIS QUITE NEW APPROACH HAS
 BEEN DEVELOPED AND PUBLISHED PREVIOUSLY BY DEL PEZZO ET AL. (2006)
 AND APPLIED TO A QUITE SIMILAR DATA SET AS THE ONE PRESENTED HERE.

 This is not true, as we clearly indicate in the text. We used a number of
waveforms more than doubled respect to the previous.

 2) AT THE CURRENT STATE OF THE PRESENTATION OF THE PAPER I AM VERY
 SUSPICIOUS IF THIS STUDY IS REALLY FURTHERING OUR KNOWLEDGE IN ANY
 WAY OR IF IT IS JUST A REPETITION OF THE RESULTS ALREADY PUBLISHED
 BY DEL PEZZO ET AL. (2006).
First, we use a multi-scale approach. Second, respect to the first version we
have a new image of Qp. Third, we use much more data and a more precise ray-
tracing procedure. This improvement helps in new and more detailed
interpretation.

3) (ALTHOUGH APPENDIX 3 IS A LITTLE BIT TEDIOUS AND COULD BE
 CONSIDERABLE SHORTENED),
For us it is very hard to shorten this part without loosing in clearness. We
thus prefer not to shorten this appendix to avoid any misunderstanding
in the application of the procedure.

4) MY MAIN CONCERN IS NOT RELATED TO THE THEORY, WHICH IS WELL
 PRESENTED BUT IS BASED ON THE FACT HOW MUCH MORE DETAIL IS REALLY RESOLVED WITH
THIS HIGHER RESOLUTION TECHNIQUE. THE REASONING FOR THIS IS A AS FOLLOWS:

(I) CHAPTER 6.3 AND FIG. 3 PRESENT A CHECKERBOARD RESOLUTION TEST,
 WHICH SHOULD CLEARLY EMPHASIS THE RESOLUTION CAPABILITY OF THIS NEW
 DATA SET TOGETHER WITH THE NEW HRR APPROACH.
Checkerboard resolution test presented in fig. 3 of the first version was not
able to illustrate to readers the improvement that the multiple resolution
technique produces in our results. So, in the new version several numerical
tests were performed to show both the increased resolution in the whole area and
the capability of the used method of reproducing the main anomalies inferred by
the inversion. In particular, the checkerboard resolution test presented in the
first version has been better discussed and illustrated, showing both SN and WE
profiles together with horizontal slices at the depths where the most important
results have been found. We also marked the area of improved resolution (300
meters) [the effective HRR].

5) HOWEVER, FIGURE 3   SUGGESTS, THAT THERE SEEMS TO BE NO HIGH RESOLUTION FOR
REGIONS   BELOW 3000M, WHERE ONE OF THE ANOMALIES HIGHLIGHTED AND DISCUSSED
LATER ON IS LOCATED (ANOMALY 2). THE OTHER ANOMALY (NUMBER 1)DISCUSSED IN THE
PAPER, IS ALSO LOCATED BETWEEN 4519000 AND 4521000, A REGION WHERE ONLY A FEW
CELLS ARE WELL RESOLVED BY THE HRR AS STATED IN THE CHECKERBOARD TEST. SO ALL
THE RESULTS DISCUSSED IN THE PAPER ARE COMING FROM THE LRR AND THOSE FINDINGS
HAVE BEEN PRESENTED BEFORE. ADDITIONALLY, THE RESOLUTION TEST IS ALSO PLOTTED
FROM NORTH TO SOUTH WHERE AS ALL THE TOMOGRAPHY IMAGES ARE SHOWN FROM SOUTH TO
NORTH, WHICH DEFINITELY HAS TO BE CORRECTED.
The synthetic anomaly test done in the revised version effectively reveals that
under 3500 meters there is no high resolution; however, part of the anomaly 2
(as was marked in the first draft) is still present inside the HRR (the one
above 3500 meters) and the other part can be reconstructed at a resolution of
900 meters. The deep part of this anomaly (at a resolution of 900m) was not
detected in our previous paper (Del Pezzo et al. 2006). The improved image has
been obtained in the present paper thanks to the strongly improved data set and
quality. The present data set is more than doubled respect to the previous
dataset, and span a wider depth interval respect to the previous one. The area
where we find anomaly 1 (as marked in the first draft) is in the HRR, even if in
Fig 3 there was a misleading perspective; in the revised version we add new
images for the resolution test and do a synthetic anomaly test to show the
capacity of effectively reconstructing this anomaly at a 300m scale.

6) IT CERTAINLY DOES NOT HELP THAT THE PRESENTATION OF RESULTS IN
 THE TEXT IS RATHER SCRAPPY WITH SOMETIMES JUST A SENTENCE (E.G. A))
 AND NO ADDITIONAL EXPLANATION AT ALL. THIS LOOKS LIKE TO ME THAT THE
 WRITING UP PHASE OF THIS PAPER HAS BEEN RUSHED QUITE A BIT AND WAS
 NOT HANDLED WITH ENOUGH CARE SEEN ESPECIALLY IN THE RESULTS AND
 DISCUSSION SECTION. SINCE NO NEW METHOD HAS BEEN DEVELOPED THESE TWO
 SECTIONS SHOULD BE THE STRENGTH OF THE PAPER AND IT SEEMS THAT THE
 AUTHORS HAVE NOT PUT ENOUGH ATTENTION TOWARDS THESE SECTIONS. THE
 DISCUSSION AND CONCLUSION SECTION IS ALSO JUST AN ITERATION OF WHAT
 HAS BEEN FOUND BEFORE AND DOES NOT PUT ANY EMPHASIS IN CORRELATING
 AND DISCUSSING THEPOSSIBLE NEW FINDINGS WITH EXISTING STUDIES.
We agree with this criticism. To help the reader we re-wrote all the section,
with much more details.

 THERE ARE ALSO A LOT OF OTHER INCONSISTENCIES IN THE PAPER AND SOME
 OF THEM ARE LISTED BELOW:
 7) DEPTHS GIVEN IN THE PAPER ARE NOT ALWAYS IN RESPECT TO A COMMON
 DATUM (SEA LEVE, VOLCANO TOP,.) WHICH MAKES IT HARD FOR THE READER
 TO FOLLOW.
Done. Depths from the sea level.
 8) QT HAS NEVER BEEN INTRODUCED.
Introduced.

 9) AVERAGING BRACKETS < SHOULD BE INTRODUCED.

This was a misprint. We cut off the brackets.
 10) THE SYMBOL <GAMMA IS USED FOR THE FREQUENCY DEPENDENCE OF THE
 SOURCE SPECTRUM AS WELL AS FOR THE FREQUENCY DEPENDENCE OF Q.
Right. The frequency dependence of Q was changed in alpha.
 11) EQUATION 10 DOES NOT CONTAIN AN EXPONENTIAL TERM
This was an error. We changed the entire sentence.

 12) THE USED FREQUENCY RANGE HAS TO BE CLARIFIED MORE PRECISELY
 ESPECIALLY DIFFERENCES BETWEEN THE CN AND THE SD APPROACH.
This is done in section 4.5
 13) THE CN METHOD FOR 18HZ USES FREQUENCIES UP TO 23.6, WHICH IS
 RATHER CLOSE TO THE LOWPASS FILTER OF 25HZ, PRESUMABLY DUE TO DATA
 TRANSMISSION. HAVE CHECKS BEEN CARRIED OUT TO VERIFY THAT THIS
 LOWPASS FILTER DOES NOT INFLUENCE THE RESULTS IN THIS FREQUENCY BAND?
   The response is flat up to 25 Hz while we cut at 23.6.
 14) THE BOX SIZE OF 300M IS IN THE SAME ORDER AS THE WAVELENGTH FOR
 BOTH P- AND S- WAVE. IS THE HIGH FREQUENCY APPROXIMATION IMPLICITLY
 ASSUMED IN THE TOMOGRAPHY APPROACH STILL FULFILLED IN THIS CASE?
We already answered to this question in the introduction of this letter.

 REVIEWER #3: I HAVE CAREFULLY READ THIS PAPER AND I THINK THE
 AUTHORS SHOW A NEW AND USEFUL METHOD TO EXPLORE SMALL SCALE
 ATTENUATION STRUCTURES.
 NEXT, I GIVE MY COMMENTS WHICH COULD HELP THE AUTHORS TO CARRY OUT A
 MORE DETAILED DESCRIPTION
 COMMENTS:

1) I SUGGEST THE AUTHORS SHOULD GIVE A BETTER DESCRIPTION OF THE METHOD
 AND ITS METHODOLOGY. THE MAIN AIM OF THIS STUDY COULD BE EASILY
 ILLUSTRATED WIHT ATTENUATION TOMOGRAPHIC IMAGES IN EACH STEP, THAT
 IS, FOR EACH CELL SIZE. MOREOVER, SINCE THIS IS A TOMOGRAPHIC
 STUDY, SYNTHETIC TESTS MORE REALISTIC SHOULD BE SHOWED IN THIS STUDY
 FOR EXAMPLE, SYNTHETIC ANOMALY TESTS (E.G. SCHURR ET AL., 2003; BAI
 AND GREENHALGH, 2005; EBERHART-PHILLIPS ET AL., 2005) AND RESTORING
 RESOLUTION TESTS (E.G. ZHAO ET AL., 1992). THESE TESTS ARE USEFUL TO
 CHECK STRUCTURES WITH DIFFERENT SHAPE AND SIZE. SOME INFORMATION
 SHOULD BE ADDED/MODIFIED TO UNDERSTAND CORRECTLY THE RESULTS: RAY-
 PATH PLOTS OR MARK THE REGIONS WITH THE BEST RESOLUTION OR DENSITY
 OF RAYS (E.G. RIETBROCK, 2001; DE GORI ET AL., 2005), PLOT THE GRID
 USED OVERIMPOSED IN THE FINAL MODEL PLOTS (E.G. RIETBROCK 2001,
 REYNERS ET AL., 2006),
 SYNTHETIC TESTS ARE USED TO KNOW HOW THE REAL STRUCTURE IS
 RECONSTRUCTED WITH THE EVENT-STATION DISTRIBUTION AND THE PARAMETER
 VALUES USED IN THE INVERSION OF THE REAL DATA (E.G. SCHURR ET AL.,
 2003; RIETBROCK, 2001, ...).
This comment greatly helped us to better address the part of the paper dealing
with synthetic tests and with the marking of HRR. We start giving a better
representation of the resolution test done in the first version of this paper;
as the main interest of our paper is to constrain the zone characterized by
anomalous attenuation, we also performed a synthetic anomaly test, following
Shurr (2003).
We gave an improved representation of our results inspired by the papers
indicated by Rev. 3 , which resulted greatly helpful.

2)IN THIS STUDY, THE NR FACTOR IS DIFFERENT IN THE INVERSION OF THE REAL DATA
(NR5) AND THE CHECKERBOARD SYNTHETIC DATA (NR9). WHY THE SYNTHETIC AND REAL
DATA ARE INVERTED WITH A DIFFERENT VALUE OF NR??. ON THE OTHER HAND, THE
AUTHORS DECLARE THAT NR5 CAN ENSURE THAT EACH BLOCK IS HOMOGENEOUSLY SAMPLED. I
HAVE SOME DOUBTS. I THINK THAT THE EXPRESSION (14) WORKS WELL FOR CELL SIZE OF
1800 AND 900 M, BUT NOT   WHEN THE CELL SIZE IS CLOSE TO WAVELENGTH, AS IN THE
CASE OF A CELL   SIZE OF 300 M.

The factor of nR=9 was a typographical error: all our results come from
the formula (14). Formula (14) on the other hand is sounded only on an empirical
base: at 12 and 18 Hz centre frequency, the wavelengths are always below the
minimum cell size. The question arisen by rev. 3 about the formal correctness of
using formula (14) is right. With the decreasing of the cell size the minimum
number of rays passing through the cell also decreases. Anyway, this number is
never lower than 4. We have empirically observed that this number ensures stable
results. So we are confident that, even with a decreasing resolution, the
results at 18 Hz do not represent ghost images.

3) A MORE DETAILED DESCRIPTION OF THE CHECKERBOARD TEST IS ALSO REQUIRED. SOME
QUESTIONS SHOULD HAVE TO BE EXPLAINED:
   - THE GREY-SCALE IS UNCLEAR. WHAT DOES IT REPRESENT??, QT-1 OR
 <DELTAQT-1??
   - WHICH BLOCKS OF 1800 METERS AND 900 METERS SIDE HAVE BEEN USED
 FOR THE INVERSION WITH THE CHECKERBOARD TEST??
   - WHAT IS THE LOCATION OF THE DIVIDED BLOCKS?
 IF FIGURES 4, 5, 6, 7 AND 8 SHOW THE S-N AXIS, WHY DOES THE FIGURE 3
 SHOW THE S-N AXIS WITH DIFFERENT ORIENTATION??
 IT WOULD BE MORE CONVENIENT TO PLOT ALL FIGURES WITH THE SAME
 REFERENCE SYSTEM.
Ok, we corrected all this stuff making new plots.

4) IN THE TEXT IT IS INDICATED THAT THE INVERSION FOR 18 HZ CONSIDER AN
 INITIAL VALUE OF QT-1=0.019±0.003. COULD THE AUTHORS INDICATE WHICH
 INITIAL QT-1 VALUE IS USED IN THE REAL DATA INVERSION FOR THE
 FREQUENCY CENTRED AT 12 HZ??

We added in the text the requested information.

5) IT IS NOT CLEAR IN THE STUDY HOW THE ROBUSTNESS TEST HAS BEEN
 APPLIED. IT HAS BEEN APPLIED TO ALL BLOCKS, OR ONLY TO SOME BLOCKS.
 IT WOULD BE EASIER TO UNDERSTAND THE RESULTS OF THE ROBUSTNESS TEST
 IF THE RESULTS WERE PLOTTED AS IN LEES AND CROSSON (1989).

We corrected the text.

6) SINCE QCODA DEPENDS ON THE LAPSE TIME, IT WOULD BE CONVENIENT TO
 CHECK THE RESULTS OF QS-1 WITH OTHER LENGTHS OF THE CODA TIME WINDOW.
Unfortunately, this is practically impossible due to the noise level which is
severely high in the area under study, as widely discussed in Del Pezzo et al.
2006.

7) IN THE SECTION 7 AND 8 THE AUTHORS DECLARE " ...; THE CN AND SD
 METHODS FURNISH COMPARABLE IMAGES. ...", AND "... YIELDING
 PRACTICALLY THE SAME RESULTS.". HOWEVER THEY DO NOT INDICATE THE
 DIFFERENCES BETWEEN THESE IMAGES IN THE CENTRAL PART OF THE VOLUME,
 JUST BENEATH THE CRATERS BETWEEN -2000 AND -4000 METERS. COULD THE
 AUTHORS EXPLAIN WHY THE ATTENUATION TOMOGRAPHIC IMAGES GENERATED
 RESPECTIVELY BY THE CN AND SD METHODS ARE DIFFERENT IN THIS PART???.
 THE AUTHORS SHOULD EXPLAIN IF THESE DIFFERENCES DEPEND ON SOME
 FACTORS: SITE EFFECTS, SOURCE LOCATION, RAY COVERAGE, ... OR BY THE
 CONTRARY REMAIN UNCHANGED

The problem arisen by rev. 3 has been addressed in the following way. In the
first version of this paper we represented absolute estimates (Q-1) using the
same colour scale for the CN and SD. The estimates done with CN were defined in

the first version as the sum of the inverse Quality factor (averaged in the space) and its spatial variations (cell by cell). Using SD instead, we inverted for the variations of Q-inverse cell by cell, and represented these values summed to the average inverse Q obtained with CN. In the new representation reported in the revised paper, we avoid any bias and represent the variations respect to the mean, independently calculated for each method, taking as unique constraint that Q-1 must be positive. In this way it clearly appears that the two representations are practically equivalent. The small differences are however discussed in the new version of the paper.

8) IN THE PARAGRAPH OF THE SECTION 8 "DISCUSSION AND CONCLUSIONS" BEGINNING "THE HIGH CONTRAST IN BOTH S-WAVE VELOCITY, AND QS-1 ...", IT IS DISCUSSED THE VALUES OF VS AND QS-1 OF THE CIRCLE 2. HOWEVER, WHERE THE TEXT SAYS "THE OBSERVED STRONG CONTRAST MAY BE GENERATED BY A HIGHLY ... OVERIMPOSED (POINT "E" OF RESULTS; SEE ALSO DEL PEZZO ET AL. (2006)]" IT IS NOT CLEARLY RELATED TO "CIRCLE 2". I SUGGEST THAT SOME REORGANIZATION OF THIS PARAGRAPH IS NECESSARY.

Ok, done. We rewrote all the section.

9) IN ORDER TO BETTER UNDERSTAND THE FIGURES 4, 5, 6 AND 7, THE COLOR SCALE OF QS-1 SHOULD BE MODIFIED AND EXPLAINED TO SHOW THE REPRESENTATIVE QS-1 VALUES. I CAN NOT COMPARE QUANTITATIVELY THE REGIONS WITH COLOR BLUE, CYAN AND GREEN. ON THE OTHER HAND THE Q-1 SCALE VARIES IN THE RANGE BETWEEN 10-6 AND 0.05, BUT WHAT IS THE MINIMUM OF Q-1 IN THE VOLUME UNDER STUDY??

We decided to overcome the problem changing the colour scale.

10) FIGURES 4, 5, 6 AND 7. FOR A MAJOR UNDERSTANDING OF THE RESULTS, I ADVISE THE AUTHORS MARK IN THE FIGURE 4, 5, 6 AND 7 THE REGIONS WITH GOOD RAY COVERAGE OR THOSE WHERE THE CHECKERBOARD SYNTHETIC MODEL IS WELL RECOVERED. THE BLOCK SIZES SHOULD BE ALSO INDICATED

We did this in Fig. 3 and 4, marking the HRR with a white broken line.

11) FIGURE 8 IS NOT CLEAR. I SUGGEST THAT THE AUTHORS INCLUDE A PERSPECTIVE VIEW OF THE SHALLOW CRUST UNDER MT. VESUVIUS VOLCANO SHOWING THE LOW QS-1 ISOSURFACE AS IN FINLAYSON ET AL. (2003)

The set of new figures clearly show all the features avoiding any isosurface.

 MINOR
12) I THINK IT IS CONVENIENT TO MAKE A DISTINCTION BETWEEN RESOLUTION AND SPATIAL RESOLUTION TO AVOID AMBIGUITY BETWEEN CELL SIZE AND RESOLUTION MATRIX.
We always refer to the spatial resolution.

 GRAMMATICAL/TYPOGRAPHICAL:

 PAGE 2
 -- BAI ET AL. (2005) --- BAI AND GREENHALGH (2005)
Done
 PAGE 3
 -- IS MORE IMPORTANT THAN INTRINSIC ATTENUATION (DEL PEZZO ET AL., 2006) ...
 SPECIFY WHICH ARTICLE OF DEL PEZZO ET AL. (2006) YOU HAVE CITED

Done

-- A RESOLUTION OF 900 METERS IN A PREVIOUS STUDY OF THE SAME AREA, CARRIED OUT USING A SUBSET OF THE PRESENT DATA SET (DEL PEZZO ET AL., 2006). ...
SPECIFY WHICH ARTICLE OF DEL PEZZO ET AL. (2006) YOU HAVE CITED
Done
 PAGE 6
 AFTER THE EXPRESSION (2), "WHERE DCK REPRESENTS THE LOG-SPECTRAL RATIO BETWEEN S AND CODA PRE-MULTIPLED FOR ..."
 I THINK THAT IT IS CLEARER SAID " WHERE DCK REPRESENTS THE LOG OF ENERGY SPECTRAL RATIO ..."
Done
 PAGE 10
 -- BAI ET AL. (2005) --- BAI AND GREENHALGH (2005)

 -- " ... 900 METERS BLOCK IN THE PREVIOUS STEP.. WE DIVIDE.." --
 " ... 900 METERS BLOCK IN THE PREVIOUS STEP. WE DIVIDE.."
Done
 PAGE 13
 "..., CLEARLY CORRESPONDS WITH THE LOWEST QS-1 VALUES ..." -- "..., CLEARLY CORRESPONDS WITH THE LOWEST QP-1 VALUES ..."
 IF IT IS QS-1, IT WILL BE CHANGED THE REFERENCE TO THE FIGURE
 (FIGURE 4 PANEL B AND C)
Done
 PAGE 15

 -- " VOLCANIC ROCKS OVERIMPOSED (POINT "E" OF RESULTS; SEE DEL PEZZO ET AL. (2006)". SPECIFY WHICH ARTICLE OF DEL PEZZO ET AL. (2006) YOU HAVE CITED
Done
 IN THE EXPRESION (16) THERE IS A TYPOGRAPHIC ERROR:
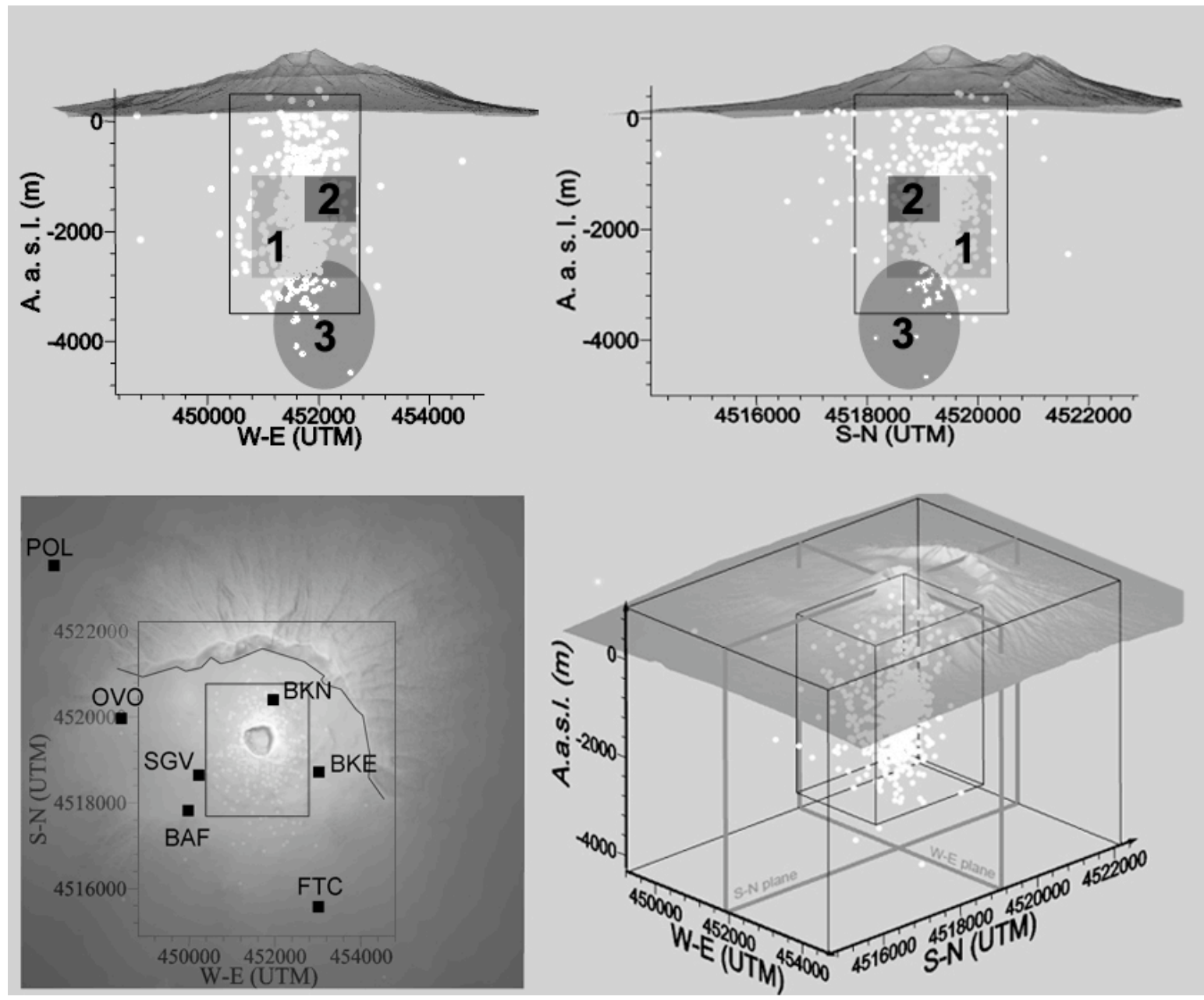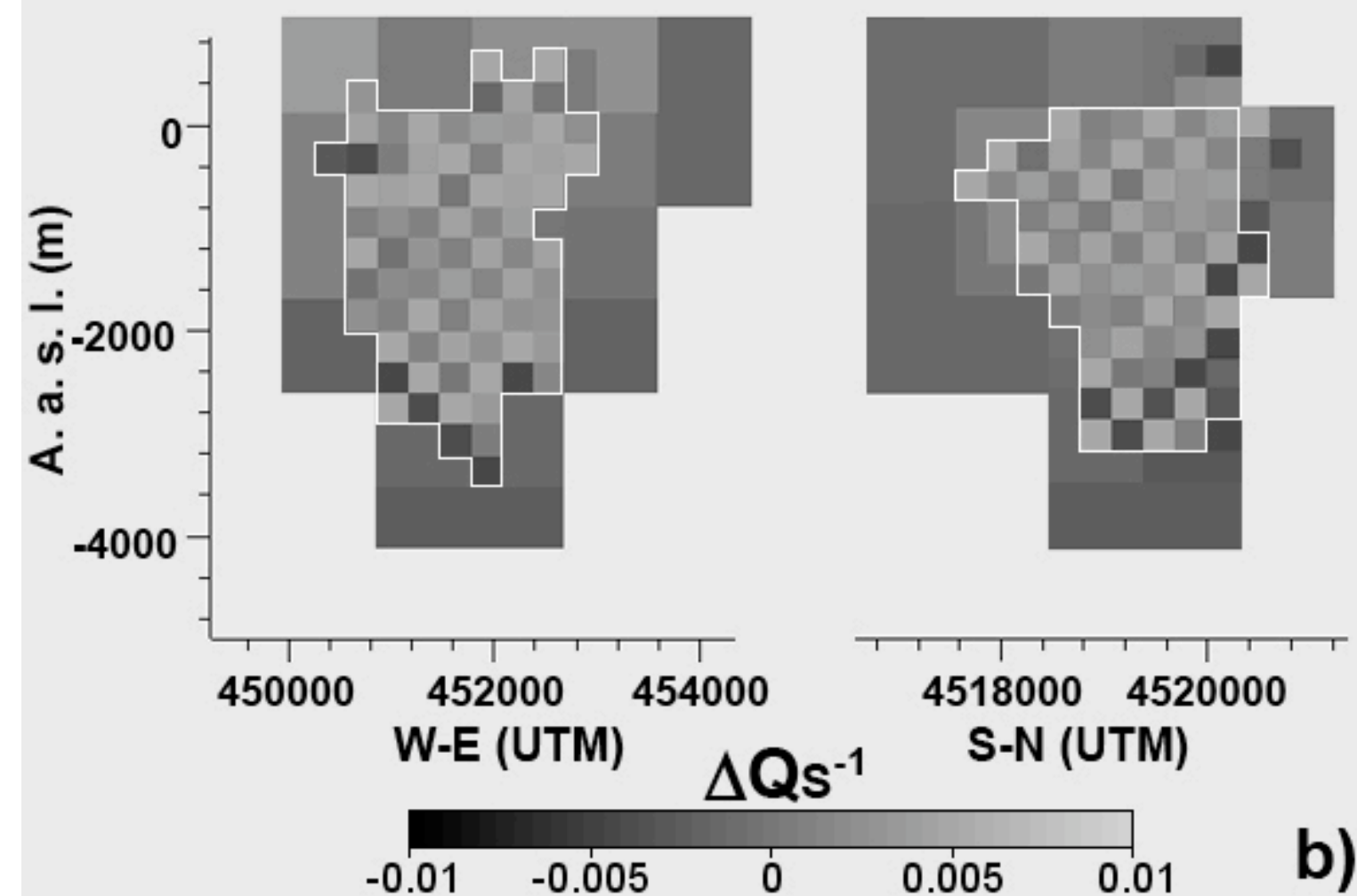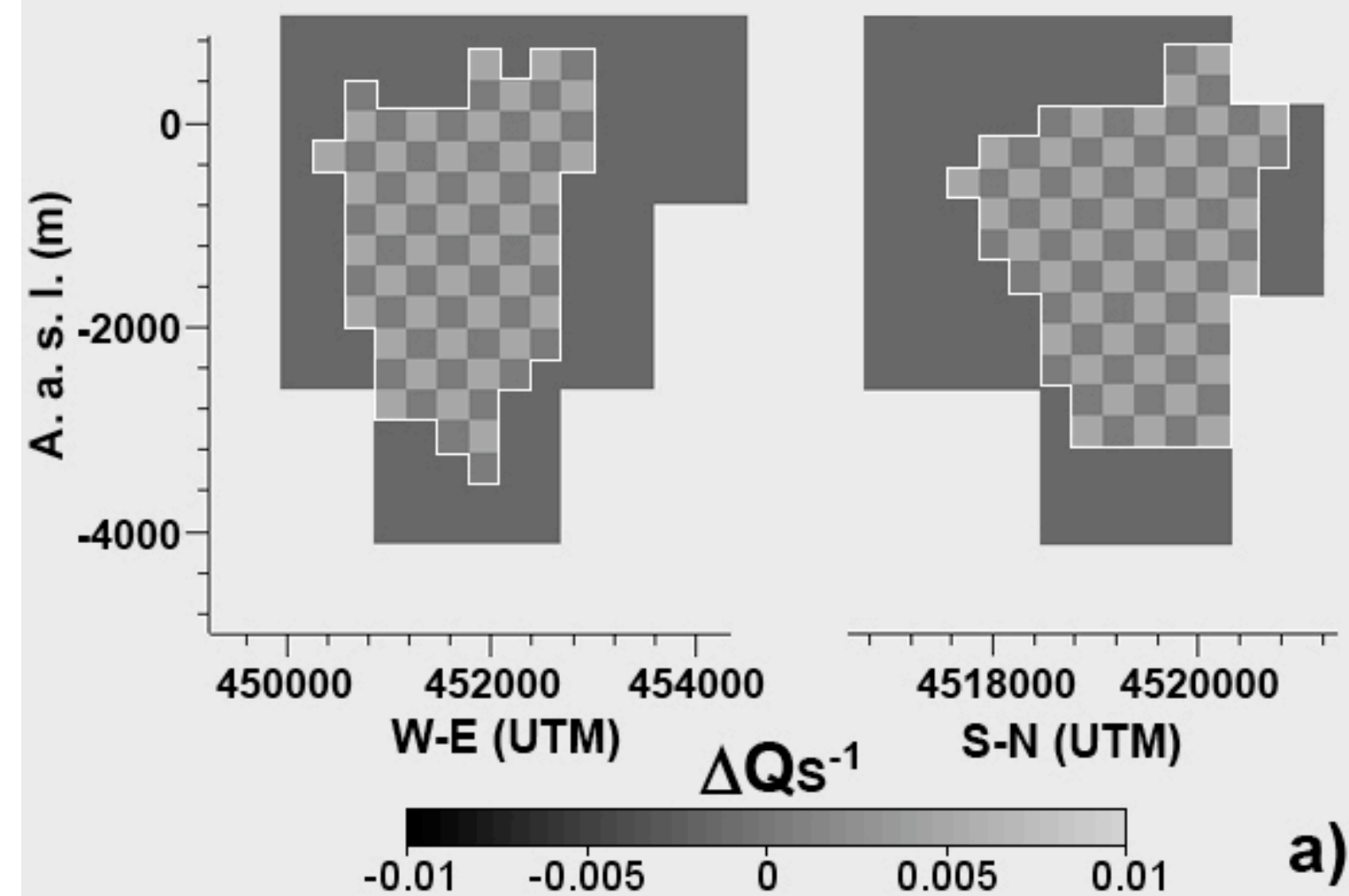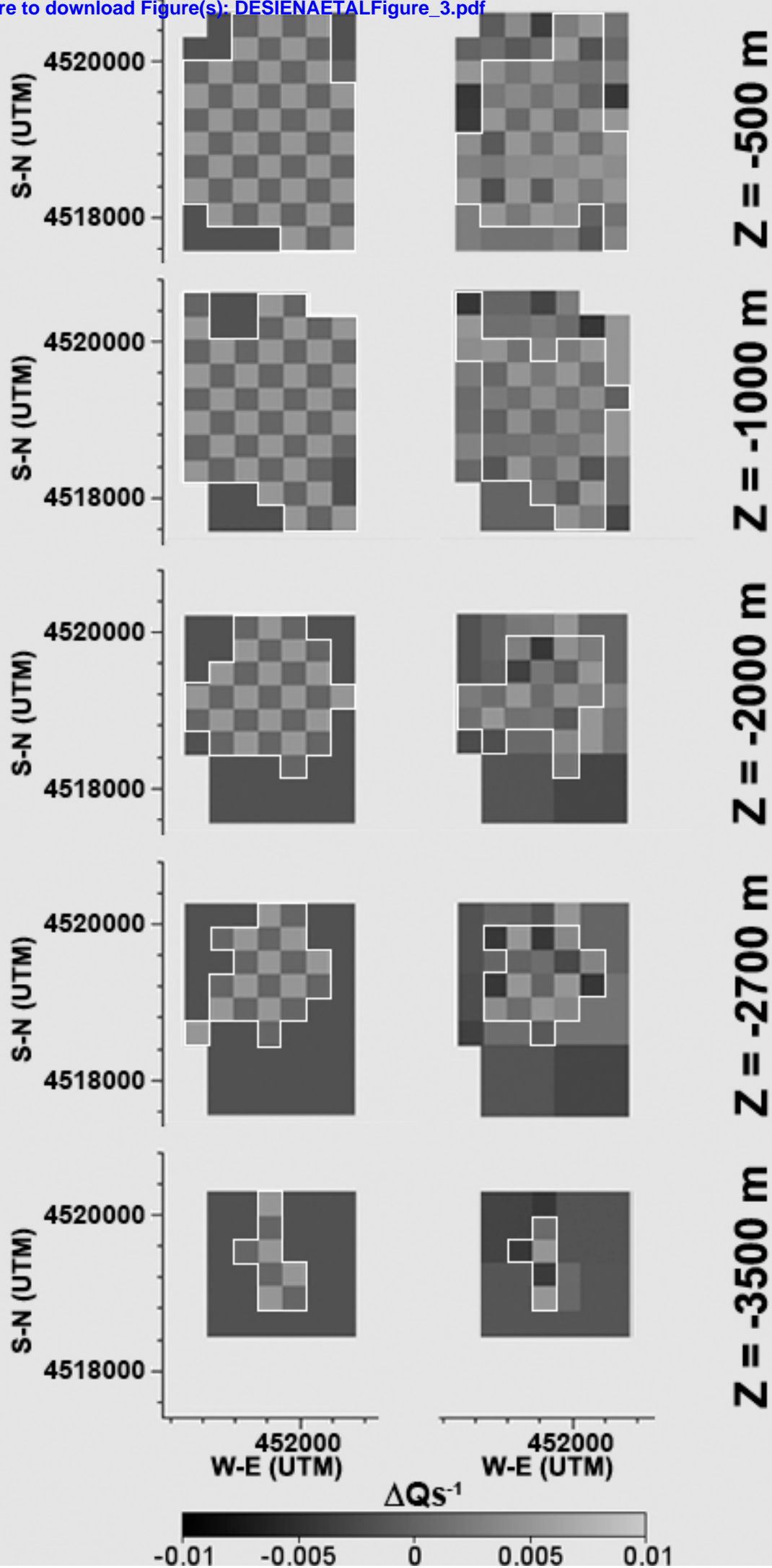 IT IS WRITTEN EIJ(F,R)=...1/RIJ, INSTEAD EIJ(F,R)=...1/RIJ2
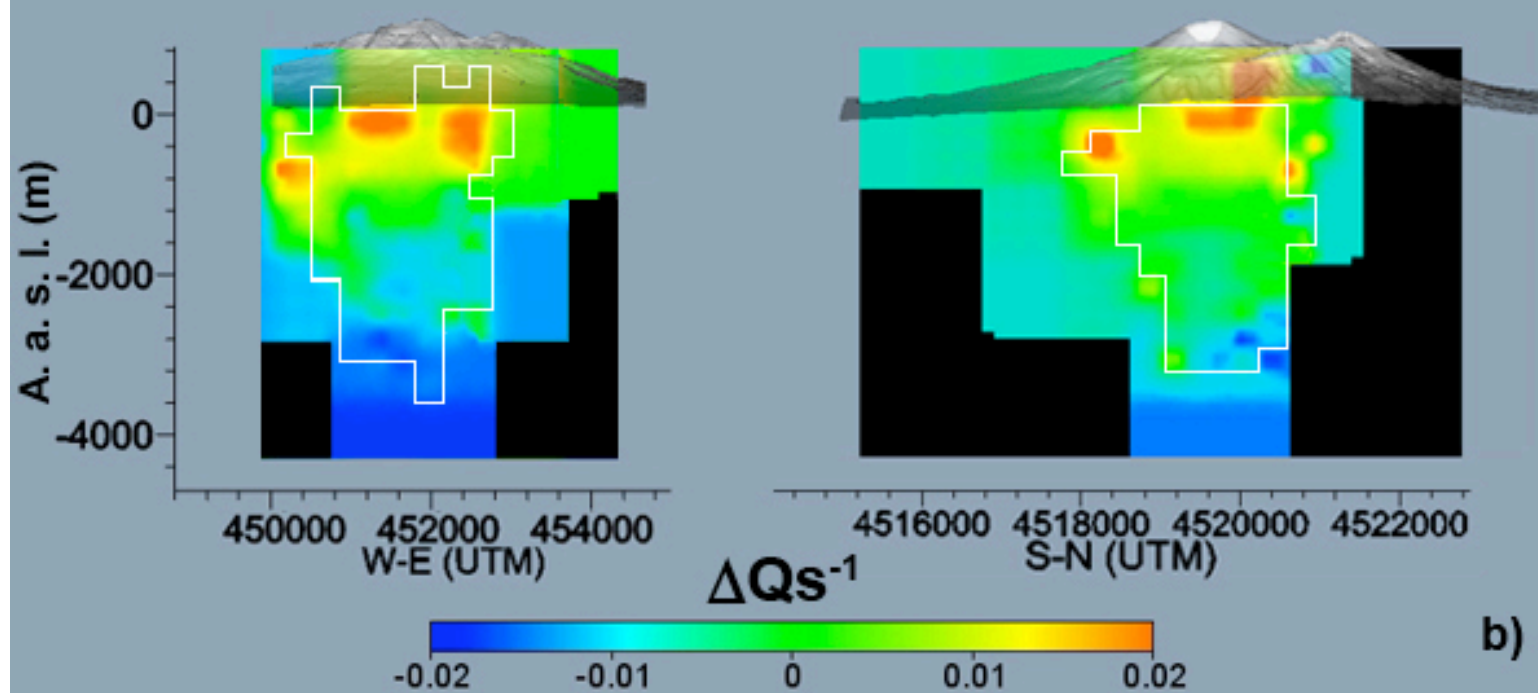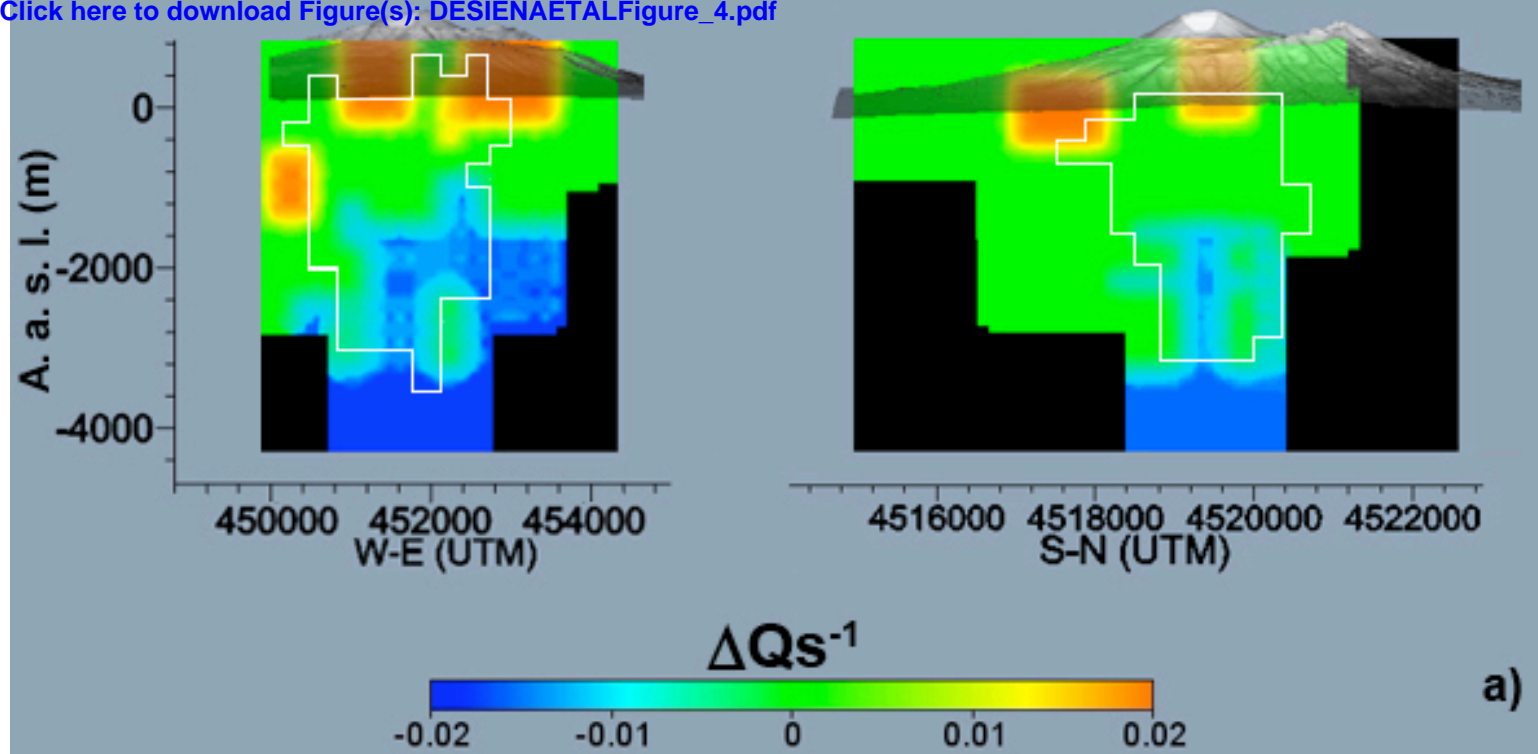Done
 PAGE 21
 REFERENCES
 BAI, C., AND GREENHALGH, S., 2006 .... --- BAI, C., AND GREENHALGH, S., 2005
Done.

ΔQs^{-1}

a)

ΔQs^{-1}

-0.01   -0.006   0   0.006   0.01

b)

ΔQs^{-1}

-0.02   -0.01   0   0.01   0.02
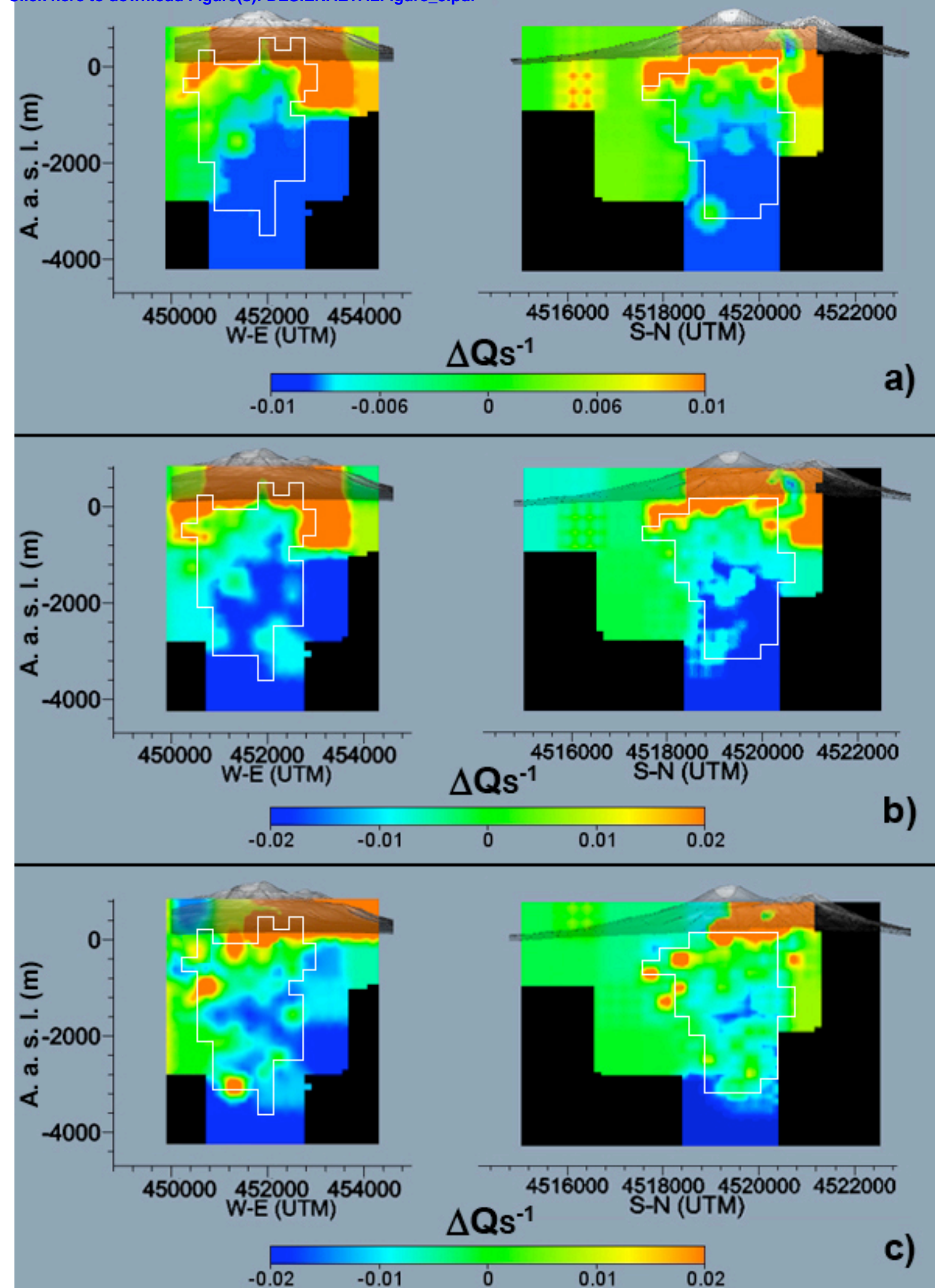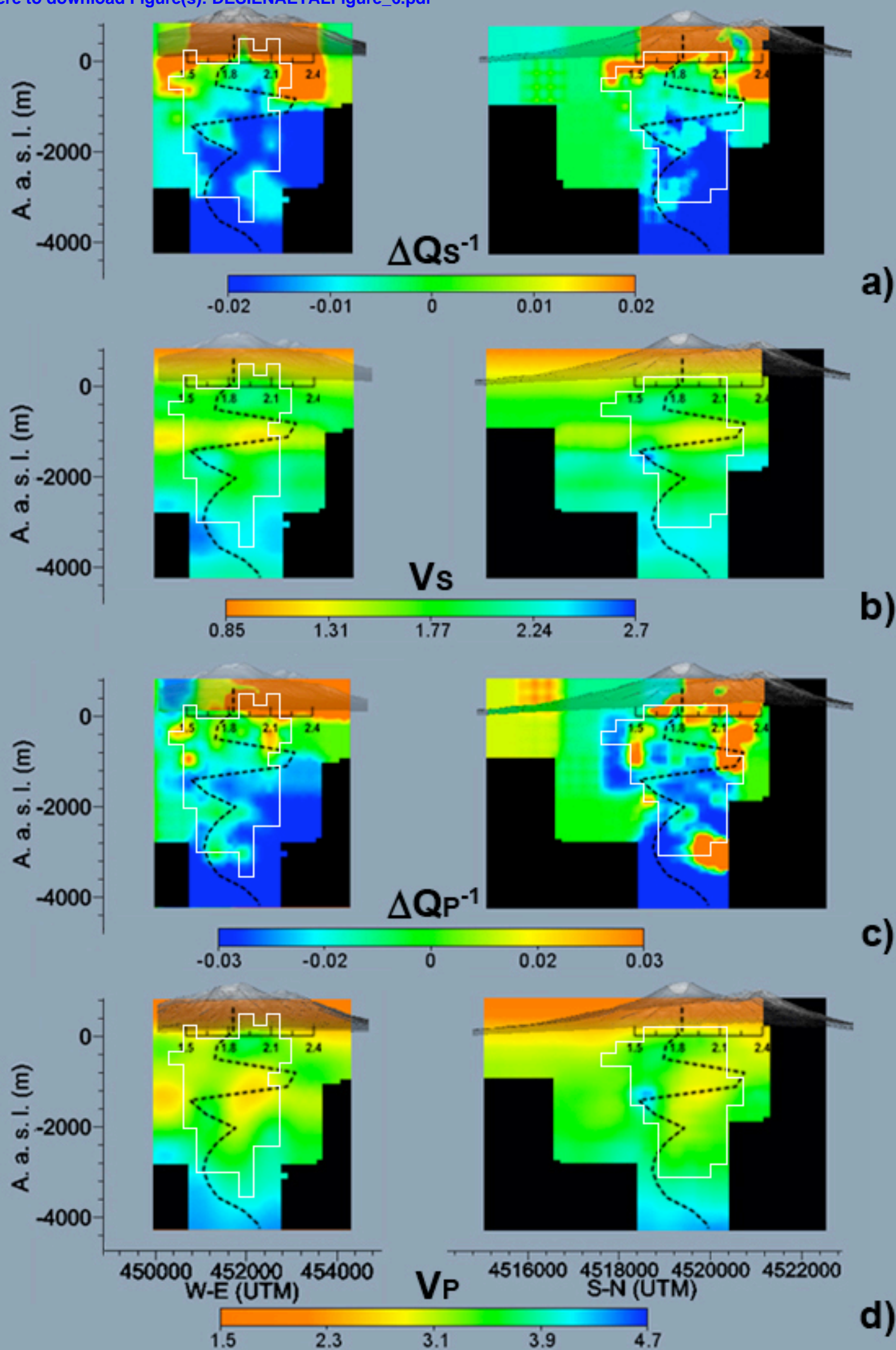
c)

ΔQs^{-1}
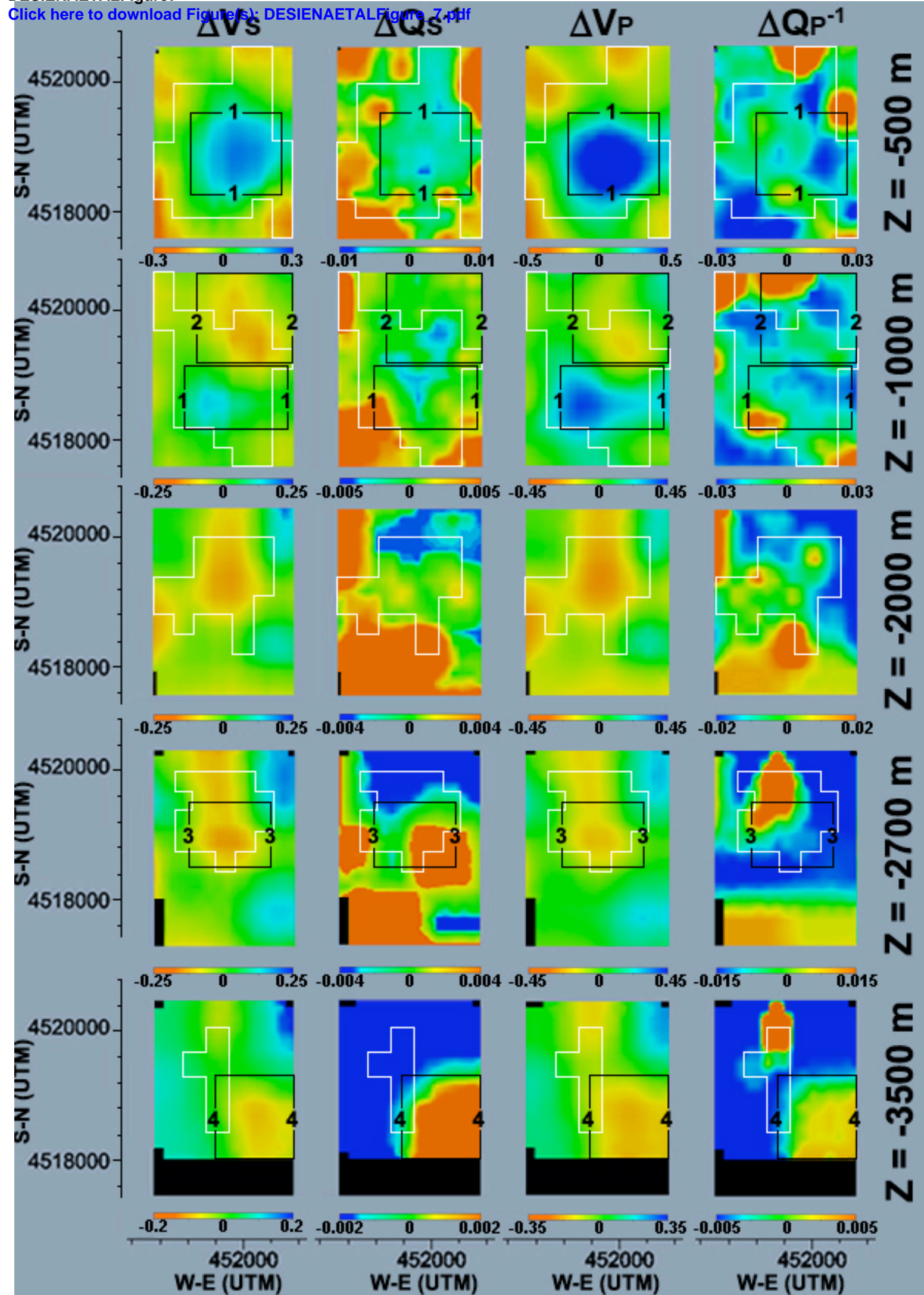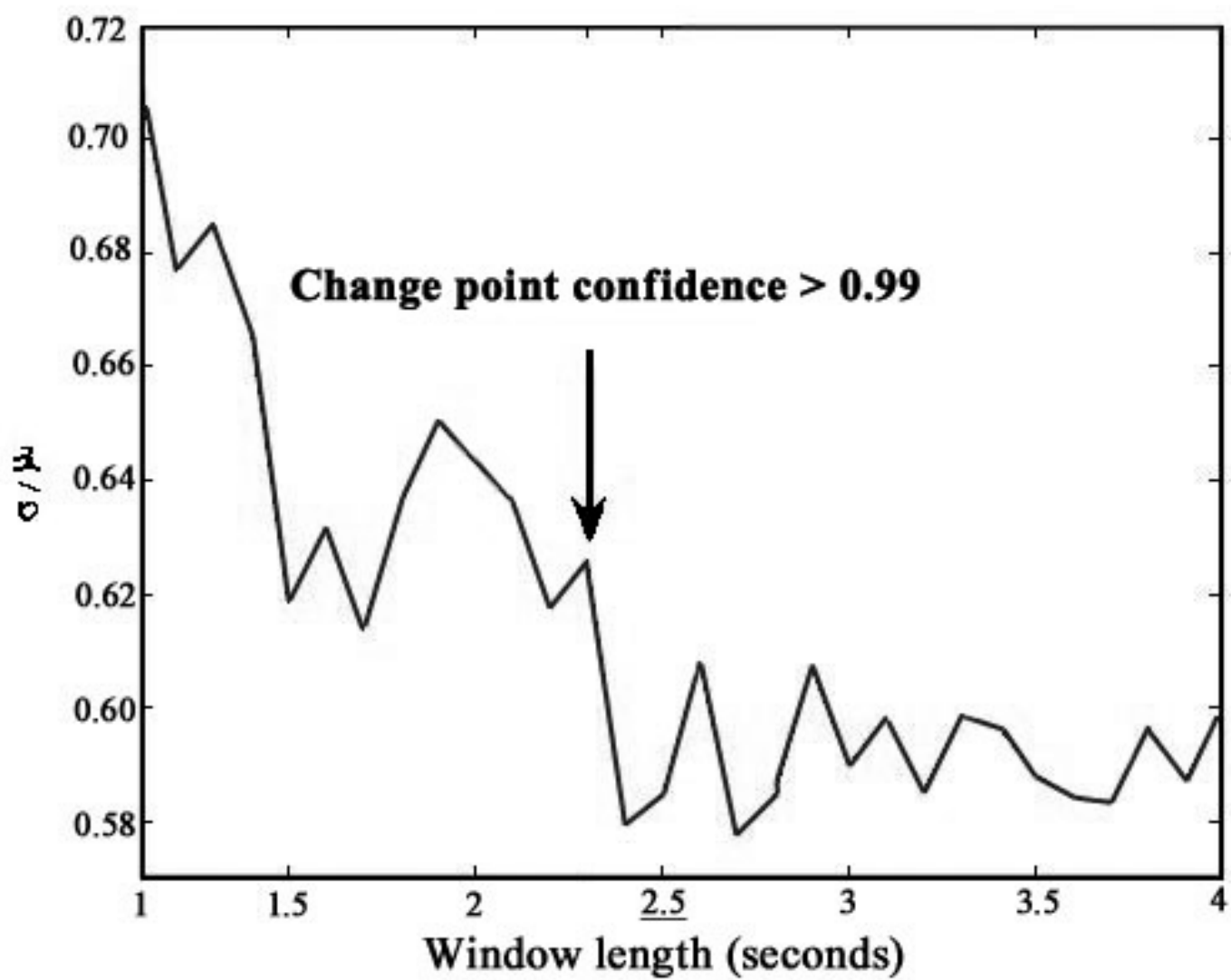
-0.02   -0.01   0   0.01   0.02

Multiple resolution seismic attenuation imaging at Mt. Vesuvius

Luca De Siena[1] *Edoardo Del Pezzo[1] Francesca Bianco[1]
Anna Tramelli[1]

[1]*Istituto Nazionale di Geofisica e Vulcanologia , sezione di Napoli Osservatorio Vesuviano, Via Diocleziano, 328 - 80124 Napoli, Italia.*

∗ *fax: +39 081 6108323 ; email: delpezzo@ov.ingv.it*

Abstract

A three-dimensional S wave attenuation tomography of Mt. Vesuvius has been obtained with multiple measurements of coda-normalized S-wave spectra of local small magnitude earthquakes. We used 6609 waveforms, relative to 826 volcano-tectonic earthquakes, located close to the crater axis in a depth range between 1 and 4 km (below the sea level), recorded at seven 3-component digital seismic stations. We adopted a two-point ray-tracing; rays were traced in an high resolution 3-D velocity model. The spatial resolution achieved in the attenuation tomography is comparable with that of the velocity tomography (we resolve 300 m side cubic cells). We statistically tested that the results are almost independent from the radiation pattern. We also applied an improvement of the ordinary spectral-slope method to both P- and S-waves, assuming that the differences between the theoretical and the experimental high frequency spectral-slope are only due to the attenuation effects. We could check the coda-normalization method comparing the S attenuation image obtained with the two methods. The images were obtained with a multiple resolution approach. Results show the general coincidence of low attenuation with high velocity zones. The joint interpretation of velocity and attenuation images allows us to interpret the low attenuation zone intruding toward the surface until a depth of 500 meters below the sea level as related to the residual part of solidified magma from the last eruption. In the depth range between -700 and -2300 meters above sea level, the images are consistent with the presence of multiple acquifer layers. No evidence of magma patches greater than the minimum cell dimension (300m) has been found. A shallow P wave attenuation anomaly (beneath the southern flank of the volcano) is consitent with the presence of gas saturated rocks. The zone characterized by the maximum seismic energy release cohincides with a high attenuation and low velocity volume, interpreted as a cracked medium.

Key words: Attenuation tomography, Mt. Vesuvius, Coda normalization method, Spectral slope, Multi resolution inversion

Rev. 2 Point 1

Rev. 2 Point 2

Rev.2 Point 2

Added.
Rev. 2 Point 6
Rev 3 Point 8

1 Introduction.

The knowledge of the internal structure of the volcanoes represents a crucial task to properly constrain the physical models of eruption. Passive tomography is one of the easiest and cheapest way to achieve this goal and is consequently widely applied for the study of volcano structures at several depths (Chouet et al., 1996).

There are two main factors limiting the maximum resolution that can be obtained in passive methods: the ray coverage and the wavelength of the waveforms from which the observables are retrieved. The first factor is linked to the station density and the source space distribution. The second is directly associated with the kind of events that are used as input. For a local tomography on a volcano with a volume of the order of 10 km of linear dimensions, local VT earthquakes, with their associate wavelengths that ordinary span from some kilometers to hundreds of meters (Chouet, 2003) are a suitable input. Generally the smallest wavelength characterizes the minimum cell size, and this can be considered as the thumb rule for this constraint. Moreover, to reach this minimum cell size, one needs a suitable source space distribution (sources as much as possible uniformly distributed in the volume, and an as dense as possible network of receivers). In a configuration typical of an up-to-date seismic network, an order of resolution of 300 meters can be reached only in the volume cells with a sufficient ray coverage (Chouet et al., 1996). This leads to the solution of a mixed-determined problem, with an highly overdetermined system of equations correspondent to the cells with a redundant number of rays crossing through, and an equal- or lower-determined system for the other cells. A way to optimize the problem is to use an approach with a non uniform cell size, that maintains a sufficient over-determination in any cell, but reaches a good resolution only in the parts of the investigated volume characterized by the maximum ray coverage. This kind of approach is typically named as multi-step or multiple-resolution method [see Bai and Greenhalgh (2005), for an example of travel time multi-step tomography on a volcano]. `Rev 3 Minor`

The attenuation of elastic waves depends strongly on a number of factors affecting the lithology, the most important of which are probably the temperature and the presence of fractures and hydrothermal or magmatic fluids. Attenuation is quantified by the quality factor, Q, defined as the ratio between the energy lost by a wave cycle and the energy of the cycle itself; equivalently, attenuation can be defined through the attenuation coefficient $\alpha = \pi f r / v Q$ `Rev 2 Point 10` that accounts for the damping of the wave amplitude, A, as a function of distance, r and frequency, f. This factor may greatly vary for rocks with the same composition but different degree of fracturing and/or temperature. The response of the rocks to the propagation of longitudinal and shear waves is different; the independent determination of the quality factors for longitudinal

2

(Qp) and shear (Qs) waves, critical parameters for the characterization of the physical state of the rocks within a volcano, aims at discriminating between melt fluids and gases residing at shallow depths in the earth's crust. For this purpose, a comparative study of velocity and attenuation tomography can be critical (Hansen et al., 2004).

A phenomenon that intensely affects the wave propagation in volcanic areas is the scattering process, which tends to transfer the high-frequency energy of direct P and S waves into the coda of the seismograms (Sato and Fehler, 1998). Scattering is produced by the interaction of the wavefield with the small scale heterogeneities in the elastic parameters, as, for example, those associated with intense rock fracturing. The average attenuation caused by scattering, can be studied independently from the one caused by intrinsic attenuation, separating the two different types of losses (Bianco et al., 1999). Results on volcanoes show that, for frequencies higher than 10 Hz, scattering attenuation is more important than intrinsic attenuation (Del Pezzo et al., 2006 a). For a comprehensive summary of results from attenuation measurements by a range of methods, at varying frequency, on different scales and in different geological settings the reader is referred to Sato and Fehler (1998).

Rev 3 minor

Unfortunately, for the single path estimates (necessary for tomography) of the attenuation coefficient, the separation between the two kinds of contribution (scattering and intrinsic) is practically impossible. Consequently, in the attenuation tomography, the parameter obtained by the inversion is the total-Q or the correspondent attenuation coefficient.

This paper is aimed at giving an image of the shallow crust materials at Mt. Vesuvius volcanic area using shear wave attenuation tomography at high frequency (in the range between 10 and 20 Hz), solved with a multi-resolution method with a minimum cell (the greatest available resolution) of 300 meters. Observables (total-Q inverse for each single path) are obtained using the coda-normalization method (Aki, 1980), and checked with the ordinary spectral-slope method. Spectral slope is used also to estimate P-wave total Q-inverse. Attenuation images are eventually compared with high resolution passive velocity tomography [the same minimum cell size, Scarpa et al. (2002)]. The images obtained with this method are also compared with those obtained at a resolution of 900 meters in a previous study of the same area, carried out using a subset of the present data set (Del Pezzo et al., 2006 b). We will show that the low attenuation zone located under the crater is coincident with a high velocity volume, possibly associated with residual frozen magma from the last eruptions; and that a high attenuation volume at 1-2 km of depth is coincident with a low velocity zone. This is interpreted as the aquifer permeating the shallow structure of Mt. Vesuvius.

Rev 3 minor

2   Geological and seismological settings.

Mt. Vesuvius is a stratovolcano formed by an ancient caldera (Mt. Somma) and by a younger volcanic cone (Mt. Vesuvius). The volcanic activity is dated back to 300–500 ky (Santacroce, 1987) and characterized by both effusive and explosive regimes (Andronico et al., 1995). The volcanic complex is located in the Campania plain (southern Italy) at the intersection of two main fault systems oriented NNW–SSE and NE–SW (Bianco et al., 1997). The last eruption, in March 1944, was effusive (Berrino et al., 1993). It may have started a new obstructed conduct phase and hence a quiescent stage.

The seismic activity is actually the unique indicator of the internal dynamics [see e.g. De Natale et al. (1998)]. Seismicity studies are of extreme importance for the high risk volcanic area of Mt. Vesuvius. As an overall, the seismicity of Mt. Vesuvius is characterized by a mean rate of approximately 300 events per year. The largest earthquake in the area [reasonably since the last eruption -1944- see Del Pezzo et al. (2004)] occurred in 1999, and has been associated with regional and local stress fields (Bianco et al., 1997). The main features of the earthquake space and time distribution are described in the papers by Scarpa et al. (2002), hereafter cited as SCA02, and Del Pezzo et al. (2004). In the study of SCA02 the relocated seismicity appears to extend down to 5 km below the central crater, with most of the energy (up to local magnitude 3.6) clustered in a volume spanning 2 km in depth, positioned at the border between the limestone basement and the volcanic edifice. The hypocentral locations for the data used in the present article show the same pattern of the overall seismicity (Figure 1).

The earthquakes recorded at Mt. Vesuvius are mostly of volcano-tectonic type (VT), with fault-plane orientations, showing an highly non-regular spatial pattern. The spectral content of the P- and S-wave trains of the VT events is compatible with stress drops spanning a range between 1 and 100 bars (100 bars for the largest magnitude) and focal dimensions of the order of 100 m (Del Pezzo et al., 2004).

The velocity structure beneath Mt. Vesuvius, in the depth range from the Earth surface to 10 km, has been deduced by seismic tomography. Auger et al. (2001) suggest the presence of a melting zone at a depth of about 8 km, on the base of the TOMOVES experiment results (see the book by Capuano et al. (2003) and the numerous references therein). At smaller scale, between the topographical surface and 5 km of depth, SCA02 evidence a low velocity contrast between 1 and 2 km, possibly associated with the presence of aquifers. No shallow and small magma chambers are visible at the resolution scale reached by SCA02.

3 Data selection.

In the present work we utilized a total number of <mark>6609 waveforms, obtained from a selection of 826 earthquakes recorded from January 1996 to June 2000 at seven 3-component stations</mark> that are the analogical station OVO (66 dB dynamic range, three component) sampled at 100 s.p.s. and 6 digital, high dynamic (120 dB, gain ranging), 1 Hz , seismic stations sampled at 125 s.p.s. (Table I). Analog anti-aliasing filter with 25 Hz cut-off frequency operated on all the data logger prior to sampling. Data selection has been made on the base of the following pre-requisites: the best signal to noise ratio, the absence of spikes and other disturbances in the waveforms, a minimum coda duration (from origin time) of 15 s and the absence of secondary events in the early coda. In doing this selection we implicitly restricted the earthquake magnitude in the range from 1.6 to 3.0, because small aftershocks are often present in the coda of larger events. Location of the 826 earthquakes (Figure 1) was obtained using P-picking of all the available seismic stations constituting the monitoring network (www.ov.ingv.it) with a non linear procedure based on a grid-search algorithm (Lomax et al., 2001); ray-tracing was calculated using the $3D$ velocity model obtained by SCA02.

> Rev 2 point 1

4 Methods.

4.1 Ray tracing.

<mark>We used a Thurber-modified approach (Block, 1991)</mark> to trace the path of each ray in the 3-D velocity structure of Mt. Vesuvius obtained by SCA02. This is an extension of the approximate ray-bending method (Um and Thurber, 1987) that works well in velocity structures characterized by fairly sharp velocity variations, like that of Mt. Vesuvius. The only limitation is that the method does not compute reflected ray paths, that anyway are not taken into account in the present work. After dividing the whole structure to be investigated in three different grids (respectively with 1800, 900 and 300 m cubic cell size) we stored in a database the length of each ray, connecting each source to each receiver, and the length of the ray-segments crossing each cell. This database is necessary for the multiple-resolution inversion approach, as discussed later.

> Rev 2 point 1

4.2   Single-path attenuation with the coda-normalization (CN) method.

The CN method is widely used to retrieve attenuation parameters independently of the site and instrumental transfer function [Aki (1980); Sato and Fehler (1998)]. Del Pezzo et al. (2006 b) used this approach for the estimation of single path total Q-inverse to map the S-wave attenuation structure in Mt. Vesuvius area, using a subdivision of the investigation volume in cubic cell of 900 meters in a single-scale approach. Even though the method used to estimate the single path inverse total-Q has been already described and discussed in Del Pezzo et al. (2006 b), we report in Appendix 1 a synthesis for sake of completeness.

Our reference equation (see Appendix 1 and 2 for any detail) is:

$$\frac{E_{ij}(f,r)}{E^C(f,t)}r_{ij}^2 = \frac{1}{P(f,t_c)}\exp\left[-2\pi f\int\limits_{rij}\frac{dl}{v(l)Q_T^{ij}(l)}\right] \tag{1}$$

Taking logs of both sides of eq. (1) and approximating the line integral with a sum, we can write

$$d_k^C = \frac{1}{2\pi f}\ln(\frac{1}{P(f,t_c)}) - \sum_{b=1}^{N\_cells} l_{kb}s_b Q_b^{-1} \tag{2}$$

Rev 2 point 9

where d_k^C represents the log of energy spectral ratio between S and coda pre-multiplied for the squared ray-length and divided for $2\pi f$. N_cells is the total number of blocks crossed by the ray , l_{kb} is the length of the k-th ray-segment intersecting the b-th block characterized by slowness s_b and inverse quality factor Q_b^{-1}. In this formulation we use the suffix k to indicate the k-th ray of the suite of rays connecting stations to sources. Eq. (2) can be rewritten separating Q_b^{-1} into an average Q_b^{-1}, $<Q_b^{-1}>$, that we assume to be equal to the average quality factor for the whole area (Q_T^{-1}), and an incremental δQ_b^{-1}.It results:

Rev 3 minor

Rev 2 point 8

$$\tilde{d}_k^C = \sum_{b=1}^{N\_cells} l_{kb}s_b\delta Q_b^{-1} \tag{3}$$

where:

$$\tilde{d}_k^C = \frac{1}{2\pi f}\ln(\frac{1}{P(f,t_c)}) - d_k^C - Q_T^{-1}\sum_{b=1}^{N\_cells} l_{kb}s_b \tag{4}$$

Eq. (3) represents a linear system of N_k equations in N_cells unknowns that can be inverted, as discussed in the next chapters.

6

4.3 The estimate of the observables with the CN method.

Prior to the application of the CN method we checked the temporal stability of the S-wave time window for the radiation pattern effect, as widely described in Appendix 2. Accordingly, we set the duration of the S-wave time window at 2.5 s starting from the S-wave arrival time. Coda signal time window starts at 8 s lapse time and ends at 12 s, since most of our data show a favorable signal-to-noise ratio (>3) for lapse time smaller than 12 s. A Discrete Fourier Transform (DFT) is applied to the signals after windowing (we used a cosine taper window with tapering at 10% both for S and coda) for both the horizontal components of the ground motion. We calculate the S spectral amplitude averaged in the frequency bands centered at the values of frequency, f_c,with bandwidths ($\pm \Delta f$) reported in Tab II, and finally log-averaged over the components; we thus obtain the ratio between the S-wave spectrum and the coda spectrum. The natural logarithm of this ratio estimates d_k^C of formula (4). The constant in eq. (2) has been already estimated by Del Pezzo et al. (2006 b) for the area under study.

4.4 The slope-decay (SD) method .

As a complementary approach, we adopted the so called slope decay method, which has been widely used to estimate the attenuation coefficient in many regions of the world [Nava et al. (1999), Giampiccolo et al. (2003), Gudmundsson et al. (2004)].

As well known, the amplitude spectral density for S and P waves for frequencies higher than the corner frequency can be expressed as the product of source, path and site effects as:

$$A_{ij}^{HF}(f,r) = S_i^A(f) I_j(f) T_j(f) G_{ij}(r) \exp(-\pi f \frac{t_{ij}(r)}{Q_T^{ij}(r)}) \qquad (5)$$

where $A^{HF}(f,r)$ is the high-frequency spectral amplitude of the P- or S-wave radiation emitted by the source i at total distance r measured along the source(i)-station (j) ray-path; f is the frequency; $S_i^A(f)$ is the amplitude spectrum at source; I_j is the instrument transfer function; T_j is the site transfer function and G is the geometrical spreading term; t_{ij} is the travel time along the ray of length r and Q_T^{ij} is the total quality factor measured along the ray-path. In the present formulation we assume that the high frequency amplitude spectrum at the source can be described by a function $S_i^A = const_i \cdot f^{-\gamma}$, γ being a constant for the whole set of data utilized. Taking the natural logarithm and making the derivative of the eq. (5) respect to frequency, f, it can be written for each ray-path:

$$D_f(\ln A_{ij}^{HF}) = D_f(\ln S_i^A) - \pi \frac{t_{ij}(r)}{Q_T^{ij}(r)} \qquad (6)$$

where D_f is the symbol of derivative. In obtaining formula (6) we assumed the independence of frequency for the site and instrument transfer function. The independence of frequency for the site term has been confirmed by Galluzzo et al. (2005) who studied the site transfer function at Mt. Vesuvius. The transfer function of the instruments is flat with frequency in the whole frequency range investigated. Transforming the couple of indexes ij in a single integer k associated with the single ray, as in the previous section, we can write:

$$D_f(\ln A_k^{HF}) = D_f(\ln S_i^A) - \pi \frac{t_k(r)}{Q_T^k(r)} \qquad (7)$$

Averaging the left hand quantity of the above equation over the rays considered (k index) we obtain:

$$< D_f(\ln A_k^{HF}) >_k = D_f^0(\ln A^{HF}) =$$
$$< D_f(\ln S_i^A) - \pi \frac{t_k(r)}{Q_T^k(r)} >_k \quad = D_f^0(\ln S^A) - \pi < \frac{t(r)}{Q_T(r)} >_k \quad (8)$$

$D_f^0(\ln S^A)$ results to be the same of $D_f(\ln S_i^A)$ (the average of the source spectral derivative equals the spectral derivative for the single event), so that we can write:

$$D_f(\ln A_k^{HF}) - D_f^0(\ln A^{HF}) \tilde{=} \pi (< \frac{t(r)}{Q_T(r)} >_k - \frac{t_k(r)}{Q_T^k(r)}) \qquad (9)$$

Indicating with d^D the quantity:

$$d_k^D = \frac{1}{\pi} \left[D_f(\ln A_k^{HF}) - D_f^0(\ln A^{HF}) \right] \qquad (10)$$

<mark>and expressing the right hand side of eq. (9) as already done in eq. (1) we obtain:</mark> <mark>Rev 2 Point 11</mark>

$$d_k^D = < \frac{t(r)}{Q_T(r)} >_k - \sum_{b=1}^{N\_cells} l_{kb} s_b Q_b^{-1} \qquad (11)$$

where the index k is referred to the k-th ray.

8

Making the same assumption that leads to formula (3), we can finally write:

$$\widetilde{d}_k^D = \sum_{b=1}^{N\_cells} l_{kb}s_b\delta Q_b^{-1} \tag{12}$$

where:

$$\widetilde{d}_k^D = < \frac{t_k}{Q_k} > -d_k^D - Q_T^{-1}\sum_{b=1}^{N\_cells} l_{kb}s_b \tag{13}$$

The inversion schemes (3) and (12) are formally identical, apart the constant values.

4.5   The estimate of the observables with the SD method.

Direct S spectral amplitudes were obtained in the <mark>frequency band centered at $f_c = 18\ Hz$, with the same bandwidth used for the CN method (Table II).</mark> The use of only this central frequency value is justified by the spectral features of the seismicity at Vesuvius like broadly discussed in Del Pezzo et al. (2006 b). We applied a DFT to windowed signals of length 2.5 seconds starting from the direct S travel time for both W-E and S-N components of the ground motion; then we log-averaged the spectra over the components.

We applied the SD method both to direct S waves and to direct P waves. Spectral amplitude for P waves was calculated in a time window starting from the P-wave onset and ending at 0.1 s before the S-wave picking, tapering each spectrum with a 10% cosine taper function.

The derivative was carried out for both S and P log-spectra in the frequency band starting from corner frequency (around 10 Hz for the whole set of data) and ending at 23 Hz (before the cut-off frequency of the anti-alias filter that was set up at 25 Hz). The derivative was computed using MATLAB "diffnew" routine.

5   Multi-resolution inversion.

The resolution of the methods depends both on the wavelength (which has to be smaller than the cell size) and on the number of rays crossing the single cell. <mark>A frequency $fc = 12$ Hz corresponds to a wavelength of about $200\ m$ for S waves. For P waves (examined at 18 Hz only) the corresponding wavelength is of the order of 150 m.</mark> Taking a cell size of 300 m we observe that the blocks bordering the volume of investigation are crossed by a number of rays

9

insufficient to ensure stability in the final solution, due to the distribution of the sources, concentrated along the crater axis and not uniformly distributed in space and depth inside the volume under investigation. This is the reason why we cannot invert the whole data set using a uniform resolution of 300 m. Consequently, we seek for solutions that can represent images in cells with a non-uniform size, as other researchers do in velocity tomography[Thurber (1987), Sambridge et al. (1998)]. In this approach, a relatively high-resolution can be obtained in a target area with a good ray coverage (this avoids linear dependence among the system equations). To perform this task we use an iterative inversion scheme [Thurber (1987), Eberhart-Phillips (1990)], in which we employ the results obtained in a lower resolution (LRR) as input for highest resolution (HRR). Bai and Greenhalgh (2005) describe an inversion scheme `Rev 3 minor` of this kind, applied to velocity tomography. Our inversion scheme is different from those above cited and will be described in the following points.

(1) The observables are calculated (both for the CN method and the SD method we apply the same inversion procedure) as above described.
(2) The attenuation factor averaged over the whole volume under study, Q_T^{-1}, is estimated with the CN method. It results in a really good agreement with that estimated by the previous works in the same area [Bianco et al. (1999), Del Pezzo et al. (2006 a)].
(3) The problem of eq. (3) and (12) is solved for a volume divided in cubic blocks of 1800 m side, using a positivity constraint. Then, each 1800 m side block is divided in 8 blocks of 900 m side, and the inverse quality factors thus calculated, $(Q_b^{-1})^{1800}$, are assigned to each of this cubes.
(4) The problem is solved for the 900 m cell size resolution, taking into consideration that each ray is characterized by the attenuation factor, which has been obtained by the solution of the previous step. In this way we obtain the new quantity $(\delta Q_b^{-1})^{900}$, which represents the variation from the inverse quality factor $(Q^{-1})^{1800}$ assigned to the 900 meters block in the previous step. We divide as before each 900 meters block in 27 blocks of `Rev 3 minor` 300 m side, assigning to each of them the inverse quality factor $(Q_b^{-1})^{900}$. Also for this step we use a positivity constraint on the $(Q_b^{-1})^{900}$.
(5) Finally we solve the problem for a 300 m side cell resolution, obtaining $(\delta Q_b^{-1})^{300}$.

It is noteworthy that, whereas the data vectors and the coefficient matrices need to be recalculated at each scale, the inversion problem is always formally the same and is given by equations (3) and (12). The details regarding how the data vectors and coefficient matrices are upgraded at each scale are reported in Appendix 3. It is also important to note that, at each step, we accept the solutions for the blocks in which the number of ray-segments , n_R, is given by:

$$n_R \geq \frac{2 Block\_side}{\lambda} \qquad (14)$$

This empirically determined threshold would ensure, in the assumption that the directions of ray-segments are randomly distributed in each block, that each block is homogeneously sampled.

6 Robustness, stability, checkerboard and synthetic anomaly tests.

6.1 a) Robustness

The robustness of the method is tested using a bootstrap approach, reducing randomly the number of available equations (rays). We applied this test to all the blocks at each cell size. The solutions for blocks of 1800 meters side were obtained for progressive reductions of the equations used to solve the inverse problem (see Appendix 3 , formula (21)); at each step we measured the quantity:

$$P = \frac{Q_b(0) - Q_b(\%)}{Q_b(0)} \times 100 \qquad (15)$$

where $Q_b(\%)$ is the quality factor of the block b obtained for the reduced data set, whereas $Q_b(0)$ is the solution obtained using the whole database. We repeated the inversion 100 times for each data reduction, measuring then the average percentage . We observed in most of the cases a significant increase of the percentage for a reduction of more then 40% of the data-set . The results for all the blocks of 1800 meters side solved are reported in Table III.

We repeated the same procedure for each scale, i.e. we measured the quantity P of formula (15) for all the 900 meters side blocks. We obtain a significant change in the value of P and a significant reduction of the average blocks resolved, for a random extraction of more than 40% of data. For sake of synthesis we report in Table IV the results obtained for 8 blocks contained in a single 1800-side block which resulted to be characterized by $(Q_b^{1800})^{-1} = 0.0128$; its position is shown in the upper panels of Figure 1 using the light grey square evidenced by number **1**. The results for the other 900 m side blocks solved by the inversion are similar.

Finally, we compared the variations of P calculated with eq. (15) for all the 300 meters side blocks, observing both a significant change in the value of the parameter models and a significant reduction in the average number of blocks resolved, for the random extraction of more than 20% of data. We report in Table V a selection of 8 blocks of 300 meters contained in the singular block of 900 meters side having $(Q_b^{900})^{-1} = 0.011$ (the position of the 900 meters block is shown in the upper panels of Figure 1 using the dark grey square evidenced

Rev 3 Point 3

by number **2**).

6.2 b) Stability.

The stability of the method is checked by changing the value of the constants in formulas (4) and (13). In formula (4) we let g_0 to vary between the values of $g_{\min} = 1$ and $g_{\max} = 2.5$ that represent the error limits of the average g as reported in Del Pezzo et al. (2006 a). In formula (13) we let $< \frac{t_k}{Q_k} >$ to vary in the interval $[-3\sigma+ < \frac{t_k}{Q_k} > , +3\sigma+ < \frac{t_k}{Q_k} >]$. The results do not change significantly. In both (4) and (13) we let Q_T^{-1} to vary in the interval $[-3\sigma+Q_T^{-1} , +3\sigma + Q_T^{-1}]$

For the resolution of $1800m$ the variations of each parameter model obtained for the extreme values are reported in Table VI.

For the intermediate resolution (900 meters) we repeat the same procedure setting maximum and minimum values of $(Q^{1800})^{-1}$ and Q_T^{-1} sampled in their confidence interval (3σ). The 8 blocks considered in Table VII are the same of Table IV.

For the maximum available resolution (300 meters), using the results obtained changing the values of Q_T^{-1}, $(Q_b^{1800})^{-1}$ and $(Q_b^{900})^{-1}$ in their confidence interval, we obtain the results shown in Table VIII for the 8 blocks considered in Table V.

6.3 c) Checkerboard inside the HRR.

Our results have been tested imposing an a priori attenuation structure to the area: we assumed an homogeneous medium in the LRR and a checkerboard distribution of the quality factors in the volume where the HRR is located, resolving only the blocks crossed by at least 5 rays per block, following eq. (14). Using the CN method we calculated the true spectral ratios and added to these values a Gaussian random error calculated with a random number generator with zero mean and standard deviation equal to 10% of the spectral ratio.

Rev 2 point 2 and 4
Rev 3 point 10

The synthetic structure results to be extremely well resolved in the central part, whereas the quality of the reproduction of the input values decreases toward the borders of the volume under investigation. The checkerboard test results (Figures 2 and 3) are shown both for the W-E and S-N sections already shown in Figure 1, and for five horizontal slices in the depth range between -500 to $-3500m$.

Both in Figure 2 and Figure 3 we marked with a white broken line the zone where the checkerboard structure is effectively reproduced, as described in the following. In Figure 2 it can be noticed that the input checkerboard structure (W-E and S-N sections in panel a) is well reproduced everywhere except in a small area toward North and toward East, corresponding to the geological structure of Mt. Somma (the same sections in panel b); this is due to the lack of seismic sensors in this area. The negative variations in the inverse quality factors under -3000 meters always well reconstruct the zones with low Q_S^{-1}. In Figure 3 the five panels on the left present five horizontal sections of the volume containing the input checkerboard structure, imaging the HRR (see also Figure 1, downward left panel); the good resolution achievable by the method used is evident in the volume constrained between 0 and -2700 m (right panels of the same figure). At $Z = -3500$ m, the method resolves at the maximum resolution only a subset of the input volume.

6.4   d) Synthetic anomaly

We performed a second test adopting the procedure described in Schurr et al.   Rev 3 point 4 and 5
(2003), using synthetic data by tracing rays through the real 3-D V_S model, in order to check the effective availability of the results which will be discussed in the following chapter. This test uses as input a Q_S^{-1} model created using anomalies comparable in size to those observed using the real data-set (W-E and S-N sections in Figure 4, panel a) but with slightly different geometries. A 10% normally distributed error was applied to the spectral ratios. The test shows that at maximum resolution the anomalies are generally well recovered between the surface and -3000 m (W-E and S-N sections in Figure 4, panel b). In the depth range between -3000 m and -4500 m the test shows that the resolution decreases. The test is consistent with the checkerboard test (Figure 3, $Z = -3500$ m) and shows that the maximum resolution achievable in this depth range is 900 m.

7   Results.   Rev 2 point 5,point 6, point 7   Rev 3 point 7,point 8, point 9, point 10

Using the present multi-resolution method, we obtained the attenuation structure under Mt. Vesuvius in two frequency bands (Table II), centered at 12 and 18 Hz. The images have a resolution of 300 meters in the sub-volumes with high ray coverage marked in Figures 2 and 3 with a white broken line. All the results obtained are shown in Figures 5, 6 and 7, where the depths (negative downward), are calculated respect to the sea level. In Figures 6 and 7 the images relative to the velocity tomography (SCA02) are also shown. The present database is a subset of the database used in the velocity tomography.

In Figure 5 the results of S-wave attenuation imaging obtained with both CN and SD are reported for sake of comparison.

Using CN technique, an estimate of the variation of Q_S^{-1} respect to the mean was obtained for the two frequency bands (12 and 18 Hz), where the signal to noise ratio value resulted sufficiently high for this analysis [see Del Pezzo et al. (2006 b)]. These images are reproduced in panels a and b of Figure 5. Using SD technique a unique image at 18 Hz was obtained (panel c).

Images shown in panel a and b of Figure 5 are very similar except for an higher attenuation zone (turquoise) located in a depth range between -2500 and -3500 m centered at 452000 onto the W-E section, visible in panel b.

Comparing panel b and panel c of Figure 5, we notice that in the HRR the images are similar. Outside the HRR slight differences between the two images appear in the W-E section, at a depth of approximately -1000 m, between coordinates 453000 and 454000. In this region CN method (panel b) gives a high attenuation contrast zone whereas the contrary occurs for SD method (panel c). We observed that the SD method produces in general images that are less variable in space respect to those from the CN method.

Figure 6, panel a, reports the W-E and S-N sections of the S- wave attenuation images at 18 Hz; in the same figure the S-wave velocity (panel b), P-wave attenuation (panel c) and P-wave velocity (panel d) for the W-E and S-N sections are also represented. V_P/V_S ratio as a function of depth (calculated as an average over the slices at different depth) is superimposed to all the figures. The color scale in panels a and c represents the variation of the inverse quality factor respect to the mean S- or P-wave attenuation; the color scales of panels b and d represent the absolute S- and P-wave velocity.

Figure 7 represents twenty horizontal slices at the depths $-500, -1000, -2000,$ -2700 and -3500 meters. Color scales represent the differences respect to the average S-wave velocity (first column), S-wave attenuation (second column), P-wave velocity (third column) and P-wave attenuation (fourth column) calculated for each slice. The differences respect to the average show the same pattern of the absolute P- and S- waves velocities and attenuation (in the discussion we will not make any difference between the absolute quantity and the variation respect to the mean), and better enlighten the lateral variations.

8 Discussion

The HRR is localized essentially under the central part of the cone spanning a depth range between +250 and -3500 m (see Figures 2 and 3). In this zone

14

we have thus an S-wave attenuation image with a resolution improved respect to that obtained by Del Pezzo et al. (2006 b) using a single scale approach. Laterally, the resolution becomes lower due to the station density, which is not comparable with the cell dimension [for a wider discussion on station density and resolution see Bai and Greenhalgh (2005)]. In general, the 3-D attenuation pattern shows a Q^{-1} which clearly decreases with depth in the 12 and 18 Hz frequency bands (Figure 5, panels a and b) , showing clearly visible attenuation contrasts localized along the borders of the already known structures (see e.g. SCA02), like the carbonate basement, well visible at the maximum resolution in the Q_S^{-1}, Q_P^{-1}, V_S and V_p images at -1500 meters (see Figures 6, all panels).

8.1 *Frequency dependence of the S-wave attenuation*

In the HRR the independence of attenuation from frequency is confirmed in the frequency range between 12 and 18 Hz. The panel b of Figure 5 shows an attenuation contrast localized between 452000 and 453000, in the depth range between -2500 and -3500 meters, with a size larger than the minimum resolution. This contrast is not evident in panel a of the same Figure, for the image obtained at 12 Hz, possibly due to the different linear dimensions of the anomalous region sampled by the different wavelength.

8.2 *Comparison between CN and SD images*

The S-wave images obtained under the cone at 18 Hz with CN and SD methods are quite enough similar, showing on average the same dependency of Q_S^{-1} with depth (Figure 5, panel b and c). In general the images obtained with CN appear much more smoothed than those obtained with SD. In the HRR most of the attenuation contrasts follow the same pattern, being sometimes different in value.

The sole significant differences between CN and SD images can be observed between -1000 m and -2000 m toward North and toward East (corresponding at surface with the geological structure of Mt. Somma). In this volume (Figure 5 panels b and c) the interface between carbonate basement and the overlying volcano materials, is not clearly defined in the SD image. On the other hand, this interface is clearly evidenced by SD method applied to P-waves, and very well defined by the velocity tomography (see also SCA02 and Zollo et al. (2002)).

The discrepancy above discussed may be due to the assumptions that are at the base of CN. In this method S-spectra are normalized by coda spectra, in order

to cancel out the site term. This procedure is based on the experimental result that the coda radiation is uniform for all the source station pairs after a lapse time greater than twice the S-wave travel time. This experimental property of coda waves may be not strictly verified in presence of a non-uniform scattering wave field (Wegler, 2003) that may produce for few waveforms a bias in the normalization of S-spectrum with coda spectrum. Despite this problem, the independence of CN of site transfer function makes CN approach particularly suitable for the application to volcanic areas, where site effects may severely affect the spectrum of S-radiation emitted by the VT earthquakes.

8.3   *Joint interpretation of velocity and attenuation images*

8.3.1   *General pattern*

We first analysed the velocity images, isolating the volumes characterized by strong laterally and/or in depth contrasts, velocity inversions, variations from the average V_P/V_S. Then, we associated them with the corresponding volumes in all the other available images. Comparing V_P with Q_P^{-1} and V_S with Q_S^{-1} images (Figures 6, all panels) we observe that high V_P zones correspond roughly to low Q_P^{-1} volumes and that high V_S zones correspond to low Q_S^{-1} volumes; the unique evident exception is the volume located under the central cone, confined in the depth range between -1000 m and -2000 m, where the pattern is characterized by a low V_S and V_P corresponding to high variations in attenuation (Q_S^{-1} and Q_P^{-1} strongly increase with depth).

8.3.2   *The shallower structures*

In average, the attenuation of the S- and P-waves increases toward North and East in all the images for the volumes above the sea level (Figure 6, panels a and c); interestingly, the S-N section of the Q_S^{-1} image (panel a) shows a low attenuation inclusion (green surrounded by orange, not included in the HRR) with dimension of the order of a 900 meters , corresponding to the structure of Mt. Somma, the ancient caldera border. This structure surrounds the central cone in the North and East quadrants (Figure 1, down left) and is characterized by higher rigidity older age lavas.

 In the HRR (marked with a broken white line in Figure 2, panel b), velocity and attenuation images clearly evidence the presence of a contrast between the structure above and the volume underneath the depth of 0 meters; this contrast marks the first interaction between the recent products of the volcano activity and the older higher rigidity materials.

A low attenuation zone [roughly surrounded by the rectangle **1**] is strongly

correlated with an high V_S and V_p zone in the same position, as shown in Figure 7 ($Z = -500$ meters). This zone is located inside the HRR (see Figure 3, panel a) and may represent the residual lava emitted during the last eruptions, completely solidified in the present time.

In the same slice (Figure 7 , $Z = -500$) we observe that the western part is characterized by low Q_S^{-1}, high Q_P^{-1} and low V_P/V_S . This features, in particular the opposite pattern of Q_S^{-1} and Q_P^{-1} , may be compatible with the presence of a CO_2 reservoir (Hansen et al., 2004). This interpretation is corroborated by the presence of the above discussed low attenuating body in the central part of the Figure. As reported by Hansen et al. (2004), when the magma rises, the decrease in confining pressure causes the magma to decompress and the biggest part of CO_2 exsolves; however, when the magma cools, a modest amount of CO_2 can be definitely trapped in the rock matrix, and could explain the observed low V_P and low V_P/V_S anomalies (Gerlach and Taylor, 1990). This interpretation is confirmed by the laboratory experiments of (Ito et al. (1979), Spencer (1979), Sengupta and Rendleman (1989)). Summarizing the results from these papers, at pressure below the saturation pressure (as should be at a depth of -500 meters), the presence of gas can lead to a decrease in V_S and V_P, an increase of Q_S^{-1}, and an anomalous decrease of Q_P^{-1}, that is the same pattern observed for Mt. Vesuvius.

The presence of melt or partially melt rocks would lead to a low V_P, a low V_S, high V_P/V_S ratio, high Q_P^{-1} and high Q_S^{-1}. In the depth range around -500 m there is consequently no evidence supporting the presence of patches of magma with dimensions larger than cell size.

8.3.3 The intermediate structure

A zone of strong lateral contrast is evident in both the V_P and V_S images [the zone surrounded by the rectangle marked by number **2** in the slices of Figure 7 ($Z = -1000$)] . In this zone there is no correspondence of the increasing velocity with decreasing attenuation, as already discussed in the "General pattern" section. The low attenuation area marked by the white rectangle **1** in Figure 7 ($Z = -1000$m) corresponds instead to an high velocity area. This area is a section of the anomalously high-velocity volume (figure 6, panels b and d) which seems to intrude from depth, in agreement with the interpretation reported in several velocity tomography studies [Zollo et al. (2002), Tondi and De Franco (2003), De Natale et al. (2005), SCA02], and interpreted as related to the residual part of solidified lava from the last eruption. This high attenuation and velocity zone is connected with the area marked by line **1** in Figure 7, $Z = -500$ m.

To refine the interpretation in the depth range around -1000 m, especially

for the area marked by rectangle **2** in Figure 7, we focus the attention on the W-E and S-N sections in Figures 6 [all panels]. The zone corresponding in depth with the maximum value of the V_P/V_S ratio roughly corresponds to the interface between high attenuation and low attenuation. This interface is also characterized by low V_P and low V_S. All these observations may be interpreted as due to the presence of a fractured medium permeated by fluids, as discussed in Hansen et al. (2004) and Eberhart-Phillips et al. (2004). In this interpretation the presence of a shallow patch of magma in the same depth range should be excluded, in the limit of the spatial resolution: in fact, the attenuation images do not show any particular evidence of melt, that, if present, should have produced both high Q_P^{-1} and high Q_S^{-1}. These results are in agreement with the previous interpretation done by SCA02 on the base of the ole velocity tomography, and are also corroborated by geochemical studies, that locate an hot aquifer under the cone just in the same position (Marianelli et al. (1999), Chiodini et al. (2001)). The properties observed at $Z = -1000$ m can be observed also at $Z = -2000$ m (see Figure 7). In particular a secondary maximum in the V_P/V_S ratio can be observed at -2000 m. The vertical sections of Q_P^{-1} and Q_S^{-1} (Figure 6 panels a and c) indicate the presence of a high attenuation zone, around -2000 m, included in a low attenuation body. This pattern can be interpreted as an highly cracked medium filled by fluids, in agreement with geochemical studies (Chiodini et al., 2001).

8.3.4 The deepest structure

The V_P ,V_S and V_P/V_S patterns between -2500 m and -4000 m (Figures 6, panels b and d) are more regular. The $Z = -2700$ and $Z = -3500$ slices of Figure 7 help in better understanding the velocity and attenuation features. The pattern of Q_P^{-1} and Q_S^{-1} are similar at $Z = -2700$ (Figure 7 and Figure 3), both in the HRR and in the LRR. Focusing the attention on the central part of the attenuation images (rectangle **3**), a high contrast in both Q_S^{-1} and Q_P^{-1}, not perfectly matching the contrast in both V_P and V_S can be observed. The imperfet match may be due to a lack of resolution of attenuation imaging in this depth range.

At $Z = -3500$ m, the decreasing attenuation corresponds to the increasing velocity outside rectangle 4, for both P and S waves. A low velocity and attenuation zone corresponding to the South-East sector of Figure 7 at $Z = -3500$ m is clearly visible, and marked with the rectangle **4**. In this region the low V_P/V_S ratio excludes the presence of partially melt rocks or fluid inclusions, suggesting on the contrary the presence of a cracked volume. This zone is spatially coincident with the zone of maximum seismic energy release, as shown in Figure 1 (upper-left and upper-right panels, the grey ellipsoidal line marked by number **3**).

9 Conclusions.

The present paper complements a previous preliminary study of the same area, which was carried out in a smaller volume respect to that used in the present study. The present paper uses a multi-resolution approach, which solves a 300 m cell size in the volume beneath the central crater located in the depth range between approximately 0 (the sea level) and -3500 m. The new study is based a data set improved respect to the first one (the number of waveforms in the present study is more than doubled respect to the previous), improving both stability and robustness. The improved resolution allowed a better definition of the 3-D pattern for both Q_P^{-1} and Q_S^{-1}, thus improving the joint interpretation of previous velocity images with the present attenuation structure. The essential results show that no magma patches with dimensions larger than the cell size are visible in the images and confirm the presence of shallow hydrothermal reservoirs (between -700 and -2300 m) evidenced by geochemical studies. The high resolution achievable between 0 and -1500 m allowed a small scale imaging of the residual solidified lava emitted during the last eruptions, leading to the interpretation in terms of large patches of gas located in the first kilometer below sea level. Interestingly, the zone of maximum seismic energy release, imaged for the first time at a resolution of 900 meters, coincides with a high attenuation and low velocity anomaly, easily interpretable as due to the presence of a cracked zone inside the limestone layer. These results are expected to add important constraints for the numerical models that will be adopted to simulate the next eruption, and consequently to be used for Civil Defense purposes.

10 Appendix 1

10.1 Coda Normalization Method.

As well known, the S-wave seismic energy density spectrum decays as a function of lapse-time as:

$$E_{ij}(f,r) = S_i(f)\theta_{ij}(\vartheta,\phi)I_j(f)T_j(f)\frac{1}{r_{ij}^2}\exp(-2\pi f\frac{t_{ij}(r)}{Q_T^{ij}(r)}) \qquad (16)$$

Rev 3 minor

where $E(f,r)$ is the energy density spectrum of the S-wave radiation emitted by the source i at total distance r measured along the ray-path connecting source(i) and station (j) ; f is the frequency. $S_i(f)$ is the energy spectrum at source, modulated by the radiation pattern function $\theta(\vartheta,\phi)$. I_j is the instrument transfer function and T_j is the site transfer function. t_{ij} is the travel time

along the ray whose length is r_{ij} and Q_T^{ij} is the total quality factor measured along the ray-path.

The coda energy spectrum evaluated around a given lapse time, t_c, can be considered as a function of the "average" medium properties and expressed as in Sato and Fehler (1998):

$$E^C(f,t) = S_i(f)I_j(f)T_j(f)P(f,t_c) \qquad (17)$$

where $P(f,t_c)$, is independent on both source-receiver distance and directional azimuth and depends only by the earth medium. The radiation pattern term $\theta_{ij}(\vartheta, \phi)$ disappears due to the well known property of natural space averaging of coda waves (Aki, 1980). For sake of simplicity, we assume the validity of the single scattering model, but in principle equation (17) is independent of any scattering model. Dividing eq. (16) for eq. (17) for each source-station pair, at lapse time t_c, we obtain

$$\frac{E_{ij}(f,r)}{E^C(f,t)}r_{ij}^2 = \frac{\theta_{ij}(\vartheta,\phi)}{P(f,t_c)}\exp\left[-2\pi f \int_{rij}\frac{dl}{v(l)Q_T^{ij}(l)}\right] \qquad (18)$$

The spectral ratio at the left side of formula (18) is independent of energy level at source, site and instrument transfer function. In eq. (18) the attenuation operator has been substituted with the path integral along the seismic ray, where $v(l)$ is the velocity along the path l. $\theta_{ij}(\vartheta,\phi)$ in principle depends on source azimuth ϕ and incidence angle ϑ. For a complete review of the method see Del Pezzo et al. (2006 b). In Appendix 2 we test the independence of the spectral ratio of formula (18) of radiation pattern for ratios evaluated on signal time windows longer than 2.5 seconds. In this case $\theta_{ij}(\vartheta,\phi)$ can be set equal to unity.

11   Appendix 2

11.1   Test for the independence of radiation pattern.

Using the properties of the early-coda, Gusev and Abubakirov (1999) developed an empirical method to test the independence of S-wave spectra from radiation-pattern, when the spectrum is estimated in a time window of duration much greater than the source duration. We make a similar test for the spectral ratio between S and coda energy spectra calculated for the earthquakes of Mt. Vesuvius. We consider for each ray connecting the source to the receiver, the quantity:

$$A = \frac{LR}{M} \qquad (19)$$

where L is the ray length, R is the spectral ratio between energies of formula (18) and $M = \exp(-\pi f r / V Q_{mean})$, with V indicating the average S-wave velocity, is the average anelastic attenuation in the area. A is implicitly dependent only on the radiation pattern, R being independent of site and instrument effects. The percent standard deviation ($\sigma_A / < A >$) calculated averaging A over the stations for a single earthquake, is plotted for different time window durations in Figure A2.1; this quantity abruptly decreases with increasing duration of the time window, as expected. We applied a statistical test [the "change point" test of Mulargia and Tinti (1985)] to estimate the "change point" of the pattern of A respect to the duration of the time window in which is calculated. The pattern results to be steady after 2.5 seconds at 99% confidence. Consequently, the radiation-pattern effects become negligible for time windows with a duration greater than 2.5 s. We interpret this result as due to the natural processes of averaging the radiation pattern effects that takes place in a ray-tube centered along the ray-path. The forward scattered radiation that arrives at the receiver soon after the ballistic (direct) arrival is contained inside this ray-tube(Gusev and Abubakirov, 1999). For the above reasons we assume that $\theta_{ij}(\vartheta, \phi)$ of eq. 18 is identically equal to unity.

12   Appendix 3

In this Appendix we explain the details relative to the points listed between 2 and 5 in the section 5

Point 2: estimate of the Average inverse Quality Factor (AQF).

S-waves AQF is calculated using the coda normalization method applied to the whole data-set ; the eq. (2) becomes:

$$d_k^C = \frac{1}{2\pi f} \ln\left(\frac{1}{P(f, t_c)}\right) - \sum_{b=1}^{N\_cells} l_{kb} s_b \left[Q_T^{-1}\right]^C \tag{20}$$

where $<>$ indicates the average over We obtained the inverse AQF for S waves (Q_T^{-1}):

$$(Q_T^{-1})^{12} = 0.010 \pm 0.003$$

$$(Q_T^{-1})^{18} = 0.019 \pm 0.003$$

where the above index is referred to the center frequency.

Uncertainty is estimated assuming that each spectrum is affected by a 10% of error due to the noise. This result is in good agreement with previous Q-estimate for S waves in the area (Del Pezzo et al., 2006 a).

P-waves AQF has been already calculated by Bianco et al. (1999).

Point 3: cell dimension of 1800 m.

The inversion problem of eq. (3) and (12) is solved for a grid of 1800 meters step. We can rewrite the equation as:

$$\tilde{d}_k^{C,D} = \sum_{b=1}^{N\_cells\_1800} G_{kb}^{1800}[(\delta Q_b^{1800})^{-1}]^{C,D} \tag{21}$$

where the superscript 1800 stands for the step of the grid, while the superscript C, D takes into account the different methods used. The elements of the inversion matrix, G_{kb}^{1800}, are the length of the $k - th$ ray segment in the 1800-meter side $b - th$ block, l_{kb}^{1800} , multiplied for his slowness s_b^{1800}:

$$G_{kb}^{1800} = l_{kb}^{1800} s_b^{1800} \tag{22}$$

Applying eq. (14), we consider only blocks crossed by at least $n_R = 35$ rays. The problem is solved separately for each frequency band. We solve the problem using the least squares algorithm "lsqlin" deployed in MATLAB.

The percentage reduction of the residuals, computed using the formula in Gubbins (2004), results to be 65%. The inverse quality factor of each 1800 meters block b is given by:

$$(Q_b^{1800})^{-1} = Q_T^{-1} + (\delta Q_b^{1800})^{-1} \tag{23}$$

Point 4: cell dimension of 900 meters.

The data vector obtained solving the inversion schemes of eq. (4) and (13) can be updated with the solutions obtained in the previous steps. Each ray crosses a medium whose quality factor is no more Q_T, and is affected by the quality factors of the cube that it effectively crosses. The elements of the data vector must represent the effect of the attenuation structure obtained in the previous steps. They become respectively:

$$(\tilde{d}_k^C)^{1800} =< \frac{1}{2\pi f} \ln(\frac{1}{P(f,t_c)}) > -d_k^C - Q_T^{-1} \sum_{b=1}^{N\_cells\_900} l_{kb}^{900} s_b^{900}$$

$$- \sum_{b=1}^{N\_cells\_900} l_{kb}^{900} s_b^{900} (\delta Q_b^{-1})^{1800,C} \tag{24}$$

and

$$(\tilde{d}_k^D)^{1800} = < \frac{t_k}{Q_k} >^{1800} -d_k^D - Q_T^{-1} \sum_{b=1}^{N\_cells\_900} l_{kb}^{900} s_b^{900} -$$

$$\sum_{b=1}^{N\_cells\_900} l_{kb}^{900} s_b^{900} (\delta Q_b^{-1})^{1800,D} \quad (25)$$

where $(\delta Q_b^{-1})^{1800,C}$ and $(\delta Q_b^{-1})^{1800,D}$ are respectively the solutions obtained with the CN method and the SD method for 1800 meters side blocks and that where assigned to the N_cells_900 blocks of 900 meters side crossed by the $k-th$ ray. In the SD method the constant value $< \frac{t_k}{Q_k} >^{1800}$ has also been updated with the informations obtained in the previous step. The inversion problem becomes, for a resolution of 900 meters:

$$(\tilde{d}_k^{C,D})^{1800} = \sum_{b=1}^{N\_cells\_900} G_{kb}^{900} [(\delta Q_b^{900})^{-1}]^{C,D} \quad (26)$$

where the superscript 900 stands for the step of the grid and the $(\delta Q_b^{900})^{-1}$ are the inverse variations respect the inverse quality factor of the 1800 meters cube in which they are contained. The elements of the inversion matrix, G_{kb}^{900}, are the length of the $k-th$ ray segment in the 900-meters side $b-th$ block l_{kb}^{900} multiplied for his slowness s_b^{900}:

$$G_{kb}^{900} = l_{kb}^{900} s_b^{900} \quad (27)$$

where, we consider only blocks crossed by at least $n_R = 17$ rays see equation (14). The inversion is linear and we can constrain the average of the $(\delta Q_b^{900})^{-1}$ to be zero. The inverse quality factor of each 900 meters block b is given by:

$$(Q_b^{900})^{-1} = Q_T^{-1} + (\delta Q_b^{1800})^{-1} + (\delta Q_b^{900})^{-1} \quad (28)$$

while the percentage reduction is 70% in residual.

Point 5: cell dimension of 300 meters.

The last step is achieved upgrading the data vectors writing the following two formulas:

$$(\tilde{d}_k^C)^{900} = < \frac{1}{2\pi f} \ln(\frac{1}{P(f,t_c)}) > -d_k^C - Q_T^{-1} \sum_{b=1}^{N\_cells\_300} l_{kb} s_b -$$

$$\sum_{b=1}^{N\_cells\_300} l_{kb} s_b (\delta Q_b^{-1})^{1800,C} - \sum_{b=1}^{N\_cells\_300} l_{kb} s_b (\delta Q_b^{-1})^{900,C} \quad (29)$$

23

and

$$(\tilde{d}_k^D)^{900} = < \frac{t_k}{Q_k} >^{900} -d_k^D - Q_T^{-1} \sum_{b=1}^{N\_cells\_300} l_{kb}s_b -$$
$$\sum_{b=1}^{N\_cells\_300} l_{kb}s_b(\delta Q_b^{-1})^{1800,D} - \sum_{b=1}^{N\_cells\_300} l_{kb}s_b(\delta Q_b^{-1})^{900,D} \quad (30)$$

where $(\delta Q_b^{-1})^{900,C}$ and $(\delta Q_b^{-1})^{900,D}$ are the solutions obtained in the previous steps that were assigned to a number of N_cells_300 blocks of 300 meters side, crossed by the $k - th$ ray. As before, the constant value $< \frac{t_k}{Q_k} >^{900}$ has been updated with the informations obtained in the previous steps. The inversion problem becomes:

$$(\tilde{d}_k^{C,D})^{900} = \sum_{b=1}^{N\_cells\_300} G_{kb}^{300}[(\delta Q_b^{300})^{-1}]^{C,D} \quad (31)$$

where the superscript 300 stands for the grid step, and the elements of the inversion matrix, G_{kb}^{300}, are given by the length of the $k - th$ ray segment in the $b - th$ block, l_{kb}^{300} , multiplied for his slowness s_b^{300}:

$$G_{kb}^{300} = l_{kb}^{300} s_b^{300} \quad (32)$$

applying eq. (14), we consider only blocks crossed by at least $n_R = 5$ rays. The percentage reduction in residual is 94%. The inverse quality factor of each 300 meters block b is given by:

$$(Q_b^{300})^{-1} = Q_T^{-1} + (\delta Q_b^{1800})^{-1} + (\delta Q_b^{900})^{-1} + (\delta Q_b^{300})^{-1} \quad (33)$$

13   Acknowledgements.

References

Andronico, D., Calderoni, G., Cioni, R., Sbrana, A., Suplizio, R., and Santacroce, R., 1995. *Geological map of Somma-Vesuvius Volcano.* Per. Mineral., 64: 77-78.

Aki, K., 1980. *Attenuation of shear-waves in the lithosphere for frequencies from 0.05 to 25 Hz.* Phys. Earth Planet. Inter., 21: 50-60.

Auger, E., Gasparini, P., Virieux, J., and Zollo, A., 2001. *Seismic Evidence of an Extended Magmatic Sill Under Mt. Vesuvius.* Science, 294: 1510-1512.

Bai, C., and Greenhalgh, S., 2005. *3D multi-step travel time tomography: imaging the local, deep velocity structure of Rabaul volcano, Papua New Guinea.* Physics of the Earth and Pl. Int., 151: 259-275.

Berrino, G., Coppa, U., De Natale, G., and Pingue, F., 1993. *Recent geophysical investigation at Somma–Vesuvius volcanic complex.* J. Volcanol. Geotherm. Res., 58: 239-262.

Bianco, F., Castellano, M., Milano, G., Ventura, G., and Vilardo, G., 1997. *The Somma-Vesuvius stress field induced by regional tectonics: evidences from seismological and mesostructural data.* J. Volcanol. Geotherm. Res., 82: 199-218.

Bianco, F., Castellano, M., Del Pezzo, E., and Ibanez, J. M., 1999. *Attenuation of short period seismic waves at Mt. Vesuvius, Italy.* Geophys. J. Int., 138: 67-76.

Block, L.V., 1991. *Joint hypocenter-velocity inversion of local earthquakes arrival time data in two geothermal regions.* Ph.d. dissertation, M.I.T., Cambridge.

Capuano, P., Gasparini, P., Zollo, A., Virieux, J., Casale, R., and Yeroyanni, M., 2003. *The internal structure of Mt. Vesuvius. A seismic tomography investigation.* Liguori Editore, ISBN 88-207-3503-2.

Chiodini, G., Marini, L., and Russo, M., 2001. *Geochemical evidence for the existence of high-temperature hydrothermal brines at Vesuvio volcano, Italy.* Geoch. et Cosmoch. Acta, 65(13), 2129– 2147.

Chouet, B., 1996. *New methods and future trends in seismological volcano monitoring.* In: Scarpa, R., Tilling, R.I. (Eds.), *Monitoring and Mitigation of Volcano Hazards.* Springer, Berlin, pp. 23–97.

Chouet, B., 2003. *Volcano Seismology.* Pageoph, 160: 739-788.

Del Pezzo, E., Bianco, F., and Saccorotti, G., 2004. *Seismic source dynamics at Vesuvius volcano, Italy.* J. Volcanol. Geotherm. Res., 133: 23-39.

Del Pezzo, E., Bianco, F., and Zaccarelli, L., 2006. *Separation of Qi and Qs from passive data at Mt. Vesuvius: a reappraisal of seismic attenuation.* Physics of the Earth and Pl. Int., 159: 202–212.

Del Pezzo, E., Bianco, F., De Siena, L., and Zollo A., 2006. *Small scale shallow attenuation structure at Mt. Vesuvius, Italy.* Physics of the Earth and Pl. Int., 157: 257-268.

De Natale, G., Capuano, P., Troise, C., and Zollo, A., 1998. *Seismicity at Somma-Vesuvius and its implications for the 3D tomography of the volcano.*

J. Volcanol. Geotherm. Res., Special Issue Vesuvius. Spera F. J., De Vivo B., Ayuso R.A., Belkin H.E. (Eds), 82: 175-197.

De Natale, G., Troise, C., Pingue, F., Mastrolorenzo, G., and Pappalardo, L., 2005. *The Somma–Vesuvius volcano (Southern Italy): Structure, dynamics and hazard evaluation.* Earth-Science Rev., 74: 73-111.

Eberhart-Phillips, D., 1990. *Three-dimensional P and S velocity structure in the Coalinga region, California.* J. Geophys. Res. 95: 15343–15363.

Eberhart-Phillips, D., Reyners, M., Chadwick, M., Chiu, J. M., 2005. *Crustal heterogeneity and subduction processes: 3-D V_P, V_P/V_S and Q in the southern North Island, New Zealand.* Geophys. J. Int. 162: 270–288.

Galluzzo, D., Del Pezzo, E., Maresca, R., La Rocca, M., and Castellano, M., 2005. *Site effects estimation and source-scaling dynamics for local earthquakes at Mt. Vesuvius, Italy.* Congress acts, ESG2006, Grenoble. Paper num. 36.

Gerlach, T., and Taylor, B., 1990. *Carbon isotope constraints on degassing of carbon dioxide from Kilauea volcano.* Geochim. Cosmochim. Acta 54, 2051–2058.

Giampiccolo, E., Gresta, S. and Ganci, G., 2003. *Attenuation of body waves in Southeastern Sicily (Italy).* Physics of the Earth and Pl. Int., 135: 267–279.

Gubbins, D., 2004. *Time series analysis & inverse theory for geophysicists.* Cambridge University Press.

Gudmundsson Ó., Finlayson D. M., Itikarai I., Nishimura Y., and Johnson W. R., 2004. *Seismic attenuation at Rabaul volcano, Papua New Guinea.* J. of Volc. and Geoth. Re., 130: 77-92.

Gusev, A. A., and Abubakirov, I. R., 1999. *Vertical profile of effective turbidity reconstructed from broadening of incoherent body-wave pulses.* Geophys. J. Int., 136: 309-323.

Hansen, S., Thurber, C. H., Mandernach, M., Haslinger, F., and Doran, C., 2004. *Seismic Velocity and Attenuation Structure of the East Rift Zone and South Flank of Kilauea Volcano, Hawaii.* Bull. of the Seism. Soc. of Am., 94: 1430-1440.

Ito, H., DeVilbiss, J., and Nur, A., 1979. *Compressional and shear waves in saturated rock during water–steam transition.* J. Geophys. Res. 84, 4731–4735.

Lomax, A., Zollo, A., Capuano, P., and Virieux, J., 2001. *Precise absolute earthquake location under Somma-Vesuvius volcano using a new three-dimensional velocity model.* Geophys. J. Int., 146: 313-331.

Marianelli, P., M´etrich, N., and Sbrana, A., 1999. *Shallow and deep reservoirs involved in magma supply of the 1944 eruption of Vesuvius.* Bull. Volcanol., 61: 48-63.

Mulargia, F., and Tinti, S., 1985. *Seismic sample areas defined from incomplete catalogues; an application to the Italian territory.* Phis. Earth Plan. Int, 40: 273-300.

Alejandro Nava, F., Garcìa-Arthur, R., Castro, R. R., Suàrez, C., Màrquez, B., Nùñez-Cornù, F., Saavedra, G. and Toscano, R., 1999. *S wave attenuation*

in the coastal region of Jalisco–Colima, México. Phys. Earth Pl. Int., 115: 247–257.

Santacroce, R., 1987. *Somma-Vesuvius.* CNR, Quaderni di Ricerca Scientifica.

Sambridge, M.S., and Gudmundsson, O., 1998. *Tomographic systems of equation with irregular cells.* J. Geophys. Res., 103: 773–781.

Sato, H., and Fehler, M.C.,1998. *Seismic Wave Propagation and Scattering in the Heterogenous Earth.* Springer.

Sengupta, M. K., and Rendleman, C. A., 1989. *Case study: the importance of gas leakage in interpreting amplitude-versus-offset (AVO) analysis.* Soc. Explor. Geophys. Abstracts 59, 848–850.

Scarpa, R., Tronca, F., Bianco, F., and Del Pezzo, E., 2002. *High resolution velocity structure beneath Mount Vesuvius from seismic array.* Geophys. Res. Lett., 29 (21): 2040.

Schurr, B., Asch, G., Rietbrock, A., Trumbull, R., and Haberland, C., 2003. *Complex patterns of fluid and melt transport in the central Andean subduction zone revealed by attenuation tomography.* Earth. Pl. Scien. Lett., 215: 105-119.

Spencer, J., 1979. *Bulk and shear attenuation in Berea sandstone: the effects of pore fluids.* J. Geophys. Res. 84, 7521–7523.

Thurber, C.H., 1987. *Seismic structure and tectonics of Kilauea volcano Hawaii.* In: Decker, R.W., Wright, T.L., Stauffer, P.H. (Eds.), Volcanism in Hawaii. US Geological Survey, pp. 919–934.

Tondi, R., and De Franco, R., 2003. *Three-dimensional modeling of Mount Vesuvius with sequential integrated inversion.* J. Geophys. Res., 108: 2256.

Um, J., and Thurber, C.H., 1987. *A fast algorithm for two-point seismic ray tracing.* Bull. of the Seism. Soc. of Am. 77: 972-986.

Wegler, U., 2003. *Analysis of multiple scattering at Vesuvius volcano, Italy, using data of the Tomoves active seismic experiment.* J. Volcanol. Geotherm. Res., 128: 45–63.

Zollo, A., D'Auria, L., De Matteis, R., Herrero, A., Virieux, J., and Gasparini, P., 2002. *Bayesian Estimation of 2-D P-Velocity Models From Active Seismic Arrival Time Data: Imaging of the Shallow Structure of Mt.Vesuvius (Southern Italy).* Geophys. J. Int., 151: 566-582.

14   Captions.

- Figure 1:Lower-left panel: Map of Mt. Vesuvius with station positions (black squares) and hypocentral locations (white dots) of the seismic events used in the present work. Black broken line depicts the old caldera rim. Upper-left and upper-right panels represent respectively the W-E and S-N sections, also reported as "W-E plane" and "S-N plane" in the lower-right "wide angle" view. The High Resolution Region (HRR) is roughly depicted by the inner polyhedron in the wide angle view. The solid line rectangles in

the upper left, upper right and lower left panels represent the sections of the HRR. The zones marked with 1and 2 represent the zone in which the robusteness test results are reported respectively in Table IV and V. The ellipsoidal zone marked with 3 shows the area with the maximum seismic energy release.

- Figure 2: Checkerboard test in the HRR. a) Input. W-E and S-N sections (also marked in figure 1, lower right panel); the white lines include all the maximum resolution cells defined by formula (14). In this volume we assumed a checkerboard structure, with high Q-contrast among the blocks; a uniform attenuation medium is assumed outside HRR. b) Output. Test results for a 10% error on synthetic data. The zones marked by the white broken lines include the cells where the checkerboard structure is effectively reproduced. ΔQ_S^{-1} grey scales represent the variation from the average quality factor.

- Figure 3: Left hand panels. Five horizontal slices at different depths (Z value respect to the sea level) of the volume containing the HRR. The white lines include all the maximum resolution cells defined by formula (14). The sections represent the input checkerboard structure also described in Figure 3, with the same colorscale. Rigth hand panels. The figures represent the test output; the zones marked by the white broken lines include the cells where the checkerboard structure is effectively reproduced.

- Figure 4: Synthetic anomaly test. The input structures (panel a) are included in a volume characterized by uniform attenuation. The output (panel b) show the reconstruction of the anomalies. Black areas are not resolved in the inversion. Colorscales refer to the variations respect to the mean inverse quality factor. The zones marked by the white broken lines include the cells where the checkerboard structure is effectively reproduced.

- Figure 5: Results of the attenuation tomography inversion, in the frequency band centered at 12 Hz (panel a), and 18 Hz (panel b) for the CN method, compared with the results obtained at 18 Hz for the SD method (panel c). W-E and S-N sections are those marked in Figure 1 (down-rigth panel). Black areas are not resolved in the inversion.Colorscales refer to the variations respect to the mean inverse quality factor. The zones marked by the white broken lines include the cells where the checkerboard structure is effectively reproduced.

- Figure 6: The W-E and S-N sections represent the attenuation structure inferred for S-waves (CN method), in the frequency band centered at 18 Hz (panel a), and the S-velocity structures inferred by Scarpa et al. (2002) (panel b). The dashed line represents the V_P/V_S pattern with depth and is overimposed to all figures. The P-wave attenuation (SD method, 18 Hz) and velocity (inferred by Scarpa et al. (2002)) are also represented in panels c and d. The colorscales in panels a and c refer to the variations respect to the mean inverse quality factor obtained in the inversions for S- and P-waves. The colorscales in panels b and d represent the absolute S- and P-wave velocity. Black areas are not resolved in the inversion. The zones marked by

the white broken lines include the cells where the checkerboard structure is effectively reproduced.

- Figure 7: Five horizontal slices of the the volume containing HRR at different depths (Z). The colorscales for S- (first column) and P-wave (third column) attenuation images represent the variations from the mean inverse quality factor calculated on each horizontal slice at each depth. The colorscales represented in the second and fourth coloumns respectively represent the variations of S- and P-wave velocity from the average velocity calculated at each depth. On each image we marked with numbered black rectangles, the zones characterized by important properties, widely discussed in the text. The zones marked by the white broken lines include the cells where the checkerboard structure is effectively reproduced.

- Figure A2.1: The percent standard deviation, σ/μ, as a function of the window duration for an earthquake recorded at all the stations. σ/μ is obtained calculating the average, μ [over stations] , of the log of spectral ratio between direct S radiation and coda radiation, after correcting the amplitudes for geometrical spreading and for the average Q. Downward arrow indicates the change-point as discussed in the text.

Table I

Station	E-W (UTM)	N-S (UTM)	altitude (a.s.l.) (m)
BAFM	450372	4518076	594
BKEM	452677	4518762	850
BKNM	451875	4520020	865
FTCM	452692	4516337	350
OVO	449190	4519705	600
POLM	447910	4522499	181
SGVM	450568	4518706	734

Table II

$-\Delta f$	$f_c(Hz)$	$+\Delta f$
8.2	12	15.8
12.4	18	23.6

29

Table III

Robusteness Test - 1800 m

Block#	1	2	3	4	5	6	7	8	9	10	11	12
$P^{1800}, 10\%$	1%	0%	0%	13%	7%	4%	0%	$0,1\%$	0%	0%	0%	3%
$P^{1800}, 20\%$	1%	0%	2%	29%	9%	11%	17%	1%	0%	0%	0%	3%
$P^{1800}, 30\%$	2%	1%	3%	28%	9%	9%	50%	$0,3\%$	0%	0%	0%	2%
$P^{1800}, 40\%$	3%	3%	10%	29%	8%	16%	87%	2%	1%	0%	0%	8%
$P^{1800}, 50\%$	6%	2%	11%	62%	20%	25%	87%	3%	1%	0%	0%	9%

Robustness test at the lowest resolution; the average percentageof eq. (15) is represented for all the blocks resolved. The increasing percentage in the first column is the data reduction.

Table IV

Robusteness Test - 900 m

Block#	1	2	3	4	5	6	7	8
P^{900}, 10%	1%	15%	2%	1%	10%	1%	31%	1%
P^{900}, 20%	1%	13%	15%	1%	12%	8%	> 100%	1%
P^{900}, 30%	1%	21%	15%	1%	16%	9%	> 100%	1%
P^{900}, 40%	2%	53%	29%	2%	30%	7%	> 100%	2%
P^{900}, 50%	2%	58%	72%	2%	40%	11%	> 100%	2%

Robustness test at the intermediate resolution; the average percentage of eq. (15) is represented for the 8 blocks in which the single 1800 meters side block of $(Q_b^{1800})^{-1} = 0.0128$ wich includes the cone was divided. The increasing percentage in the first column is the data reduction.

Table V

Robusteness Test - 300 m

Block#	1	2	3	4	5	6	7	8
P^{300}, 10%	12%	16%	21%	59%	30%	5%	1%	14%
P^{300}, 20%	37%	90%	54%	99%	17%	48%	90%	70%
P^{300}, 30%	> 100%	> 100%	67%	> 100%	69%	> 100%	98%	> 100%

Robustness test at the highest resolution; the average percentage of eq. (15) is represented for 8 blocks contained in a single 900 meters side block of $(Q_b^{900})^{-1} = 0.0110$. The increasing percentage in the first column is the data reduction.

Table VI

Stability Test - 1800 m

Block#	1	2	3	4	5	6	7	8	9	12
$[(Q^{1800})^{-1}] \times 10^{-2}$	1,98	1,79	1,50	2,44	1,28	1,37	0,92	2,86	0,51	3,16
$[(Q^{1800})^{-1}] \times 10^{-2}, (Q_T^{\min})^{-1}$	1,83	1,67	1,72	1,84	1,28	1,43	1,15	2,72	0,49	3,21
$[(Q^{1800})^{-1}] \times 10^{-2}, (Q_T^{\max})^{-1}$	1,88	1.69	1,10	2,88	1,11	1,08	0,54	2,74	0,40	2,81

Stability test at the lowest resolution; the value of the inverse quality factor of each resolved block is dependent on the maximum $((Q_T^{\max})^{-1} = 0.026)$ and minimum $((Q_T^{\min})^{-1} = 0.008)$ average inverse quality factor allowed.

Table VII

Stability Test - 900 m

Block#	1	2	3	4	5	6	7	8
$[(Q^{900})^{-1}] \times 10^{-2}$	1,79	0,52	0,96	1,79	2,75	1,64	0	1,79
$[(Q^{900})^{-1}] \times 10^{-2}, (Q_T^{\min})^{-1}, (Q_{b\,\min}^{1800})^{-1}$	1,88	0,46	1,12	1,88	2,36	1,77	0	1,88
$[(Q^{900})^{-1}] \times 10^{-2}, (Q_T^{\max})^{-1}, (Q_{b\,\max}^{1800})^{-1}$	1.67	0,58	0,80	1,67	3,14	1,51	0	1,67

Stability test at the intermediate resolution; the value of each inverse quality factor is both dependent on the maximum $((Q_T^{\max})^{-1} = 0.026)$ and minimum $((Q_T^{\min})^{-1} = 0.008)$ average inverse quality factor and the maximum $((Q_{b\,\max}^{1800})^{-1} = 0.0188)$ and minimum $((Q_{b\,\min}^{1800})^{-1} = 0.0167)$ inverse quality factor of the block in which they are contained.

Table VIII

Stability Test - 300 m

Block#	1	2	3	4	5	6	7	8
$[(Q^{300})^{-1}] \times 10^{-2}$	$5,61$	$1,78$	$1,91$	$0,39$	$1,44$	0	$2,26$	0
$[(Q^{300})^{-1}] \times 10^{-2}, (Q_{T\min})^{-1}, (Q_{b\min}^{1800})^{-1}, (Q_{b\min}^{900})^{-1}$	$2,59$	$1,76$	$1,34$	$0,05$	$1,29$	0	$2,60$	0
$[(Q^{300})^{-1}] \times 10^{-2}, (Q_{T\max})^{-1}, (Q_{b\max}^{1800})^{-1}, (Q_{b\min}^{900})^{-1}$	$6,91$	$1,99$	$2,01$	$1,59$	$1,32$	0	$1,34$	0

Stability test at the highest resolution; the value of each inverse quality factor is both dependent on the maximum $((Q_T^{\max})^{-1} = 0.026)$ and minimum $((Q_T^{\min})^{-1} = 0.008)$ average inverse quality factor. It is also dependent on the maximum $((Q_{b\max}^{1800})^{-1} = 0.0188, (Q_{b\max}^{900})^{-1} = 0.0177)$ and minimum $((Q_{b\min}^{1800})^{-1} = 0.0167, (Q_{b\min}^{900})^{-1} = 0.0151)$ inverse quality factor of the blocks in which they are contained.